Inertial and Magnetic Sensing

of

Human Motion

Daniel Roetenberg

Samenstelling van de promotiecommissie:

Prof. dr. ir. P.H. Veltink (promotor)	Universiteit Twente
Prof. dr. ir. A.J. Mouthaan (voorzitter)	Universiteit Twente
Prof. dr. ir. C.H. Slump	Universiteit Twente
Prof. dr. ir. H.J. Hermens	Universiteit Twente
Prof. dr. F.C.T. van der Helm	Technische Universiteit Delft
Prof. dr. F. Gustafsson	Linköping University, Sweden
Dr. ir. J. Harlaar	VU Medisch Centrum
Dr. ir. H.J. Luinge	Xsens Technologies

INERTIAL AND MAGNETIC SENSING OF HUMAN MOTION

PROEFSCHRIFT

ter verkrijging van
de graad van doctor aan de Universiteit Twente,
op gezag van de rector magnificus,
prof. dr. W.H.M. Zijm,
volgens besluit van het College voor Promoties
in het openbaar te verdedigen
op woensdag 24 mei 2006 om 13.15 uur

door

Daniel Roetenberg
geboren op 30 april 1976
te Almelo

Dit proefschrift is goedgekeurd door de promotor:

prof. dr. ir. P.H. Veltink

Table of Contents

Chapter 1

Introduction

1.1   The fascination for motion

THE SCIENCE of human motion analysis is fascinating because of its highly interdisciplinary nature and wide range of applications. Histories of science usually begin with the ancient Greeks, who first left a record of human inquiry concerning the nature of the world in relationship to our powers of perception. Aristotle (384-322 B.C.) might be considered the first biomechanician. He wrote the book called 'De Motu Animalium' - On the Movement of Animals. He not only saw animals' bodies as mechanical systems, but pursued such questions as the physiological difference between imagining performing an action and actually doing it [69].

Figure 1.1 — 'De Motu Animalium', Borelli 1680.

Nearly two thousand years later, in his famous anatomic drawings, Leonardo da Vinci (1452-1519) sought to describe the mechanics of standing, walking up and down hill, rising from a sitting position, and jumping. Galileo Galilei (1564-1643) followed a hundred years later with some of the earliest attempts to mathematically analyze physiologic function. Building on the work of Galilei, Borelli (1608-1679) figured out the forces required for equilibrium in various joints of the human body well before Newton published the laws of motion (see Figure 1.1). He also determined the position of the human center of gravity, calculated and measured inspired and expired air volumes, and showed that inspiration is muscle-driven and expiration is due to tissue elasticity. The early work of these pioneers of biomechanics was followed up by Newton (1642-1727), Bernoulli (1700-1782), Euler (1707-1783), Poiseuille (1799-1869), Young (1773-1829), and others of equal fame [99]. Muybridge (1830-1904) was the first photographer to dissect human and animal motion (Figure 1.2). This technique was first used scientifically by Marey (1830-1904), who correlated ground reaction forces with movement and pioneered modern motion analysis. In the 20th century, many researchers and (biomedical) engineers contributed to an increasing knowledge of human kinematics and kinetics.

1.2   Human motion analysis

Many different disciplines use motion analysis systems to capture movement and posture of the human body. Basic scientists seek a better understanding of the mechanisms that are used to translate muscular contractions about articulating joints into functional accomplishment, e.g. walking [107]. Increasingly, researchers
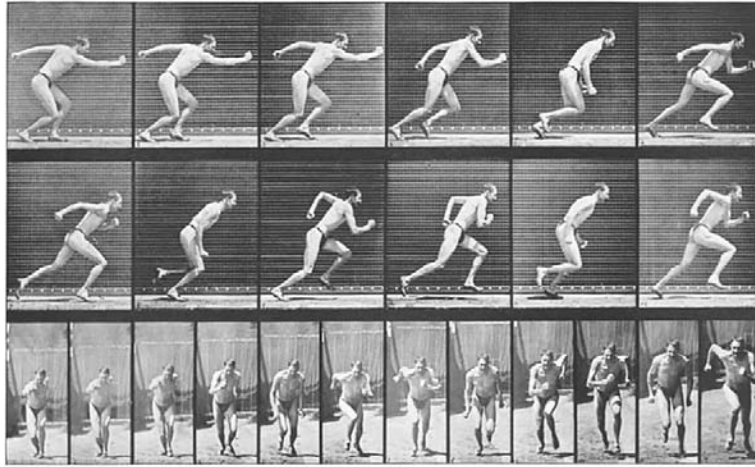
Figure 1.2 — 'The Human Figure in Motion', Muybridge 1878.

endeavor to better appreciate the relationship between the human motor control system and gait dynamics. In the realm of clinical gait analysis, medical professionals apply an evolving knowledge base in the interpretation of the walking patterns of impaired ambulators for the planning of treatment protocols, e.g. orthotic prescription and surgical intervention and allow the clinician to determine the extent to which an individual's gait pattern has been affected by an already diagnosed disorder [34]. With respect to sports, athletes and their coaches use motion analysis techniques in a ceaseless quest for improvements in performance while avoiding injury. The use of motion capture for computer character animation or virtual reality (VR) applications is relatively new. The information captured can be as general as the position of the body in space or as complex as the deformations of the face and muscle masses. The mapping can be direct, such as human arm motion controlling a character's arm motion, or indirect, such as human hand and finger patterns controlling a character's skin color or emotional state. The idea of copying human motion for animated characters is, of course, not new. To get convincing motion for the human characters in Snow White, Disney studios traced animation over film footage of live actors playing out the scenes. This method, called rotoscoping, has been successfully used for human characters ever since. In the late 1970's, when it began to be feasible to animate characters by computer, animators adapted traditional techniques, including rotoscoping.

Generally, motion analysis data collection protocols, measurement precision, and data reduction models have been developed to meet the requirements for their specific settings. For example, sport assessments generally require higher data acquisition rates because of increased velocities compared to normal walking. In VR applications, real-time tracking is essential for a realistic experience of the user,

so the time lag should be kept to a minimum. Years of technological development has resulted into many systems for measuring body segment positions and angles between segments. They can be categorized in mechanical, optical, magnetic, acoustic and inertial trackers. The human body is often considered as a system of rigid links connected by joints. Human body parts are not actually rigid structures, but they are customarily treated as such during studies of human motion [119].

Mechanical trackers utilize rigid or flexible goniometers which are worn by the user (Figure 1.3). Goniometers within the skeleton linkages have a general correspondence to the joints of the user. These angle measuring devices provide joint angle data to kinematic algorithms which are used to determine body posture. Attachment of the body-based linkages as well as the positioning of the goniometers present several problems. The soft tissue of the body allows the position of the linkages relative to the body to change as motion occurs. Even without these changes, alignment of the goniometer with body joints is difficult. This is specifically true for multiple degree of freedom (DOF) joints, like the shoulder. Due to variations in anthropometric measurements, body-based systems must be recalibrated for each user.
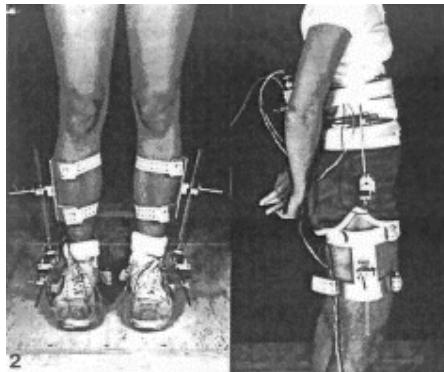
Figure 1.3 — Triaxial goniometer as applied to a subject for bilateral hip and ankle joint motion analysis, 1980.

Optical sensing encompasses a large and varying collection of technologies. Image-based systems determine position by using multiple cameras to track predetermined points (markers) on the subject's body segments, aligned with specific bony landmarks. (Figure 1.4). Position is estimated through the use of multiple 2D images of the working volume. Stereometric techniques correlate common tracking points on the tracked objects in each image and use this information along with knowledge concerning the relationship between each of the images and camera parameters to calculate position. The markers can either be passive (reflective) or active (light emitting). Reflective systems use infrared (IR) LED's mounted around the camera lens, along with IR pass filters placed over the cam-

Figure 1.4 — Modern motion capture system used in film and game industries. Actor Andy Serkis in full motion capture suit, and right the CG mask of Gollum (Lord of the Rings).

era lens and measure the light reflected from the markers. Optical systems based on pulsed-LED's measure the infrared light emitted by the LED's placed on the body segments. Also camera tracking of natural objects without the aid of markers is possible, but in general less accurate. It is largely based on computer vision techniques of pattern recognition and often requires high computational resources. Structured light systems use lasers or beamed light to create a plane of light that is swept across the image. They are more appropriate for mapping applications than dynamic tracking of human body motion. Optical systems suffer from occlusion (line of sight) problems whenever a required light path is blocked. Interference from other light sources or reflections may also be a problem which can result in so-called ghost markers.

Acoustic tracking systems use ultrasonic pulses and can determine position through either time-of-flight of the pulses and triangulation or phase-coherence. Both outside-in and inside-out implementations are possible, which means the transmitter can either be placed on a body segment or fixed in the measurement volume. The physics of sound limit the accuracy, update rate and range of acoustic tracking systems. A clear line of sight must be maintained and tracking can be disturbed by reflections of the sound.

Magnetic motion capture systems utilize sensors placed on the body to measure magnetic fields generated by a transmitter source. The transmitter source is constructed of three perpendicular coils that emit a magnetic field when a current is applied. The 3D sensors measure the strength of the field which is proportional to the distance of each coil from the field emitter assembly. The sensors and source are connected to a processor that calculates position and orientation of each sensor based on its measured field values. AC, or alternating current, trackers drive fields at one or more frequencies for their magnetic field sources [87]. If a single

frequency is used on all three (X,Y,Z) of its axes, only one at a time can be energized in order to know precisely where the field originates. This approach often is referred to as *time multiplexed* since the three windings are driven at different times. If three frequencies are used, then all three can be driven simultaneously. This has many advantages but also increases complexity and costs. This approach often is referred to as *frequency multiplexed*. Pulsed DC trackers activate their coils with short current pulses [5]. They are always time multiplexed since there is no way to distinguish one axis from another if more than one is energized simultaneously. A certain amount of 'off' time also is mandated because environmental DC signals such as the earth's field must be measured and subtracted from the sensor outputs. Magnetic systems do not suffer from line of sight problems because the human body is transparent for the used magnetic fields [33]. However, the shortcomings of magnetic tracking systems are directly related to the physical characteristics of magnetic fields. Magnetic fields decrease in power rapidly as the distance from the generating source increases and they can easily be disturbed by (ferro)magnetic materials within the measurement volume.

Inertial sensors use the property of bodies to maintain constant translational and rotational velocity, unless disturbed by forces or torques, respectively. The vestibular system, located in the inner ear, is a biological 3D inertial sensor. It can sense angular motion as well as linear acceleration of the head. The vestibular system is important for maintaining balance and stabilization of the eyes relative to the environment. Practical inertial tracking is made possible by advances in miniaturized and micromachined sensor technologies, particularly in silicon accelerometers and rate sensors. Miniature sensor units are placed on each body segments to be tracked. A rate gyroscope measures angular velocity, and if integrated over time provides the change in angle with respect to an initially known angle. An accelerometer measures accelerations, including gravitational acceleration $\mathbf{g}$. If the angle of the sensor with respect to the vertical is known, the gravity component can be removed and by numerical integration, velocity and position can be determined. Noise and bias errors associated with small and inexpensive sensors make it impractical to track orientation and position changes for long time periods if no compensation is applied [36].

1.3   Ambulatory tracking

Commercial optical systems such as Vicon (reflective markers) [113] or Optotrak (active markers) [84] are often considered as a 'golden standard' in human motion analysis. Although these systems provide accurate position information (errors $\approx$ 1mm), there are some important limitations. The most important factors are the high costs and limited measurement volume. The use of a specialized laboratory

with fixed equipment impedes many applications, like monitoring of daily life activities or assessment of workload in ergonomic studies. Recently, the health care system trend toward early discharge to monitor and train patients in their own environment. This has promoted a large development of non-invasive portable and wearable systems [13, 4]. Besides physiological parameters, such as heart rate and blood pressure, body posture and activity provide important information.

Inertial sensors have been successfully applied for measurements outside the lab [77]. The orientation obtained by present-day micromachined gyroscopes typically shows an increasing error of a few degrees per second. For accurate and drift free orientation estimation several methods have been reported combining the signals from 3D gyroscopes, accelerometers and magnetometers [30]. Accelerometers are used to determine the direction of the local vertical by sensing acceleration due to gravity. Magnetic sensors provide stability in the horizontal plane by sensing the direction of the earth magnetic field like a compass. Data from these complementary sensors can be used to eliminate drift by continuous correction of the orientation obtained by rate sensor data. This combination is also known as an attitude and heading reference system (AHRS).

Currently, relative distances on the body can only be estimated roughly by using anatomic knowledge of segment lengths and joint characteristics in combination with the inertial sensor based segment orientation estimates [76, 8, 120, 67]. This is not satisfactory in cases with complex joints and non-rigid body parts like the shoulder and back. Moreover, in this kinetic chain, model and orientation errors of joints and segments can accumulate in position errors in the connecting body parts. Absolute distances between body segments can principally not be assessed with inertial sensors solely. Only short-term estimates of position changes within seconds can be estimated accurately due to the unknown starting position and the inherent integration drift. Therefore, inertial position measurements need to be combined with a possibly slower, but regular and sufficiently accurate method.

This thesis deals with ambulatory orientation and position measurements of the human body. The required accuracy of such a system is in the order of millimeters for position and a few degrees for orientation measurements, with a minimum sample rate of 50 to 100 Hz. In the next sections, we will go more into detail on the background of the sensors and technology used in accomplishing this goal.

1.4 Inertial sensors

A single axis accelerometer consists of a mass, suspended by a spring in a housing (Figure: 1.5). Springs (within their linear region) are governed by a physical principle known as Hooke's law. Hooke's law states that a spring will exhibit a restoring force which is proportional to the amount it has been expanded or
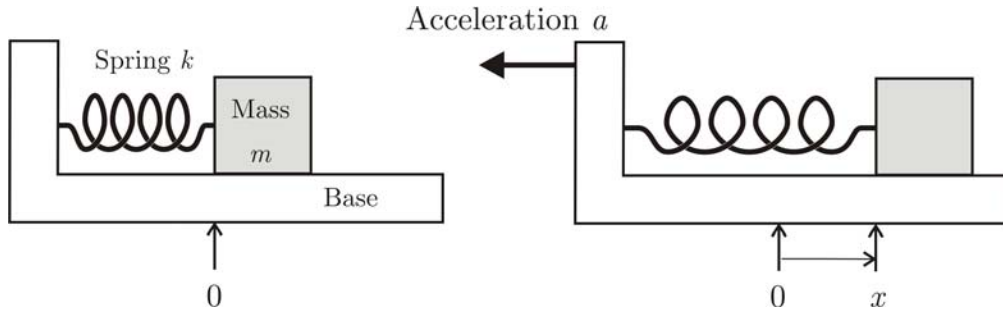
Figure 1.5 — A single axis accelerometer consisting of a mass suspended by a spring. Left: no acceleration. Right: acceleration of base to the left resulting in an expanded spring.

compressed. Specifically, $F = kx$, where k is the constant of proportionality between displacement x and force F. The other important physical principle is that of Newton's second law of motion which states that a force operating on a mass which is accelerated will exhibit a force with a magnitude $F = ma$. This force causes the mass to either compress or expand the spring under the constraint that $F = ma = kx$. Hence an acceleration a will cause the mass to be displaced by $x = \frac{ma}{k}$, or, if we observe a displacement of x, we know the mass has undergone an acceleration of $a = \frac{kx}{m}$. In this way, the problem of measuring acceleration has been turned into one of measuring the displacement of a mass connected to a spring. In order to measure multiple axes of acceleration, this system needs to be duplicated along each of the required axes.

Gyroscopes are instruments that are used to measure angular motion. There are two broad categories: (1) mechanical gyroscopes and (2) optical gyroscopes. Within both of these categories, there are many different types available. The first mechanical gyroscope was built by Foucault in 1852, as a gimbaled wheel that stayed fixed in space due to angular momentum while the platform rotated around it (Figure 1.6). Mechanical gyroscopes operate on the basis of conservation of angular momentum by sensing the change in direction of an angular momentum. According to Newton's second law, the angular momentum of a body will remain unchanged unless it is acted upon by a torque. The fundamental equation describing the behavior of the gyroscope is:

$$\boldsymbol{\tau} = \frac{d\mathbf{L}}{dt} = \frac{d\left(I\boldsymbol{\omega}\right)}{dt} = I\boldsymbol{\alpha} \tag{1.1}$$

where the vectors $\boldsymbol{\tau}$ and $\mathbf{L}$ are, respectively, the torque on the gyroscope and its angular momentum, the scalar I is its moment of inertia, the vector $\boldsymbol{\omega}$ is its angular velocity, and the vector $\boldsymbol{\alpha}$ is its angular acceleration.

Gimbaled and laser gyroscopes are not suitable for human motion analysis due to their large size and high costs. Over the last few years, micromachined inertial
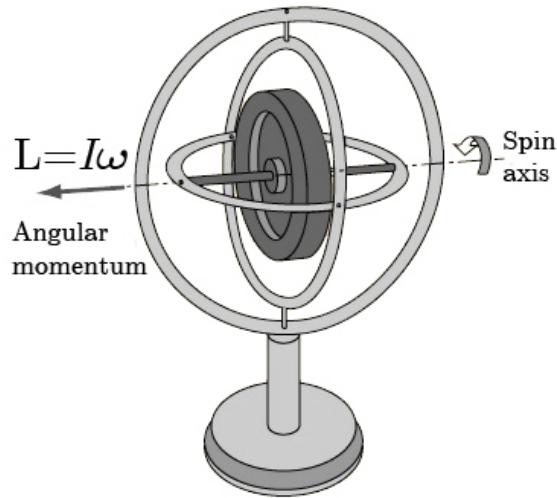
Figure 1.6 — A conventional spinning wheel gyroscope. The rapidly spinning inner wheel will maintain its direction in space if the outside framework changes.

sensors have become more available. Vibrating mass gyroscopes are small, inexpensive and have low power requirements, making them ideal for human movement analysis. A vibrating element (vibrating resonator), when rotated, is subjected to the Coriolis effect that causes secondary vibration orthogonal to the original vibrating direction. By sensing the secondary vibration, the rate of turn can be measured (see Figure 1.7). The Coriolis force is given by:

$$\mathbf{F}_C = -2m\left(\boldsymbol{\omega} \times \mathbf{v}\right) \tag{1.2}$$

where m is the mass, $\mathbf{v}$ the momentary speed of the mass relative to the moving object to which it is attached and $\boldsymbol{\omega}$ the angular velocity of that object. Various micro-electromechanical machined geometries are available, of which many use the piezo-electric effect for vibration exert and detection.
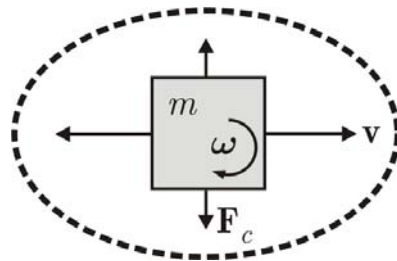

Figure 1.7 — A vibrating mass gyroscope consists of mass, which is brought into vibration $\mathbf{v}$. When the gyroscope is rotated, the mass will undergo a small additional displacement caused by the Coriolis force $\mathbf{F}_C$ in the direction perpendicular to the original displacement.

1.5 Sensor fusion

The traditional application area of inertial sensors is navigation as well as guidance and stabilization of military systems. Position, velocity and attitude are obtained using accurate, but large gyroscopes and accelerometers, in combination with other measurement devices such as GPS, radar or a baro altimeter. Generally, signals from these devices are fused using a Kalman filter to obtain quantities of interest. The Kalman filter [52] is useful for combining data from several different indirect and noisy measurements. It weights the sources of information appropriately with knowledge about the signal characteristics based on their models to make the best use of all the data from each of the sensors. There is no such thing as a perfect measurement device; each type of sensor has its strong and weak points. The idea behind sensor fusion is that characteristics of one type of sensor are used to overcome the limitations of another sensor. For example, magnetic sensors are used as a reference to prevent the gyroscope integration drift about the vertical axis in the orientation estimates of the AHRS. However, iron and other magnetic materials will disturb the local magnetic field and as a consequence, the orientation estimate. Errors related to magnetic disturbances will have different spatial and temporal properties than gyroscope drift errors. Using this *a priori* knowledge, the effects of drift and disturbances can both be minimized.

The inertial sensors of the inertial navigation system (INS) can be mounted on vehicles in such a way they stay leveled and pointed in a fixed direction. This system relies on a set of gimbals and sensors attached on three axes to monitor the angles at all times. Another type of INS is the strapdown system that eliminates the use of gimbals and which is suitable for human motion analysis. In this case, the gyros and accelerometers are mounted directly to the structure of the vehicle or strapped on the body segment. The measurements are made in reference to the local axes of roll, pitch, and heading (or yaw). The clinical reference system provides anatomically meaningful definitions of main segmental movements (e.g. flexion-extension, abduction-adduction or supination-pronation) (see Figure 1.8). In this thesis, rotation matrices are used to describe 3D orientations.

1.6 Outline of the thesis

In **Chapter 2**, a method is introduced for estimating body segment orientation combing the sensor signals of miniature 3D gyroscopes, accelerometers and magnetometers in a complementary Kalman filter. Ferromagnetic materials disturbing the local earth magnetic field can be detected and removed yielding accurate orientation estimation near these materials.

The filter is evaluated extensively by means of the camera-based system Vicon

(a) Aerospace sequence: roll, pitch and heading   (b) Joint rotation convention for a knee joint
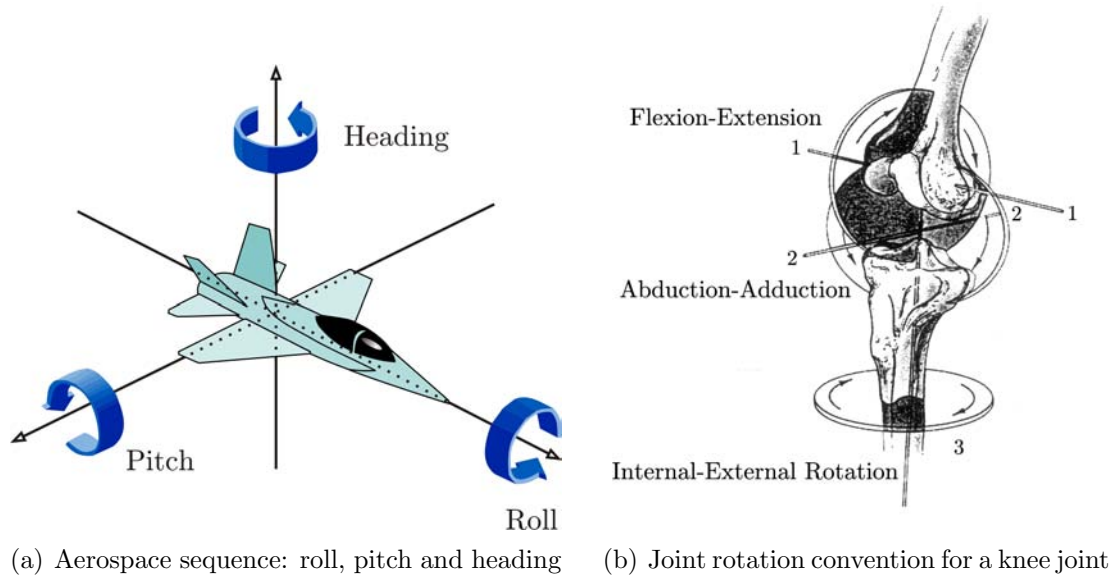
Figure 1.8 — Reference frames for navigation and clinical applications.

in **Chapter 3**. Three optical markers were attached to the inertial and magnetic sensor module and the orientation estimated by the Kalman filter was compared with the orientation obtained with the camera system. The sensor was placed on the lower arm of five subjects. They performed movements to simulate assembly line work near a large ferromagnetic object.

The fusion of a camera-based system and inertial sensors for accurate position estimation is presented in **Chapter 4**. The results can be used to improve dynamic performances beyond the limitations of the optical system and fill gaps of marker data in case of occlusion with inertial position estimates. Although these position estimates are still lab bound, it gives us important information on the characteristics of inertial position calculations and the design of the fusion filter for inertial aided on-body position estimates.

An on-body position aiding system is described in **Chapter 5**. It is a magnetic tracking device in which the source (coils) and power supply are worn on the user's body. The choice for a magnetic system was based on possibility to make this system portable and the transparency of the human body for magnetic fields. The performances of the 6 DOF estimates were compared with an optical tracking system by placing markers on the coils and sensor module. Several trade-offs in the design were investigated.

Magnetic pulsing requires a substantial amount of energy which limits the update rate and the magnetic field can easily be disturbed. Therefore, the system

is combined with inertial sensors in **Chapter 6**. In between magnetic updates, position and orientation changes are measured by inertial sensors. A Kalman fusion filter is designed and tested, based on the earlier developed structure, to fuse both 6 DOF estimates in an optimal way.

Finally, the thesis concludes with a general discussion in **Chapter 7**.

Chapter 2

Compensation of magnetic disturbances improves inertial and magnetic sensing of human body segment orientation

D. Roetenberg, H.J. Luinge, C.T.M. Baten and P.H. Veltink

2.1 Introduction

THE USE of miniature inertial sensors has become a common practice in ambulatory human movement analysis. Micro-machined gyroscopes and accelerometers are used in several applications which include monitoring of activities of daily living [18, 79, 70], assessment of internal mechanical working load in ergonomics studies [17, 15, 109, 11], measurement of neurological disorders [110, 72, 112, 115] and mixed and augmented reality [30, 8, 51]. It should be noted that there are important limitations in the current systems. The inherent drift of the orientation and position estimates limits long-term stable application of these sensors [36].

Typically, angular orientation is determined by integrating the output from the angular rate sensors. Microelectromechanical (MEMS) gyroscopes are accurate for angular velocity measurements but can only be used for a short time to calculate angular orientation. A relatively small offset error due to temperature effects on the gyroscope signal and noise will introduce large integration errors. Linear accelerometers measure the vector sum of acceleration **a** and gravitational acceleration **g** in sensor coordinates. The orientation calculated using the angular rate sensors can be used to express this vector sum in global coordinates. The gravitational acceleration component **g** is in most situations of human movement sensing dominant, thus providing inclination information [43, 12, 64]. This can be used to correct the drifted orientation estimate from the gyroscopes. The principles for orientation estimation of a moving human body segment by fusing miniature gyroscopes and accelerometers in a Kalman filter have been described by Luinge [66]. The results show accurate drift-free inclination estimation, though heading (or yaw) drift is the impeding factor for full 3D orientation measurement in this filter. Since accelerometers cannot detect rotations about the vertical axis, magnetic sensing can be added. The magnetometer is sensitive to the earth's magnetic field and can thus be used to correct drift of the gyroscope about the vertical axis. Bachmann [8] and Foxlin [30] have implemented filters in which accelerometers and magnetometers are used for low frequency components of the orientation and gyroscopes to measure faster changes in orientation. However, ferromagnetic materials, like iron, or other magnetic materials in the vicinity of the sensor will disturb the local magnetic field and will therefore cause large errors in the estimated orientation, especially in the heading direction. Also, other proposed methods to fuse the three different sensors do not take magnetic interferences into account [54, 68, 42]. In controlled measurement volumes like laboratories for gait or virtual reality, the magnetic field can be characterized *a priori*. However, in ambulatory applications with unknown materials and magnetic objects in the environment, inaccuracy in orientation estimation is very likely to occur.

In this study, the Kalman filter for body segment orientation by Luinge [63] is

extended with a magnetometer model which is preventing heading drift and is able to compensate for magnetic disturbances [94]. This chapter focuses on the filter design and the effects of ferromagnetic materials near the sensor under static and dynamic conditions.

2.2 Sensor fusion

A complementary Kalman filter was designed to estimate orientation by combining the signals of a complete 3D sensor module including three rate gyroscopes, three accelerometers and three magnetometers. The structure of the error estimation procedure is shown in Figure 2.1. The Kalman filter is useful for combining data from several different indirect and noisy measurements. Thus, while gyroscopes measure orientation by integrating angular velocities and the accelerometer (as an inclinometer) and magnetometer (as a compass) provide a noisy and disturbed but drift-free measurement of orientation, the Kalman filter weights the three sources of information appropriately with knowledge about the signal characteristics based on their models to make the best use of all the data from each of the sensors [30].
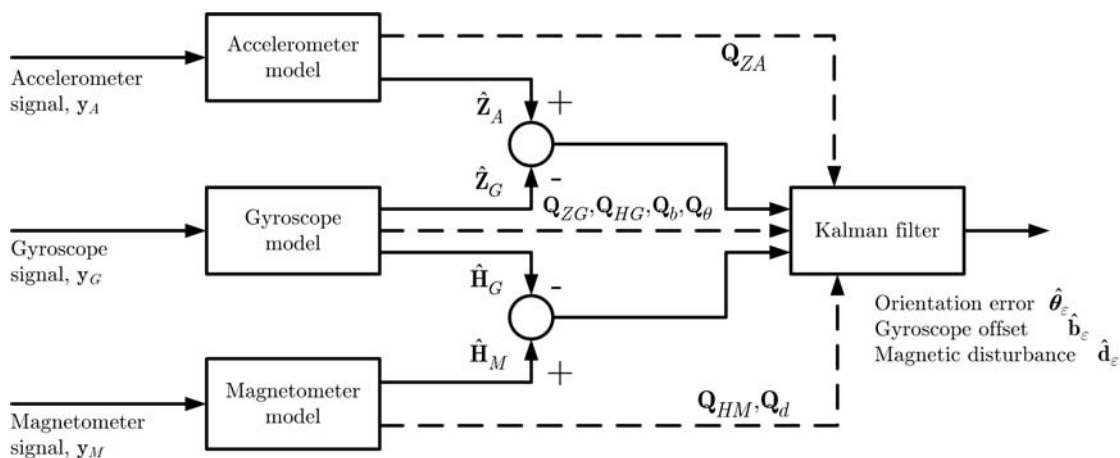
Figure 2.1 — Fusion of gyroscope $\mathbf{y}_G$, accelerometer $\mathbf{y}_A$, and magnetometer signals $\mathbf{y}_M$ in the error model for combined inertial and magnetic orientation sensing. $\hat{\mathbf{Z}}_A$ and $\hat{\mathbf{Z}}_G$ are the estimates of inclination by accelerometer and gyroscope, respectively, with $\mathbf{Q}_{ZA}$ and $\mathbf{Q}_{ZG}$ being the related error covariance matrices. $\hat{\mathbf{H}}_G$ and $\hat{\mathbf{H}}_M$ are the estimates of the global magnetic field vector by gyroscope and magnetometer, respectively, with $\mathbf{Q}_{HG}$ en $\mathbf{Q}_{HM}$ being the related error covariance matrices. Differences between the sensor estimates in $\mathbf{Z}$ and $\mathbf{H}$ are written as a function of the orientation error $\hat{\boldsymbol{\theta}}_\varepsilon$, gyroscope offset error $\hat{\mathbf{b}}_\varepsilon$ and magnetic disturbance error $\hat{\mathbf{d}}_\varepsilon$ and the related covariance matrices $\mathbf{Q}_\theta$, $\mathbf{Q}_b$, and $\mathbf{Q}_d$, the estimated errors by the Kalman filter are used to correct the estimated orientation and signal predictions, as illustrated in Figure 2.2.

From this combination or fusion of sensor signals, information is obtained regarding the offsets of the gyroscopes, accelerometers and magnetometers, which can be

used to recalibrate the sensors in use. The model of the measured gyroscope and acceleration signals is based on the following assumptions:

- A gyroscope measures a 3D angular velocity plus an offset and white measurement noise in the sensor coordinate frame.
- The spectrum of the gyroscope offset has a low bandwidth in comparison with the spectrum of the kinematic signals that are to be measured.
- A 3D accelerometer measures the sum of acceleration of the movement, gravitational acceleration (9.8 ms^{-2}) and a white noise component, all in the sensor coordinate frame.
- The acceleration of the body segment in the global system can be described as low-pass filtered white noise.

In this study, the following additional assumptions are used:

- A 3D magnetometer measures the earth magnetic field vector plus a white noise component.
- The magnetic field can be disturbed by nearby ferromagnetic materials or magnetic fields other than the earth magnetic field. The bandwidth of the disturbance is larger than the bandwidth of the gyroscope drift and is dependent of the movement.

The complementary Kalman filter is not based on the model of the process, but on a model of errors. The advantages are that this structure maintains the high dynamic response necessary for attitude state variables and most error processes in the inertial measurement units (IMU's) can be described by linear processes [16]. The four parts of the complementary filter are: the *a priori* model prediction of the state, the error model, the Kalman filter, and the state correction yielding the *a posteriori* state estimate (see Figure 2.2). A hat on top of symbol denotes an estimate, a minus superscript the *a priori* estimate that is made using the sensor model and a plus superscript an estimate that is made after correction by the filter.

2.2.1 Prediction model

The sensor is assumed to be attached to a human body segment that rotates and translates with respect to a global coordinate frame. The strapdown integration algorithm by Bortz [14] was used to calculate the change in orientation from an angular velocity. The orientation of the sensor with respect to the global coordinate frame G is expressed with a rotation matrix $\mathbf{R}$, containing the three unit vectors $\mathbf{X}$, $\mathbf{Y}$ and $\mathbf{Z}$ of the global coordinate system expressed in the sensor frame S:

$$^{GS}\mathbf{R} = \begin{bmatrix} {}^{S}\mathbf{X} & {}^{S}\mathbf{Y} & {}^{S}\mathbf{Z} \end{bmatrix}^{\mathrm{T}} \tag{2.1}$$
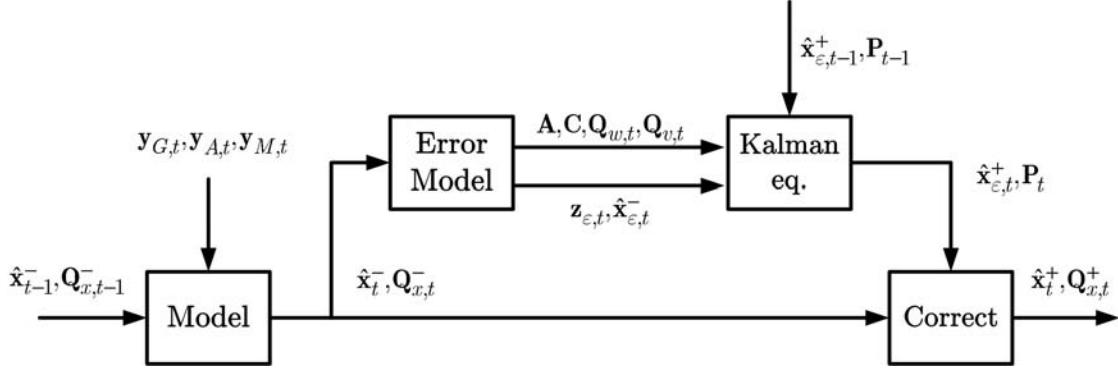
Figure 2.2 — Structure of complementary Kalman filter for orientation estimation. $\mathbf{x}$ is the vector featuring the states of the model used for the orientation estimation, whereas $\mathbf{x}_\varepsilon$ represents the errors in the model states: the gyroscope bias error, orientation error, and magnetic disturbance error. $\mathbf{Q}_x$ describes the covariance matrices of the filter states. Sensors signals are $\mathbf{y}_G$: gyroscope; $\mathbf{y}_A$: accelerometer; and $\mathbf{y}_M$: magnetometer, from which the filter measurement input $\mathbf{z}_\varepsilon$ can be calculated using the error model. In the model, the angular velocities are integrated to an angular orientation and the *a priori* signal predictions are made. $\mathbf{A}$, $\mathbf{C}$, $\mathbf{Q}_w$, and $\mathbf{Q}_v$ are matrices describing the error model and $\mathbf{P}$ is the covariance matrix used in the Kalman filter.

Gyroscope

The gyroscopes signals are described as the sum of the angular velocity $\boldsymbol{\omega}_t$, the offset $\mathbf{b}_t$ and a white noise term $\mathbf{v}_{G,t}$:

$$\mathbf{y}_{G,t} = \boldsymbol{\omega}_t + \mathbf{b}_t + \mathbf{v}_{G,t} \tag{2.2}$$

The slow variation of the gyroscope offset is modeled as a realization of a first order Markov process, driven by a white Gaussian noise vector:

$$\mathbf{b}_t = \mathbf{b}_{t-1} + \mathbf{w}_{b,t} \tag{2.3}$$

Accelerometer

The accelerometer signals are described as the sum of the acceleration $\mathbf{a}_t$, the gravity $\mathbf{g}_t$ and a white noise term $\mathbf{v}_{A,t}$:

$$\mathbf{y}_{A,t} = \mathbf{a}_t - \mathbf{g}_t + \mathbf{v}_{A,t} \tag{2.4}$$

The acceleration was modeled as a first order-low pass filtered white noise process according to:

$$\mathbf{a}_t = c_a \mathbf{a}_{t-1} + \mathbf{w}_{a,t} \tag{2.5}$$

where c_a, determining the cutoff frequency.

Magnetometer

The magnetometer signals are described as the sum of the earth magnetic field vector $\mathbf{m}_t$, a disturbance vector $\mathbf{d}_t$ and a white noise term $\mathbf{v}_{M,t}$:

$$\mathbf{y}_{M,t} = \mathbf{m}_t + \mathbf{d}_t + \mathbf{v}_{M,t} \tag{2.6}$$

The magnetic disturbance is modeled by the following Markov scheme:

$$\mathbf{d}_t = c_d \mathbf{d}_{t-1} + \mathbf{w}_{d,t} \tag{2.7}$$

$\mathbf{w}_{d,t}$ is the driving Gaussian noise with a standard deviation of $\boldsymbol{\sigma}_d$ and c_d is a constant between 0 and 1. In the vicinity of ferromagnetic materials or external magnetic fields, the magnetic flux is most likely to be higher or lower as can be seen in Figure 2.3. In real 3D space, the field distribution is of course more complicated, and, therefore, the magnetic dip angle φ_{mag} should also be taken into account in order to identify a disturbance. The magnetic dip angle, also called magnetic inclination, is the angle the earth magnetic field makes with the surface of the earth. This dip angle varies depending the position on the earth's surface [80].
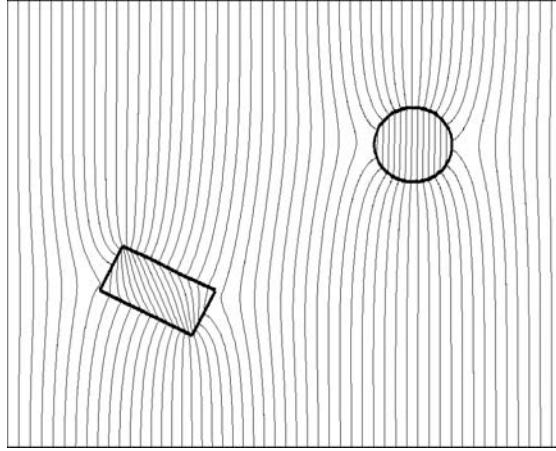
Figure 2.3 — Finite element simulation of ferromagnetic objects in free space with a homogeneous magnetic field. The objects have a permeability of 5000 times the permeability of free space ($4\pi \times 10^{-7}$ H/m). The field lines bend toward the objects, generally favoring a perpendicular angle of incidence with the ferromagnetic surface.

The magnetic inclination φ_{mag} is $0°$ at the magnetic equator and $90°$ at each of the magnetic poles. In the latter case, magnetometers do not provide any heading information, which makes correction of gyroscope drift around the vertical axes impossible. At the locations of our experiments, the magnetic dip angle φ_{mag} is about $67°$. When changes in magnetic flux and dip angle are measured, $\boldsymbol{\sigma}_d$ will be increased, since this is the driving component in estimating the disturbance vector

$\mathbf{d}_t$. The total flux $\|\mathbf{m}_t\|$ is calculated by taking the absolute value of the three magnetic sensor components:

$$\|\mathbf{m}_t\| = \sqrt{m_{x,t}^2 + m_{y,t}^2 + m_{z,t}^2} \tag{2.8}$$

Under non-disturbed conditions, this value is normalized to $\|\mathbf{m}_t\| = 1$. To calculate the magnetic dip angle, firstly the measured magnetic sensor signals should be expressed in the global frame using:

$$^G\mathbf{m}_t = {}^{GS}\mathbf{R}_t\,{}^S\mathbf{m}_t \tag{2.9}$$

Then the dip angle in the global frame is:

$$\varphi_{mag,t} = \arctan\left(\frac{{}^Gm_{z,t}}{\sqrt{{}^Gm_{x,t}^2 + {}^Gm_{y,t}^2}}\right) \tag{2.10}$$

If $\|\mathbf{m}_t\| = 1$ and $\varphi_{mag,t} = 67°$ there is a homogeneous magnetic field without ferromagnetic materials and the disturbance $\mathbf{d}_t$ equals zero:

$$\mathbf{d}_t = \begin{bmatrix} 0 & 0 & 0 \end{bmatrix} \tag{2.11}$$

When $\|\mathbf{m}_t\|$ and φ_{mag} change, $\mathbf{d}_t$ should change by updating $\boldsymbol{\sigma}_d$:

$$\boldsymbol{\sigma}_d = \boldsymbol{\sigma}_m \left|\|\mathbf{m}_t\| - \|\mathbf{m}_{t-1}\|\right| + \boldsymbol{\sigma}_\varphi \left|\varphi_{mag,t} - \varphi_{mag,t-1}\right| \tag{2.12}$$

where $\boldsymbol{\sigma}_m$ and $\boldsymbol{\sigma}_\varphi$ are vectors consisting of three equal components, which determine the contributions of the changes in total flux and dip angle respectively.

2.2.2 Filter structure

The Kalman filter uses a state space representation to model the relation between errors in estimated model variables and the error in the inclination and magnetic field vector predicted by the model. This relation is called an error state model and is governed by the linear stochastic difference equation [16]:

$$\mathbf{x}_{\varepsilon,t} = \mathbf{A}\mathbf{x}_{\varepsilon,t-1} + \mathbf{w}_t \tag{2.13}$$

with a measurement $\mathbf{z}$ that is:

$$\mathbf{z}_{\varepsilon,t} = \mathbf{C}\mathbf{x}_{\varepsilon,t} + \mathbf{v}_t \tag{2.14}$$

$\mathbf{w}_t$ and $\mathbf{v}_t$ represent the system and measurement noise respectively. They are assumed to be independent, white and with normal probability distributions and

are specified by the covariance matrices $\mathbf{Q}_{w,t}$ and $\mathbf{Q}_{v,t}$. Now, $\mathbf{x}_\varepsilon$, $\mathbf{A}$, $\mathbf{z}_\varepsilon$, $\mathbf{C}$ and the covariance matrices have to be determined. The most important factors causing an error in the orientation estimate are incorporated in the error state vector $\mathbf{x}_\varepsilon$. The first error state variable is the orientation error, since it is used as a starting point to obtain the next orientation by strapdown integration. The second error state variable is the gyroscope offset error, since a small offset error causes a dramatic effect on the estimated orientation. The last error state variable is the error in the magnetic disturbance vector.

$$\mathbf{x}_{\varepsilon,t} = \left[\begin{array}{ccc} \boldsymbol{\theta}_{\varepsilon,t} & \mathbf{b}_{\varepsilon,t} & \mathbf{d}_{\varepsilon,t} \end{array} \right]^{\mathrm{T}} \qquad (2.15)$$

The orientation error $\boldsymbol{\theta}_\varepsilon$ is defined as the angle and direction over which the actual sensor coordinate frame has to be rotated in order to coincide with the estimated sensor coordinate frame. Matrix $\mathbf{A}$ and noise component $\mathbf{w}_t$ describe the propagation of the *a priori* error state vector. They can be found by considering the effect of the unknown system components on the error state. In this complementary filter structure, the knowledge about previous errors is incorporated in the current state estimate. Consequently, there is no correlation between the *a priori* estimated errors between two timesteps. This means that *a priori* errors $\mathbf{b}_{\varepsilon,t}^-$, $\boldsymbol{\theta}_{\varepsilon,t}^-$ and $\mathbf{d}_{\varepsilon,t}^-$ do not depend on previous error states $\mathbf{b}_{\varepsilon,t-1}^-$, $\boldsymbol{\theta}_{\varepsilon,t-1}^-$ and $\mathbf{d}_{\varepsilon,t-1}^-$. Therefore the $\mathbf{A}$ matrix equals the zero matrix. The error estimate is updated with measurement information according to:

$$\hat{\mathbf{x}}_{\varepsilon,t}^+ = \hat{\mathbf{x}}_{\varepsilon,t}^- + \mathbf{K}_t \left(\mathbf{z}_{\varepsilon,t} - \mathbf{C}\hat{\mathbf{x}}_{\varepsilon,t}^- \right) \qquad (2.16)$$

where the Kalman gain matrix $\mathbf{K}$ is computed from the estimation error covariance matrix, according to:

$$\mathbf{K}_t = \mathbf{P}_t^- \mathbf{C}^{\mathrm{T}} \left(\mathbf{C}\mathbf{P}_t^- \mathbf{C}^{\mathrm{T}} + \mathbf{Q}_{v,t} \right)^{-1} \qquad (2.17)$$

and $\mathbf{P}$ is updated according to the Ricatti equation:

$$\mathbf{P}_{t+1} = \mathbf{A}(\mathbf{I} - \mathbf{K}_t\mathbf{C})\mathbf{P}_t\mathbf{A}^{\mathrm{T}} + \mathbf{Q}_{w,t+1} \qquad (2.18)$$

Since matrix $\mathbf{A}$ equals zero, the Ricatti equation simplifies to:

$$\mathbf{P}_{t+1} = \mathbf{Q}_{w,t+1} \qquad (2.19)$$

Matrix $\mathbf{C}$ and noise $\mathbf{v}_t$ describe the relation between the error states and the measurements (Kalman filter input). They can be found by considering the effect of the gyroscope offset, orientation error and magnetic disturbance on the inclination and magnetic vector estimates. The filter has therefore two different inputs. A sensor signal generation model was developed to make two estimates of inclination

[63], one based on the gyroscope signals $\mathbf{Z}_G$ and one based on the accelerometer signals $\mathbf{Z}_G$, (see Figure 2.1):

$$\mathbf{z}_{\varepsilon,inclination,t} = {}^S\hat{\mathbf{Z}}_{A,t} - {}^S\hat{\mathbf{Z}}_{G,t} \tag{2.20}$$

The same principle of the inclination sensor signals generation model was applied for the estimation of the global magnetic vector. Both magnetometer $\mathbf{H}_M$ and gyroscope $\mathbf{H}_G$ systems make an estimate of the magnetic field vector:

$$\mathbf{z}_{\varepsilon,magnetic,t} = {}^S\hat{\mathbf{H}}_{M,t} - {}^S\hat{\mathbf{H}}_{G,t} \tag{2.21}$$

The error input can be formed by combining equations 2.20 and 2.21 in one vector:

$$\mathbf{z}_{\varepsilon,t} = \begin{bmatrix} \mathbf{z}_{\varepsilon,incl,t} & \mathbf{z}_{\varepsilon,mag,t} \end{bmatrix}^{\mathrm{T}} \tag{2.22}$$

The inclination estimate from the accelerometer is calculated by subtracting the predicted acceleration $\hat{\mathbf{a}}_t^-$ from the accelerometer signal to obtain the gravity vector. The gravity vector is normalized to obtain an estimate of the inclination vector:

$$\begin{aligned} {}^S\hat{\mathbf{Z}}_{A,t}^- &= \frac{\mathbf{y}_{A,t} - {}^S\hat{\mathbf{a}}_t^-}{\left|\mathbf{y}_{A,t} - {}^S\hat{\mathbf{a}}_t^-\right|} \\ &= {}^S\mathbf{Z}_t + \frac{1}{\mathrm{g}}\left(-{}^S\hat{\mathbf{a}}_t \times \hat{\boldsymbol{\theta}}_{\varepsilon,t}^- - c_a {}^S\hat{\mathbf{a}}_{\varepsilon,t-1}^+ + \mathbf{w}_{a,t} + \mathbf{v}_{A,t}\right) \end{aligned} \tag{2.23}$$

with ${}^S\mathbf{Z}_t$ being the correct inclination vector at time t, ${}^S\hat{\mathbf{a}}_t \times \hat{\boldsymbol{\theta}}_{\varepsilon,t}^-$ the effect of the orientation error on the acceleration estimate and $c_a {}^S\hat{\mathbf{a}}_{\varepsilon,t-1}^+$ the effect of the previous acceleration error. The estimate of ${}^S\hat{\mathbf{H}}_{M,t}^-$ is the measured magnetic vector subtracted by the estimated magnetic disturbance vector ${}^S\hat{\mathbf{d}}_t^-$:

$$\begin{aligned} {}^S\hat{\mathbf{H}}_{M,t}^- &= \mathbf{y}_{M,t} - {}^S\hat{\mathbf{d}}_t^- \\ &= {}^S\mathbf{H}_t - {}^S\hat{\mathbf{d}}_t \times \hat{\boldsymbol{\theta}}_{\varepsilon,t}^- - c_d {}^S\hat{\mathbf{d}}_{\varepsilon,t-1}^+ + \mathbf{w}_{d,t} + \mathbf{v}_{M,t} \end{aligned} \tag{2.24}$$

with ${}^S\mathbf{H}_t$ being the correct normalized magnetic vector at time t, ${}^S\hat{\mathbf{d}}_t \times \hat{\boldsymbol{\theta}}_{\varepsilon,t}^-$ the effect of the orientation error on the magnetic disturbance estimate and $c_d {}^S\hat{\mathbf{d}}_{\varepsilon,t-1}^+$ the effect of the previous magnetic disturbance error. To define the inclination estimate ${}^S\hat{\mathbf{Z}}_{G,t}$ and magnetic vector ${}^S\hat{\mathbf{H}}_{G,t}$ from the gyroscopes, first the orientation after one integration step has to be calculated. Because the errors in the predicted error state are small compared to the actual signals, only first order approximations of the error models are made. For small errors, the relation between the actual and estimated orientation is given by [14]:

$$ {}^{GS}\hat{\mathbf{R}} = {}^{GS}\mathbf{R}\left(\mathbf{I} + [\boldsymbol{\theta}_\varepsilon\times]\right) \tag{2.25}$$

The matrix cross product operator is given by:

$$[\boldsymbol{\theta}\times] = \begin{bmatrix} 0 & -\theta_z & \theta_y \\ \theta_z & 0 & -\theta_x \\ -\theta_y & \theta_x & 0 \end{bmatrix} \tag{2.26}$$

The orientation can be found by considering a first order approximation of a strapdown integration step:

$$^{GS}\hat{\mathbf{R}}_t^- = {}^{GS}\mathbf{R}_{t-1}^+ + {}^{GS}\mathbf{R}_{t-1}^+ \left[T\hat{\boldsymbol{\omega}}_t^- \times\right] \tag{2.27}$$

where T is the sample time. By substituting the angular velocity estimate from 2.2 into the previous equation and neglecting products of errors, it follows that the error propagation $\boldsymbol{\theta}_{\varepsilon,t}$ is described by:

$$\boldsymbol{\theta}_{\varepsilon,t}^- = \boldsymbol{\theta}_{\varepsilon,t-1}^+ - T\mathbf{b}_{\varepsilon,t-1}^+ + T\mathbf{v}_{G,t} \tag{2.28}$$

For the inclination estimate, the strapdown integration can be approximated with:

$$\begin{aligned}
^S\hat{\mathbf{Z}}_{G,t}^- &= {}^S\hat{\mathbf{Z}}_{t-1}^+ - T{}^S\hat{\boldsymbol{\omega}}_t \times {}^S\hat{\mathbf{Z}}_{t-1}^+ \\
&\approx {}^S\mathbf{Z}_t + {}^S\hat{\mathbf{Z}}_{t-1} \times \hat{\boldsymbol{\theta}}_{\varepsilon,t-1}^+ - T{}^S\hat{\mathbf{Z}}_{t-1} \times \hat{\mathbf{b}}_{\varepsilon,t-1}^+ + {}^S\hat{\mathbf{Z}}_{t-1} \times T\mathbf{v}_{G,t}
\end{aligned} \tag{2.29}$$

The gyroscope-based estimated magnetic vector is obtained similarly to the inclination:

$$\begin{aligned}
^S\hat{\mathbf{H}}_{G,t}^- &= {}^S\hat{\mathbf{H}}_{t-1}^+ - T{}^S\hat{\boldsymbol{\omega}}_t \times {}^S\hat{\mathbf{H}}_{t-1}^+ \\
&\approx {}^S\mathbf{H}_t + {}^S\hat{\mathbf{H}}_{t-1} \times \hat{\boldsymbol{\theta}}_{\varepsilon,t-1}^+ - T{}^S\hat{\mathbf{H}}_{t-1} \times \hat{\mathbf{b}}_{\varepsilon,t-1}^+ + {}^S\hat{\mathbf{H}}_{t-1} \times T\mathbf{v}_{G,t}
\end{aligned} \tag{2.30}$$

Now, the $\mathbf{C}$ matrix can be defined:

$$\begin{aligned}
\mathbf{z}_{\varepsilon,t} &= \begin{bmatrix} ^S\mathbf{Z}_{A,t} - {}^S\mathbf{Z}_{G,t} \\ ^S\mathbf{H}_{M,t} - {}^S\mathbf{H}_{G,t} \end{bmatrix} \\
&= \mathbf{C} \begin{bmatrix} \boldsymbol{\theta}_{\varepsilon,t} \\ \mathbf{b}_{\varepsilon,t} \\ \mathbf{d}_{\varepsilon,t} \end{bmatrix} + \mathbf{v}_t
\end{aligned} \tag{2.31}$$

with $\mathbf{C}$ being a 6×9 matrix:

$$\mathbf{C} = \begin{bmatrix} \left[\left(-{}^S\hat{\mathbf{Z}}_t - \frac{1}{g}{}^S\hat{\mathbf{a}}_t^-\right)\times\right] & \left[T{}^S\hat{\mathbf{Z}}_t\times\right] & \mathbf{0}_3 \\ \left[\left(-{}^S\hat{\mathbf{H}}_t - {}^S\hat{\mathbf{d}}_t^-\right)\times\right] & \left[T{}^S\hat{\mathbf{H}}_t\times\right] & -c_d\mathbf{I}_3 \end{bmatrix} \tag{2.32}$$

$\mathbf{I}_3$ is the 3×3 identity matrix and $\mathbf{0}_3$ the 3×3 zero matrix. The noise term $\mathbf{v}_t$ is described by:

$$\mathbf{v}_t = \begin{bmatrix} \frac{1}{g}\left(-c_a{}^S\hat{\mathbf{a}}_{\varepsilon,t-1}^+ + \mathbf{v}_{A,t} + \mathbf{w}_{a,t}\right) - {}^S\hat{\mathbf{Z}}_t \times T\mathbf{v}_{G,t} \\ \mathbf{w}_{d,t} + \mathbf{v}_{M,t} - {}^S\hat{\mathbf{H}}_t \times T\mathbf{v}_{G,t} \end{bmatrix} \tag{2.33}$$

2.2.3 Covariance matrices

The error covariance matrix $\mathbf{Q}_{w,t}$ of the system noise term $\mathbf{w}_t$ can be found using the knowledge the $\mathbf{A}$ matrix equals the zero matrix and by taking the variances of the error propagations 2.28:

$$\mathbf{Q}_{w,t} = \begin{bmatrix} \mathbf{Q}_{\theta,t-1}^+ + T^2\mathbf{Q}_{b,t-1}^+ + T^2\mathbf{Q}_{vG,t} & T^2\mathbf{Q}_{b,t-1}^+ & 0 \\ T^2\mathbf{Q}_{b,t-1}^+ & \mathbf{Q}_{b,t-1}^+ + \mathbf{Q}_{wb,t} & 0 \\ 0 & 0 & c_d^2\mathbf{Q}_{d,t-1}^+ + \mathbf{Q}_{wd,t} \end{bmatrix}$$
$$(2.34)$$

where $\mathbf{Q}_{\theta,t-1}^+$, $\mathbf{Q}_{b,t-1}^+$ and $\mathbf{Q}_{d,t-1}^+$ are the *a posteriori* error covariance matrices of the orientation, offset and magnetic disturbance at the previous timestep, respectively. $\mathbf{Q}_{vG,t}$ is the gyroscope noise covariance matrix, $\mathbf{Q}_{wb,t}$ the covariance matrix of the offset noise $\mathbf{w}_{b,t}$ and $\mathbf{Q}_{wd,t}$ the covariance matrix of the driving noise $\mathbf{w}_{d,t}$ of the magnetic disturbance. The term $\mathbf{Q}_{vG,t}$ was found by assuming that the gyroscope noise variance is equal in the X-Y and Z direction. In this case, the noise covariance matrix does not change when the noise is expressed in a different reference system. The measurement noise covariance $\mathbf{Q}_{v,t}$ was found by taking the covariances of Equation 2.33:

$$\mathbf{Q}_{v,t} = \begin{bmatrix} \frac{1}{g^2}\left(c_a^2\mathbf{Q}_{a,t-1}^+ + \mathbf{Q}_{wa,t} + \mathbf{Q}_{vA,t}\right) + \mathbf{Q}_{vG,t} \\ \mathbf{Q}_{wd,t} + \mathbf{Q}_{vM,t} + \mathbf{Q}_{vG,t} \end{bmatrix} \qquad (2.35)$$

with $\mathbf{Q}_{a,t-1}^+$ being the *a posteriori* acceleration error covariance matrix, $\mathbf{Q}_{wa,t}$ the covariance matrix of $\mathbf{w}_{a,t}$, $\mathbf{Q}_{vA,t}$ the covariance of the accelerometer measurement noise vector $\mathbf{v}_{A,t}$ and $\mathbf{Q}_{vM,t}$ the covariance of the magnetometer measurement noise vector $\mathbf{v}_{M,t}$.

2.3 Experimental methods

The purpose of the experiments was to investigate the accuracy, stability and reproducibility of the orientation estimation under various conditions. For the experiments, a MT9-A (Xsens Motion Technologies, see Figure 2.4) inertial and magnetic sensor module was used. The module consisted of three orthogonally placed angular rate sensors (Murata ENC03J), 3D linear acceleration sensors (Analog Devices ADXL202E), 3D magnetoresistive sensors (Philips KMZ51 and KMZ52) and an ambient temperature sensor. All sensor signals were sampled at 100 Hz with 16 bits. An anti-aliasing filter of 50 Hz was applied to the gyroscopes. Accelerometers and magnetometers were low-passed filtered at 10 Hz, all with second order filters. The calibration procedure to obtain the gains, offsets and non-orthogonality of accelerometers, gyroscopes and magnetometers was performed by the manufacturer of the sensor module and was based on Ferraris [29].
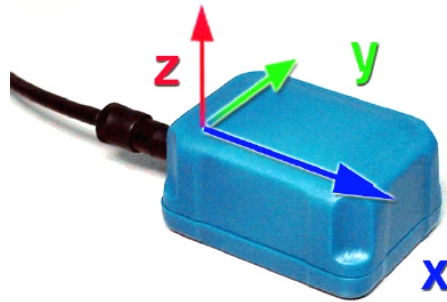
Figure 2.4 — MT9-A module consisting of 3D gyroscopes, 3D accelerometers, 3D magnetometers and a temperature sensor. The dimensions of the module are 39 * 54 * 28 mm (W * L * H) and the weight is 40 grams. The sensor frame is indicated by XYZ.

The stability of the filter was first investigated under static conditions. An iron cylinder of 3.75 kg was placed near the sensor module for 10 minutes without moving the sensor. The second quasi-static tests implied rotations of + and - 90° along the three axes. To ensure exact angles of rotations, the sensor module was fixed in an aluminum (not ferromagnetic) cubic frame. The definition of the sensor frame S can be found in Figure 2.4. After each rotation, the module was not moved for two to four seconds. The sensor module was first rotated 90° and -90° along the X-axis, followed by -90° and 90° along the Y-axis. It was then rotated 90° along the Z-axis, and -90° back to its original orientation. After these rotations, the iron cylinder was placed at 5 cm of the module and a new sequence of rotations was performed in opposite directions. The iron was then taken away and the sensor was rotated 90° along the X-axis and -90° back. The angles as calculated by the Kalman filter were compared with the physical orientation of the sensor in the aluminum frame. In the final set of experiments, a relatively simple human body movement was executed. For this, the sensor module was placed on the wrist of a subject and the arm was flexed and extended repetitively. This movement could easily be evaluated and the signals showed typical human accelerations and angular velocities. A linear calibrated potentiometer (MCB, PP27, 10kΩ) was fixed at the elbow joint and aligned with the sensor module as a reference measurement. The potentiometer had an accuracy of 1 % and was sampled with the AD converter inside the sensor module with 16 bits resolution and stored as an additional channel. The elbow was placed on a table, the upper arm was kept static and the lower arm was moved in the ^{G}XZ plane with the wrist in neutral position (see Figure 2.5). The movement was repeated 20 times at 0.25, 0.5, 1.0 and 2.0 Hz using a metronome with 5.0 kg of iron placed on the table at distances of 5 and 10 cm from the sensor and without iron. All experiments were repeated 10 times.
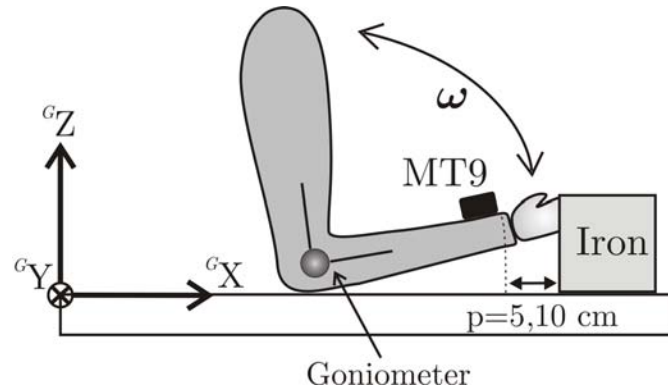
Figure 2.5 — Experimental setup for dynamic orientation estimation. The elbow is fixed on the table and the lower-arm is moved in the X-Z plane at different speeds. This is repeated with 5.0 kg of iron placed in front of the hand at 5 and 10 cm when the lower arm was lying on the table.

Before using the filter, the model parameter c_a was estimated by analyzing typical accelerations [63] of several movements. The parameter c_d was obtained by characterizing the disturbances by moving the sensor module at different speeds and distances from ferromagnetic materials. The sensor noise variances $\mathbf{Q}_{vA}$, $\mathbf{Q}_{vG}$ and $\mathbf{Q}_{vM}$ were found by taking the variances of the sensor signals while the sensor was lying still. These parameters were not changed during the experiments.

2.4   Results

The 10-minute static tests showed no drift or interference problems. The accuracy was 0.6° root mean square (rms) with a standard deviation (std. dev.) of 0.3°. Figure 2.6 shows the signal norms of the accelerometers and magnetometers of one typical trial of the quasi-static experiments. The acceleration norm shows a constant value of approximately 9.8 ms^{-2} with peaks at the moments of rotation. The magnetic norm has a value of approximately 1 when no iron is near the sensor. When the iron mass is moved toward the sensor (marked by the arrow) the magnetic disturbance can be detected.

In Figure 2.7, the Euler angles along the three axes are given when only the angular velocities from the gyroscopes are integrated. It can be seen that the integration drift is between 10 - 25° after one minute. Although the calculations for orientations are not performed using Euler angles, for obvious reasons like singularities, these results are presented in this way for better interpretation. Obviously, there is no magnetic disturbance noticeable since the gyroscopes are not interfered by ferromagnetic materials. Figure 2.8 shows the output from the same motion sequence when a Kalman filter is used with all three types of sensors but no magnetic
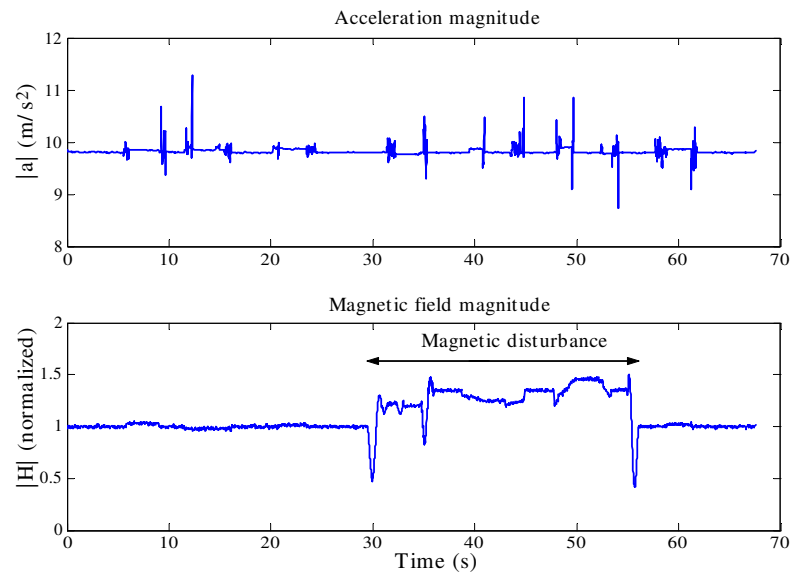
Figure 2.6 — Signal norms of the accelerometers (upper) and magnetometers (lower) of a typical quasi-static trial. The acceleration norm is approximately 9.8 m/s^2. The peaks occur during the moments of rotation. The norm of the magnetic field is approximately 1 when the earth magnetic field in not disturbed. Then an iron cylinder is placed near the sensor module from 30 to 55 seconds and the disturbance can be detected. After the cylinder is removed, the norm is 1 again.
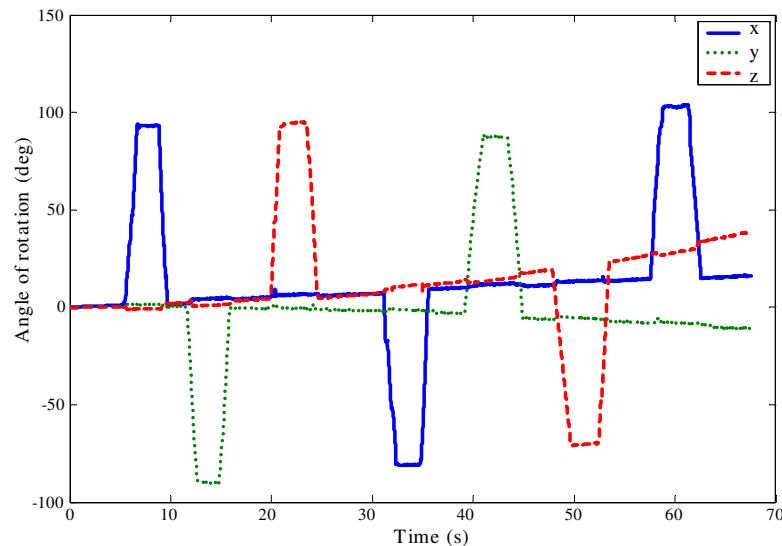
Figure 2.7 — Euler angle presentation of rotations around the X (solid), Y (dot) and Z (dashed) axes when only the gyroscope angular velocities are integrated. After a few seconds the drift error becomes significant.
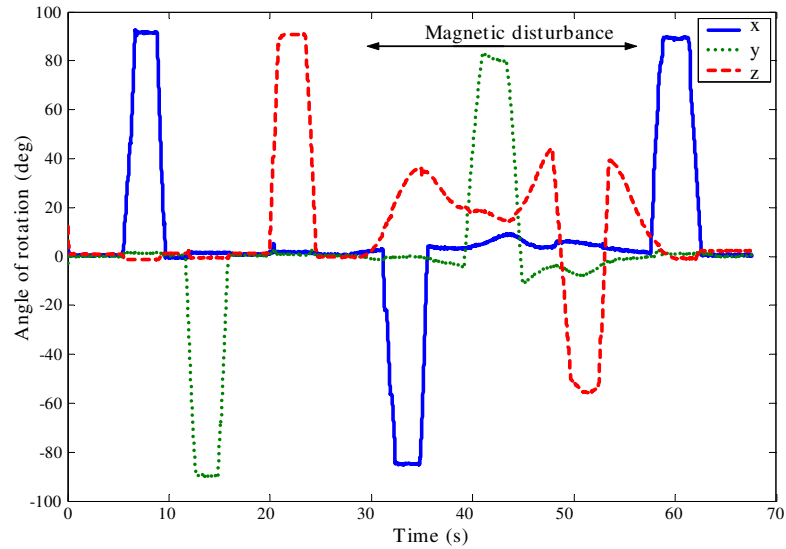
Figure 2.8 — Angles of rotation with a Kalman filter with equal weight to gyroscopes, accelerometers and magnetometers. No magnetic disturbance compensation is applied and the errors become quite large during the period of interference (marked by the arrow).
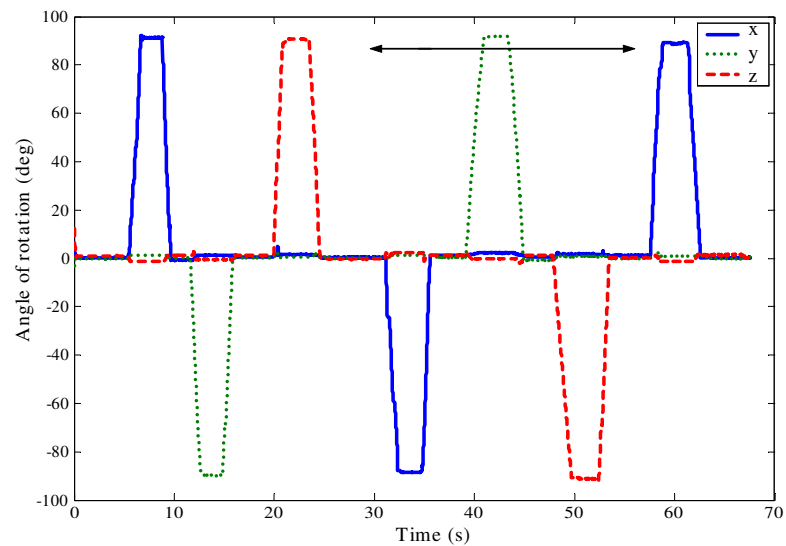
Figure 2.9 — Angles of rotation with the full Kalman filter featuring the magnetic disturbance compensation. During the period of interference (marked by the arrow) the output is not disturbed and the whole trial is drift-free.

disturbance compensation is applied. From the start of the interference, the error becomes significant. When the iron is removed, the rotation around the Z-axis slowly convergences back to its original orientation. The interference can also be observed in the X and Y (inclination) components, because of the influence on the magnetic dip angle.

Figure 2.9 illustrates the effect of the magnetic signal model and the Kalman filter on the same signals. The output of the Kalman filter is drift-free, not disturbed by the iron and the rotations are estimated accurately.

In Figure 2.10, the distribution of the errors of the quasi-static experiments is presented in box plots. The errors are defined as the angle over which the filter output has to be rotated to coincide with the actual angles of rotation of the sensor in the frame during all static parts. The first box A shows the static errors of the full Kalman filter with magnetic disturbance compensation during the parts when no ferromagnetic materials were near the sensor. It was normally distributed with a mean of 1.3° and a standard deviation of 0.4. Box B shows the results of the full Kalman filter during the parts where the magnetic field was disturbed by the iron object. The mean error was now 1.5° (std. dev. 0.45). In the middle box C, the errors are shown where a Kalman filter was used without compensation and no disturbances were present. The errors were equal to the full Kalman filter without the disturbance, namely 1.3° (std. dev. 0.4). Box D indicates that the Kalman filter without magnetic disturbance compensation had big errors up to 40° when iron is placed near the sensor module. In many practical applications, this is not acceptable. The errors when only the angular velocities of the gyroscopes were integrated during 60 seconds are plotted in the fifth bar E. It should be noted that the error in gyroscope integration is depending on the length of the trial. Increasing the duration of the trial will increase the gyroscope drift error. There was a significant difference (Friedman Anova and posthoc test Wilcoxon, p<0.01) between the orientation estimates with compensation and the orientation estimates without compensation and only gyroscope integration at the periods of magnetic interference. Between methods A, B and C, no significant differences were found.

In Figure 2.11, the dynamic errors from the arm movement together with their standard deviations are plotted when the full Kalman filter with compensation is used. The errors were calculated by taking the rms values of the differences between the filter output and the angle of the potentiometer during the movement. It can be seen that the errors increase from 1.3° to about 2.4° when the iron comes closer to the sensor module. If a Kalman filter without the magnetic disturbance compensation was used, errors up to 40° were measured. There was a significant difference between the trials without iron and with iron (Friedman Anova and posthoc test Wilcoxon, p<0.01), but between the trials with iron no significant difference was found. The graph also shows that the errors get slightly bigger as the speed of the movement increases; however no significant differences were found.

34
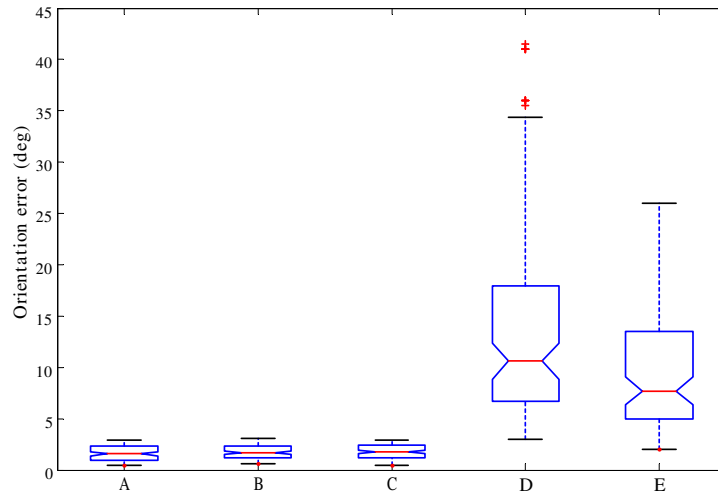
Figure 2.10 — Orientation estimation errors of quasi static experiments with magnetic interference presented in box plots. The boxes have lines at the lower quartile, median, and upper quartile values. The whiskers are lines extending from each end of the box to show the extent of the rest of the data. Outliers are marked with the + signs.
Box A: static errors of the full Kalman filter with magnetic disturbance compensation during the parts when no ferromagnetic materials were near the sensor.
Box B: full Kalman filter during the parts with magnetic disturbances.
Box C: Kalman filter without the disturbance compensation model and no ferromagnetic materials near the sensor module.
Box D: Kalman filter without the disturbance compensation model with ferromagnetic materials near the sensor module.
Box E: Orientation errors by integrating gyroscope signals during 60 seconds using a strapdown integration algorithm.
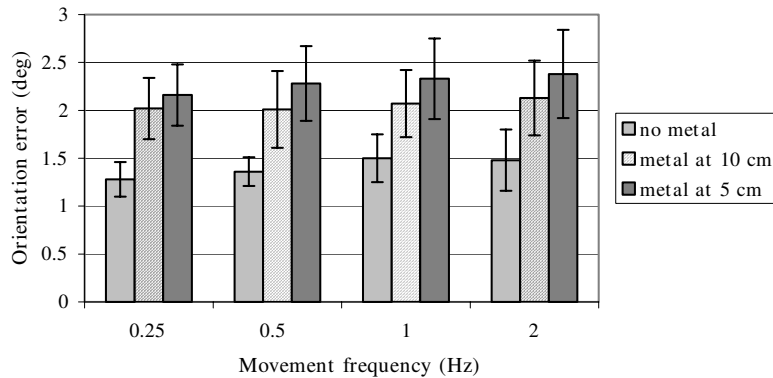
Figure 2.11 — Orientation estimation errors of dynamic experiments without iron, iron placed at 5 cm and 10 cm at different frequencies of the arm flexion movement. The full Kalman filter is used.

2.5   Discussion

This chapter proposes a method for fusion of gyroscope, accelerometer and magnetometer signals to estimate orientation of human body segments. The combination of the three types of sensor signals for human motion analysis has been reported previously [30, 54, 8, 68, 42]. However, magnetic interference has not been taken into account in these filters and large errors will occur in the vicinity of ferromagnetic objects. The performances of the method proposed in this chapter have been tested under static, quasi-static and dynamic conditions. The results show a significant improvement of orientation estimates using the magnetic interference correction and the filter overcomes both sensor and electronics drift. The structure of the complementary filter, where only three factors ($\boldsymbol{\theta}_\varepsilon$, $\mathbf{b}_\varepsilon$ and $\mathbf{d}_\varepsilon$) have to be estimated enables fast real time implementation. From the experiments and literature [10], it can be found the accuracy of the dynamic orientation measurements is sensitive to several factors, namely: the speed and type of movement, often depending on the body segment on which the sensor module is placed and the environment, which means: the distance to the ferromagnetic material, type, mass and geometry. The errors measured varied between 1.3° and 2.4° (std. dev. 0.5). In this study, the orientation filter was tested under well-controlled and limited conditions. The dynamic test was performed only in one direction. To fully assess the system, 3D movements should be compared with an external tracking (e.g. camera) reference system. This will be presented in the next chapter.

In case a sensor module is placed at a fixed distance near ferromagnetic materials, like on prostheses or on tools, the magnetic sensors should be calibrated under these conditions. Soft and hard iron effects as described in [19] should then be taken into account. More ferromagnetic materials in the measurement volume will decrease the filter performance. The accuracy could also decrease if the disturbance has the same low bandwidth as the gyroscope heading drift or the magnetic field is constantly disturbed. The distinction between heading drift and disturbance is then difficult to make. However, since the magnetic disturbance is modeled as an autoregressive process, these errors are limited. If the sensors are used for example in a moving vehicle, the accelerometer model should be modified. Accelerations of the vehicle will most likely be different from human accelerations solely, resulting in wrong inclination estimates. The acceleration error $\mathbf{a}_\varepsilon$ was not modeled as a Kalman state since this error hardly influences the inclination estimate. The estimation of the acceleration $\mathbf{a}$ by using the signal prediction model showed stable and accurate results. If a more accurate estimate of the acceleration $\mathbf{a}$ is desired, it could be taken into account in the Kalman filter.

The proposed model and Kalman filter can be applied to any combination of inertial and magnetic sensors. In principle, only the specifications of the sensors have to be known, like noise and drift. As MEMS techniques improve, the next

generation of gyroscopes will suffer less from drift [102, 3, 117]. This means the accelerometer and magnetometer filter weights can be reduced, resulting in less interference problems. The temperature sensor was only used as a global indication of the stability of the temperature inside the whole sensor module. For accurate temperature drift compensation, a temperature sensor should be mounted directly on the gyroscopes and accelerometers and a temperature model should be available.

In conclusion, the proposed Kalman filter implementation shows accurate and drift free 3D orientation estimates with the capability to correct for magnetic interferences.

Chapter 3

Evaluation of orientation measurements

D. Roetenberg, C.T.M. Baten and P.H. Veltink
based on [92], accepted for publication in
IEEE Trans. on Neural Systems and Rehabilitation Engineering

3.1 Introduction

IN REHABILITATION, ergonomics and sports physiology, posture and movement analysis is one of the central assessment tools [119, 56, 107]. Current state-of-the-art technology allows accurate motion analysis in fixed laboratory setups. Under field conditions, for example at the actual work place during actual work, possibilities are limited. Gyroscopes are often combined with accelerometers, used as an inclinometer, and magnetometers, used as a compass, for stable orientation measurements. Ferromagnetic materials, like iron, and other magnetic materials in the vicinity of the sensor will disturb the direction and density of local earth magnetic field and will therefore distort these orientation measurements [120]. This magnetic interference impedes many applications with ferromagnetic materials in an unknown surrounding. These materials are encountered in many work places, for example in back load estimation for ergonomic purposes at assembly lines [28]. In the previous chapter, an algorithm has been described for orientation estimation of human motion featuring magnetic disturbance compensation. The orientation filter was tested under well-controlled conditions. In this study [91], the orientation output obtained with this Kalman-based filter using the three-dimensional inertial and magnetic sensors is validated against a laboratory bound opto-kinetic system in a simulated assembly line work environment.

3.2 Methods

The complementary Kalman-based filter was used to estimate the orientation by combining 3D gyroscope, accelerometer and magnetometer signals using a model of the system and relevant signals. When no ferromagnetic materials are present near the sensor module, the local earth magnetic field presents a good reference. The total magnetic flux and the dip angle of the magnetic field are constant in this homogeneous field and are used as a measure of disturbance. In case of a detection of a magnetic disturbance, less weight is assigned to the magnetometers and the estimation relies more on the gyroscopes and accelerometers.

3.2.1 Measurement set-up

The algorithm previously described was tested in experiments by comparing the orientation as calculated by the filter to the orientation that was obtained by a laboratory bound 3D optical tracking system Vicon 370 (Oxford Metrics) consisting of 6 cameras operating at 50 Hz. The calibrated volume size was 4000 * 2000 * 2000 mm. The error is defined as the smallest angle about which the estimated orientation by the Kalman-based filter has to be rotated to coincide with the orien-
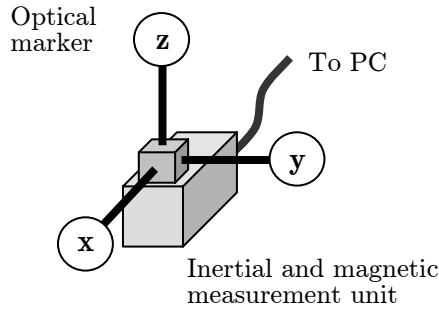
Figure 3.1 — Inertial and magnetic sensor module with three orthogonally placed optical markers.

tation obtained by the reference system. Three optical markers with a diameter of 25 mm were securely attached in an orthogonal arrangement to the sensor module on 10 cm carbon fiber sticks to measure the sensor orientation (see Figure 3.1). For the experiments, a MT9-A (Xsens Motion Technologies) inertial and magnetic sensor module was used. The signals of the sensors were sampled at 100 Hz with 16-bit resolution and stored together with a synchronization signal on a handheld computer.

To compare the orientation obtained using the inertial and magnetic sensors with the optical reference system, the relation between both coordinate systems had to be determined by means of a rotation. Firstly, the marker coordinate frame was constructed from the three measured marker positions in the global reference frame. The orientation of the sensor frame with respect to the marker frame was found by using two instances with different orientations in which the accelerometer was measured while the sensor was held still. When the accelerometer is not moving, the measured output will point in vertical direction, which is along the global reference Z-axis. The magnetic field was used for the heading reference. The orientation of the body segment in the global reference frame $^{GS}\mathbf{R}$ was obtained using:

$$^{GS}\mathbf{R} = {}^{GM}\mathbf{R}{}^{MS}\mathbf{R} \tag{3.1}$$

where $^{GM}\mathbf{R}$ is the orientation matrix describing the rotation from global to marker frame and $^{MS}\mathbf{R}$ is the orientation matrix describing the rotation from marker to sensor frame.

3.2.2 Experiments

The comparison of the Kalman-based filter with the reference system was performed with a number of experiments. In the first experiment, the sensor module with the attached markers was placed on a 50 cm long wooden stick and moved

Figure 3.2 — Experimental set-up: the sensors module was placed on the wrist of the subject. Markers for the video-based reference system are indicated by the reflective dots. The object in front of the subject is an iron case that induced magnetic disturbances to the sensor measurements.

by hand near a large iron tool case. The movements consisted of small and large rotations along multiple axes at different velocities and different distances from the ferromagnetic case. In the following experiments, the sensor module with optical markers was placed on the wrist of five different subjects. For each subject eight trials were recorded, varying from half a minute to five minutes. Each trial began with three seconds without movement to obtain the initial sensor offsets. In the first two trials, the subject performed ab/adduction and flexion/extension of the arm without ferromagnetic materials in the measurement volume. In the second set of two trials, the same arm movements were now performed near a large metal (steel) case (see Figure 3.2). Dimensions of the case were 70 * 35 * 90 cm (W * D * H). The third set of five trials consisted of simulated assembly line work. The subject was asked to pack and unpack small objects from a carton box that was positioned on the metal case. In two of these trials, after one minute the subject took one step back from the metal case for five seconds. These experiments were processed with the described Kalman-based filter with and without the magnetic disturbance model.

3.3   Results

The gyroscope, accelerometer and magnetometer signals of a typical trial of the first set of experiments are presented in Figure 3.3. The gyroscope signals show the angular velocities of the 3D rotations. The accelerometers show the three components of the gravitational acceleration and the acceleration of the sensor. The components of the magnetic field vector and the disturbance as measured by the magnetometers are plotted in the lower graph.
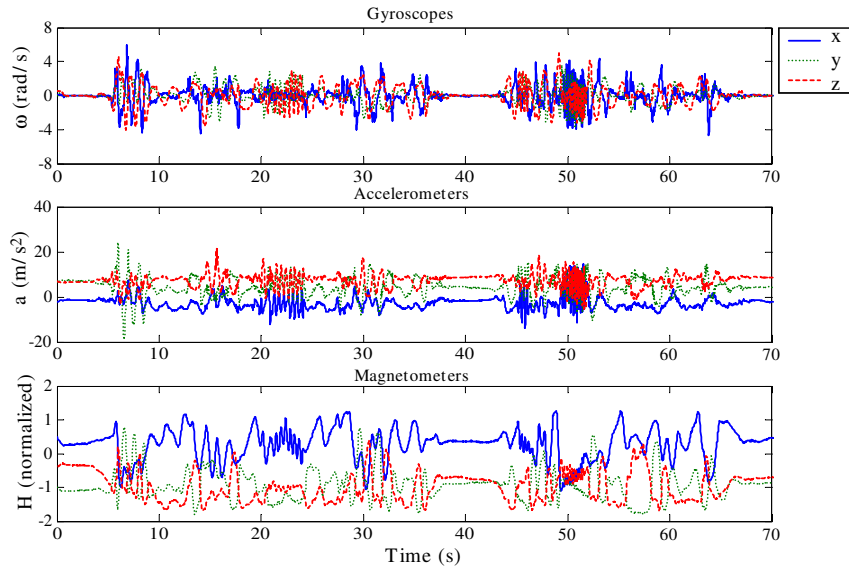
Figure 3.3 — Sensor signals of gyroscopes (upper), accelerometer (middle) and magnetometers (lowers) of combined 3D rotation near the ferromagnetic box.
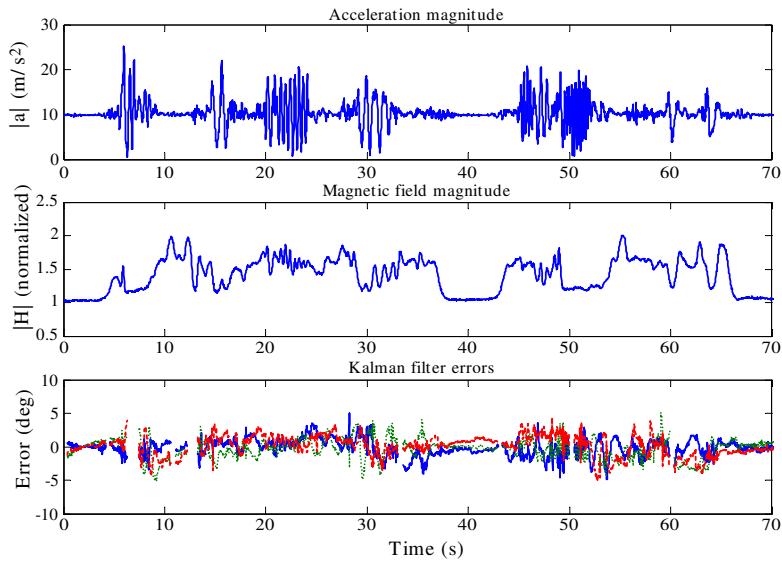
Figure 3.4 — Results from the sensor signals as plotted in Figure 3.3. Upper: acceleration norm. Middle: magnetic field magnitude. During the movements of the sensor, the magnetic norm is quite variable which is caused by the disturbed magnetic field. Lower: orientation difference between the filter with magnetic disturbance compensation and the optical reference system. The gaps in the data are caused by missed markers from the optical reference system, so no reference orientation could be calculated.

In Figure 3.4, the norms of the accelerometer and magnetometer signals are given in the upper and middle graph, respectively. The effect of the magnetic disturbance is clearly noticeable in variability of the magnetic norm. The difference in orientation estimated with the inertial and magnetic sensor module compared to the optical reference system is given in the lower graph. The error was expressed by the three components of the difference vector between both orientation estimates and was 2.7° root mean square (rms). When no magnetic disturbance compensation was applied the error was 11.9° rms.

Disturbances of the heading estimates due the metal case for a trial of the simulated assembly line experiment are shown in the upper graph of Figure 3.5. In the first five seconds, the sensor module is in a non-disturbed area and the magnetic norm equals one. During the movements near the metal case, the norm is quite variable. After 50 seconds the arm is retreated from the disturbed area and the norm equals one again.
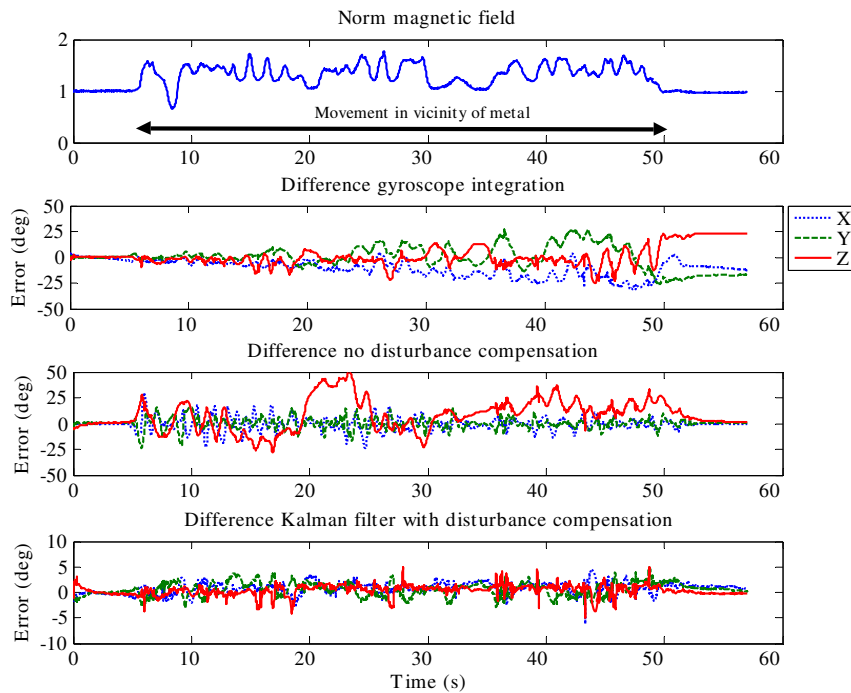
Figure 3.5 — Orientation estimation from the inertial and magnetic sensor measurements compared to the optical reference system in a simulated work task. Upper: normalized magnetic flux density. During the movements of the arm, the magnetic norm is quite variable which is caused by the disturbed magnetic field. Second: orientation angle difference in three axes when only gyroscopes are used. Third: Kalman-based filter orientation estimation with equal weight to accelerometer and magnetometer without disturbance model. Lower: Kalman-based filter with magnetic disturbance model.

The subsequent graphs show the differences of the orientations obtained with the inertial and magnetic sensor module with respect to the optical reference system. In the second graph, it can be seen that the drift error becomes significant after only a few seconds when only gyroscopes are used. The third graph presents the output of the Kalman-based filter with an equal weight factor of the accelerometers and magnetometers without magnetic disturbance compensation. When the arm enters the disturbed area, the orientation error around the Z-axis becomes quite large. After moving the arm away from the metal case the error converges back to zero. The disturbance is also noticeable in the other axes, since the magnetic field also influences the inclination component (dip angle). The lower graph illustrates that the orientation estimates using the full Kalman-based filter with magnetic disturbance model is not disturbed and drift free. The difference in orientation between the filter and the optical reference system of the complete trial is 3.4° rms.

In total, 10 trials with arm ab/adduction and flexion/extension were recorded without magnetic disturbance, two for each of the five subjects. From the same set of movements, 9 trials were successfully captured in the vicinity of the metal case. The rms error when no metal was near the sensors was 2.6° (std. dev. 0.5). With the metal case and no compensation applied, the rms error was 13.1° (std. dev. 3.0). In the simulated assembly line experiments, the error was 19.8° (std. dev. 3.6) with no compensation. Using the magnetic disturbance model and the described filter this rms error reduced significantly (paired t-test, p<0.01) to 3.6° (std. dev. 0.6).

3.3.1   Accuracy of the reference system

The accuracy of the reference system was considered by looking at the distances mx-y and mx-z between the markers x-y and x-z (Figure 3.1). Small variations in those distances were observed during the experiments (Figure 3.6).
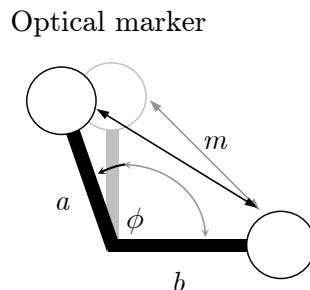
Optical marker

Figure 3.6 — Varying distances between markers cause errors in the orientation estimates of the optical reference frame.

Assuming fixed distances a and b between the markers and origin of the marker frame and the distance m delivered by the optical reference system (see Figure 3.7), the angle ϕ is calculated using the cosine rule:

$$\cos \phi = \frac{a^2 + b^2 - m^2}{2ab} \tag{3.2}$$

With an initial orthogonal marker frame, the error ϕ_ε becomes:

$$\phi_\varepsilon = 90° - \phi \tag{3.3}$$

The total error ϕ_ε was calculated by taking the norm of the error angles between markers x-y and x-z. The rms error related to the reference system was 0.9° (std. dev. 0.3).
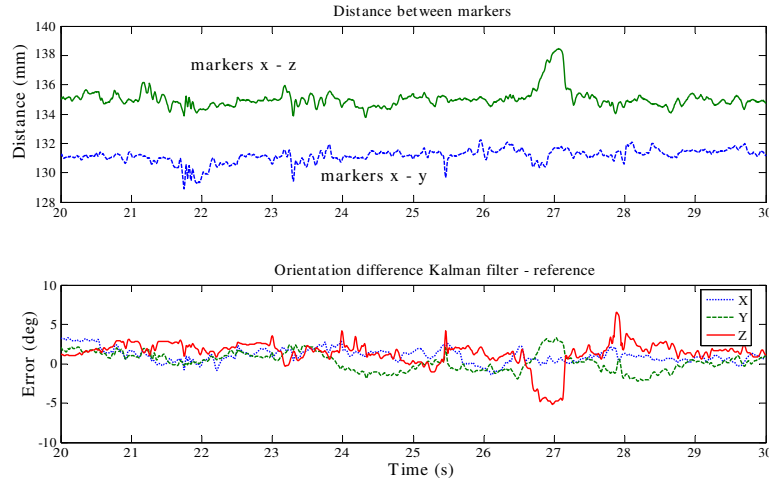
Figure 3.7 — Upper graph: distances in mm's between x and y markers and x and z markers. Lower graph: detail of orientation angle difference between Vicon system and the Kalman algorithm. Note the correlation between the error in the reference system and the difference between Vicon and Kalman filter.

3.4   Discussion

In this study, the accuracy and stability of orientation estimation fusing inertial and magnetic sensors with a Kalman-based filter was compared with a laboratory bound 3D optical tracking system. The rms difference between the two systems is 2.6° when no metal is in the measurement volume. When a sensor module attached to a body segment moved near a large ferromagnetic object, instant errors up to 50 degrees were measured when no compensation for disturbances was

applied. Using the magnetic disturbance model, the accuracy of the orientation estimate near metal increased significantly to 3.6° rms with no drift. The errors are dependent on the distance to the metal case and the complexity of the movements. Disturbances encountered in this set-up could be representative for assembly line work. However, performances may decrease in workplaces with moving parts since the properties of these disturbances are not modeled in the filter.

Some of the differences could explicitly be characterized as errors in the camera based system due to variations in the distances between markers. These variations can be caused by camera noise, limited sight of markers or vibrations of the marker frame [26]. The major part of the differences between the two systems is caused by modeling errors in the Kalman-based filter. Sources of errors are the estimates of the acceleration of the segment and magnetic disturbance vector. This latter vector is calculated based on the magnetic field vector estimates of the gyroscopes and magnetometers. When the magnetometers detect a disturbance from a changing dip angle and/or a changing magnitude, the orientation estimation will rely more on the gyroscopes and accelerometers. Because during the change, the information from the magnetometer is not taken into account, drift around the vertical axis can occur. However, with a constant magnetic disturbance, for example no movement near a metal case, no additional errors will be introduced. Finally, noise, non-linearity and limited resolution of the sensors are a source of errors.

The proposed method can be used for analyzing multiple body segments by putting a sensor module on each connecting part. The orientation and magnetic disturbance will be estimated by the filter for each segment. Anatomical constraints can be used to link the different segments and enhance the orientation estimation [76, 63, 9]. It should be investigated whether magnetic disturbance information from one sensor module can be used to predict the disturbance near a sensor module on a different segment. When markers or inertial sensor modules are attached to a body segment they should be calibrated to this body segment to obtain the orientation of this body segment. It should be noted that the problem of relating sensor to body segment has not been addressed in this study. Despite the choice of bony landmarks for placement, the skin under the sensor modules or markers will move with respect to the bones and will cause errors [98, 89]. Several compensation algorithms and solutions like cluster markers have been proposed to estimate the actual joint position and orientation from the marker positions on the skin [62, 2]. These methods should be optimized for inertial sensor modules since the net effect of the movement artifacts of a cluster of optical markers on the skin will be different from one sensor module.

In conclusion, the accuracy of orientation measurements fusing inertial and magnetic sensors substantially improves with the use of a magnetic disturbance model and enables ambulatory measurements at places were ferromagnetic materials are present.

Chapter 3. Evaluation of orientation measurements

Chapter 4

Improved motion tracking by fusion of optical and inertial measurements

D. Roetenberg and P.H. Veltink

submitted

4.1   Introduction

OPTICALLY based motion tracking systems like Vicon, Optotrak and Elite [90] are widely applied in clinical motion analysis [119, 56]. They offer accurate position tracking of body segments using either passive reflective or active transmitting markers captured by a number of cameras. Besides their high cost, one of the problems using these systems is the fact that the line of sight from camera to marker can be blocked, resulting in incomplete data [22]. A general approach to improve the continuity of the data is to position the cameras carefully and choose a marker set that would stay in view despite rotations or obstructions.

In recent years, many methods have been developed and are being utilized in commercial software to improve noisy and discontinued data [105, 78, 75, 24, 49]. The interpolation methods to fill gaps are often based on spline or polynomial functions connecting the last and first available samples before and after the gap. By looking at the kinematics of the body motion, the missed data can be predicted and performances improved. However, in pathological movement, which is often more variable, this method is less suitable. Despite these techniques, problems with missing markers blocked by for example walking aids, an assisting physiotherapist or the subject self, are still reported [101, 104, 108]. Gap-filling algorithms can only bridge a relatively short time without causing big errors. According to He and Tian [44], general filtering algorithms can reduce, but not eliminate the effect of outliers on the reconstructed trajectory.

Miniature inertial sensors have been proposed as an alternative to the camera-based systems [72]. They do not suffer from line-of-sight problems, latency or high costs related to the optical systems, however they are prone to errors due to integration drift [36]. Several methods and algorithms have been reported for accurate and drift free orientation measurements of human body segments combining the signals from 3D gyroscopes, accelerometers and magnetometers [30, 8, 65, 93]. Inertial position measurement is not possible without additional sources for long term applications due to integration drift of the accelerometers. Moreover, accelerometers can only measure position changes in time and no absolute positions.

In traditional navigation applications, several systems combining the position and orientation estimates from inertial sensors with an aiding source, such as GPS or radar, have been implemented successfully [16, 39]. In human motion tracking, combinations of inertial sensors with other motion tracking systems have also been reported. Emura and Tachi [27] combined a magnetic position and orientation tracking system with rate gyroscopes to improve the data rate and latency of the magnetic system. Foxlin [31] fused acoustic time of flight measurements with miniature accelerometers and gyroscopes for 6 DOF motion tracking. Azuma [7] used vision based features from head mounted devices together with inertial sensors for virtual and augmented reality purposes.

In this chapter [95], inertial sensors are combined with an optical tracking system. The first purpose is to fill gaps of optical data with position estimates of inertial data. The performances will be compared with a standard spline function. The second goal is to increase dynamic performances of the optical system. Relatively cheap inertial sensors can be sampled at high frequencies and can be placed at body parts with high velocities or accelerations. This offers the possibility to measure angular velocities and accelerations of body segments directly instead of differentiating the optical data. This could offer a valuable tool for studies in kinematics and new developments in induced acceleration analysis [55, 47].

4.2 Design of the fusing filter

4.2.1 Inertial tracking

Linear accelerometers measure the vector sum of acceleration $\mathbf{a}$ and gravitational acceleration $\mathbf{g}$ in sensor coordinates (S). To remove the component of acceleration due to gravity, the attitude of the accelerometer with respect to the vertical needs to be known. To measure the attitude, a gyroscope is required. This sensor measures angular velocity, and if integrated over time provides the change in angle with respect to an initially known angle. The combination of accelerometers and gyroscopes is also known as an inertial measurement unit (IMU) and comprises of three accelerometers in an orthogonal arrangement along with three gyroscopes. The sensor signals can be expressed in the global reference system (G):

$$^{G}\mathbf{a}_t - {^{G}\mathbf{g}} = {^{GS}\mathbf{\Theta}_t} \left({^{S}\mathbf{a}_t} - {^{S}\mathbf{g}} \right) \tag{4.1}$$

with $^{GS}\mathbf{\Theta}_t$ the rotation matrix describing the conversion from sensor to global frame at time t. After removing the gravity component, the acceleration $\mathbf{a}$ can be integrated once to velocity $\mathbf{v}$ and twice to position $\mathbf{p}$. These algorithms are generally known as an inertial navigation system (INS) [74], see Figure 4.1.

4.2.2 Fusion

To blend the available data from the inertial sensors and optical system efficiently, a complementary Kalman filter has been designed (see Figure 4.2). The complementary Kalman filter only operates on the system errors [16]. This mechanization has the advantage that it keeps the high dynamic responses necessary for human motion analysis. The observation delivered to the filter is the difference between the inertial position measurement $\mathbf{p}$ and the optical position measurement $\mathbf{q}$. The estimated errors from the Kalman filter are used to correct the inertial position and orientation estimates.
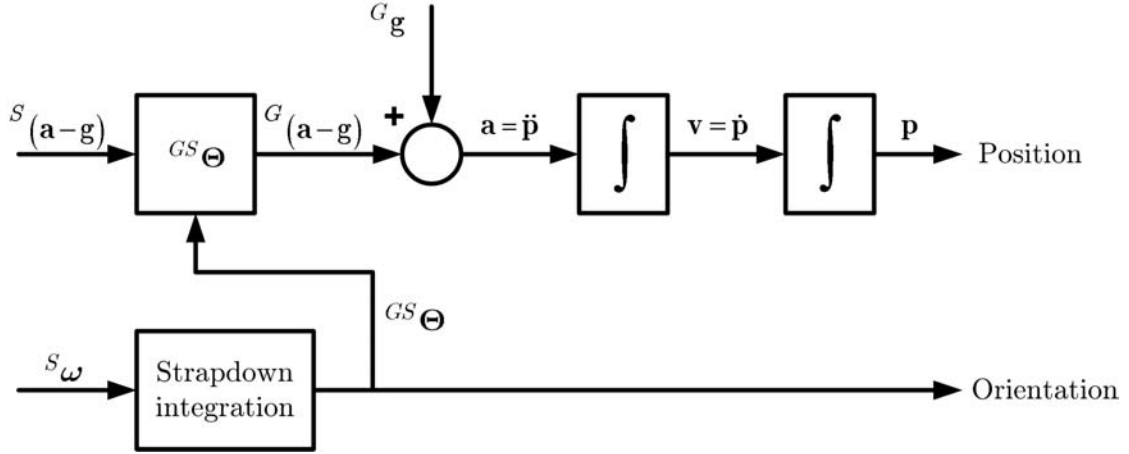
Figure 4.1 — Inertial navigation system (INS). The position and orientation in the global frame is computed using the sensor signals from the IMU. The upper input is the accelerometer signal $\mathbf{a} - \mathbf{g}$, the lower input is the angular velocity from the gyroscopes $\boldsymbol{\omega}$.

The discrete Kalman filter assumes the vector of states being estimated, $\mathbf{x}_t$, evolves according to a state propagation equation or dynamic model:

$$\mathbf{x}_{t+1} = \mathbf{A}\mathbf{x}_t + \boldsymbol{w}_t \tag{4.2}$$

where $\mathbf{A}$ is the state transition matrix from t to $t + 1$, and that measurements $\mathbf{z}_t$ are related to the states by a linear measurement model:

$$\mathbf{z}_t = \mathbf{C}\mathbf{x}_t + \boldsymbol{v}_t \tag{4.3}$$

where $\boldsymbol{w}_t$ and $\boldsymbol{v}_t$ represent process and measurement noise with covariance matrices $E\left[\boldsymbol{w}_t\boldsymbol{w}_t^\mathrm{T}\right] = \mathbf{Q}_t$ and $E\left[\boldsymbol{v}_t\boldsymbol{v}_t^\mathrm{T}\right] = \mathbf{R}_t$, respectively [35]. Note, that in a complementary filter structure the states $\mathbf{x}_t$ are error states, therefore, they can be read as $\mathbf{x}_{\varepsilon,t}$. Figure 4.3 gives a complete picture of the operation of the Kalman filter [114]. The outputs of the filter are used to correct the position, velocity, acceleration and orientation estimates $\hat{\mathbf{p}}^+$, $\hat{\mathbf{v}}^+$, $\hat{\mathbf{a}}^+$ and $\hat{\boldsymbol{\Theta}}^+$.

The most important factors contributing to the output error are incorporated in the error state vector:

$$\mathbf{x}_{\varepsilon,t} = \left[\mathbf{p}_{\varepsilon,t}, \mathbf{v}_{\varepsilon,t}, \boldsymbol{\Theta}_{\varepsilon,t}, \mathbf{a}_{\varepsilon,t}, \boldsymbol{\omega}_{\varepsilon,t}, \mathbf{q}_{\varepsilon,t}\right]^\mathrm{T} \tag{4.4}$$

with $\mathbf{p}_{\varepsilon,t}$, $\mathbf{v}_{\varepsilon,t}$ and $\boldsymbol{\Theta}_{\varepsilon,t}$ being the position error, velocity error and orientation error, respectively, $\mathbf{a}_{\varepsilon,t}$ is the accelerometer error and $\boldsymbol{\omega}_{\varepsilon,t}$ is the gyroscope error and $\mathbf{q}_{\varepsilon,t}$ is the position error from the optical system. All state vectors represent 3D vectors:

$$\mathbf{x}_\varepsilon = \left[\begin{array}{ccc} x_{\varepsilon,x} & x_{\varepsilon,y} & x_{\varepsilon,z} \end{array}\right] \tag{4.5}$$
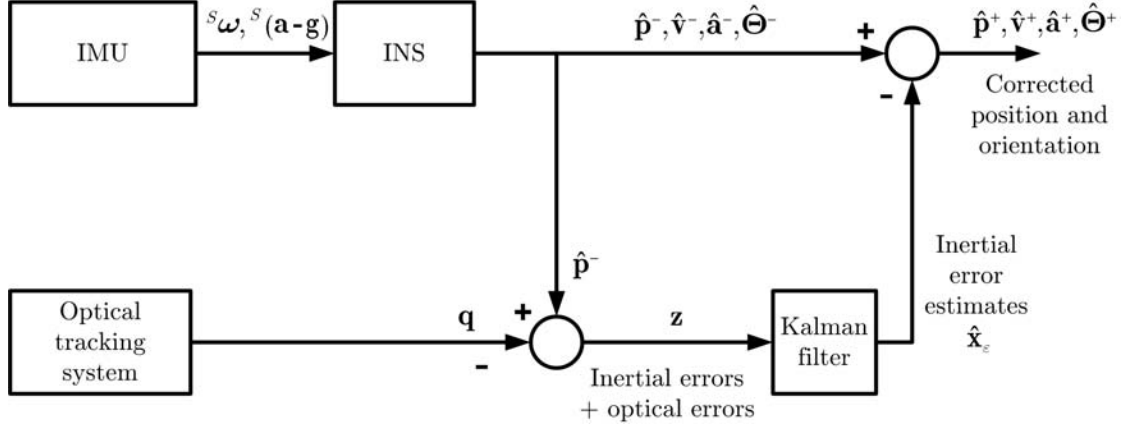
Figure 4.2 — Complementary Kalman filter structure for position and orientation estimates combining inertial and Vicon measurements. The signals from the IMU ($\mathbf{a} - \mathbf{g}$ and $\boldsymbol{\omega}$) provide the input for the INS (Figure 4.1). By double integration of the acceleration, the position $\hat{\mathbf{p}}^-$ is estimated at a high frequency. At a feasible lower frequency, the optical tracking system provides position $\mathbf{q}$. The difference between the inertial and optical estimates $\mathbf{z}$ is delivered to the Kalman filter. Based on the system model the Kalman filters estimates the propagation of the errors $\hat{\mathbf{x}}_\varepsilon$. The outputs of the filter are used to correct the position, velocity, acceleration and orientation estimates $\hat{\mathbf{p}}^+$, $\hat{\mathbf{v}}^+$, $\hat{\mathbf{a}}^+$ and $\hat{\boldsymbol{\Theta}}^+$.

4.2.3 Error model

The discrete inertial error model with timestep Δt, follows directly from the system description in Figure 4.1. The position error is calculated by the integration of the velocity error. The velocity error is the integration of the acceleration error. The velocity error is also depending on the orientation error multiplied by the measured acceleration signal as follows from Equation 4.1. The orientation error can be found by taking the first order approximation of a strapdown integration step:

$$\mathbf{p}_{\varepsilon,t+1} = \mathbf{p}_{\varepsilon,t} + \Delta t \mathbf{v}_{\varepsilon,t} \tag{4.6}$$

$$\mathbf{v}_{\varepsilon,t+1} = \mathbf{v}_{\varepsilon,t} + \Delta t \left({}^G(\mathbf{a}_t - \mathbf{g}) \times \boldsymbol{\Theta}_{\varepsilon,t} + \mathbf{a}_{\varepsilon,t} \right) \tag{4.7}$$

$$\boldsymbol{\Theta}_{\varepsilon,t+1} = \boldsymbol{\Theta}_{\varepsilon,t} + \Delta t \left[\boldsymbol{\omega}_{\varepsilon,t} \times \right] \tag{4.8}$$

where the matrix cross product operator is given by:

$$[\boldsymbol{\omega}\times] = \begin{bmatrix} 0 & -\omega_z & \omega_y \\ \omega_z & 0 & -\omega_x \\ -\omega_y & \omega_x & 0 \end{bmatrix} \tag{4.9}$$
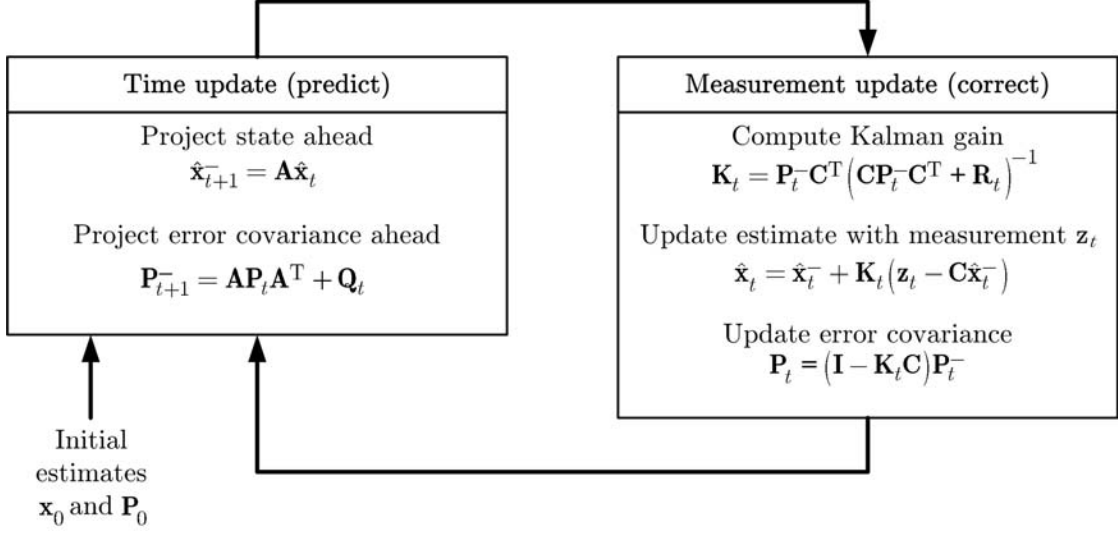
Figure 4.3 — Kalman filter loop. The *a priori* states $\hat{\mathbf{x}}^-$ and error covariance matrices $\mathbf{P}^-$ are predicted each time step t. When the measurement $\mathbf{z}$ comes available, the Kalman gain $\mathbf{K}$ is computed and the *a posteriori* estimates $\hat{\mathbf{x}}$ and $\mathbf{P}$ are computed after which the process can be repeated [114].

The acceleration and gyroscope errors $\mathbf{a}_{\varepsilon,t}$ and $\boldsymbol{\omega}_{\varepsilon,t}$ are modeled as first order Markov processes.

$$\mathbf{a}_{\varepsilon,t+1} = \mathbf{a}_{\varepsilon,t}e^{-\beta_a \Delta t} \tag{4.10}$$

$$\boldsymbol{\omega}_{\varepsilon,t+1} = \boldsymbol{\omega}_{\varepsilon,t}e^{-\beta_\omega \Delta t} \tag{4.11}$$

The autocorrelation of the Markov process is defined by [16]:

$$R_X(\tau) = \sigma^2 e^{-\beta|\tau|} \tag{4.12}$$

The optical position error $\mathbf{q}_{\varepsilon,t}$ is also modeled as a first order Markov process with additional white measurement noise:

$$\mathbf{q}_{\varepsilon,t+1} = \mathbf{q}_{\varepsilon,t}e^{-\beta_q \Delta t} + \boldsymbol{v}_{q,t} \tag{4.13}$$

In most optical systems, the correlation in errors between two consecutive samples from the optical system will be low and the error can be described just by the white noise term. The state transition matrix $\mathbf{A}_t$ is defined from equations 4.6 to 4.13:

$$\mathbf{A}_t = \begin{bmatrix} \mathbf{I}_3 & \Delta t \mathbf{I}_3 & \mathbf{0} & \mathbf{0} & \mathbf{0} & \mathbf{0} \\ \mathbf{0} & \mathbf{I_3} & \Delta t\,[(\mathbf{a}-\mathbf{g})\times] & \Delta t \mathbf{I}_3 & \mathbf{0} & \mathbf{0} \\ \mathbf{0} & \mathbf{0} & \mathbf{I}_3 & \mathbf{0} & [\Delta t\times] & \mathbf{0} \\ \mathbf{0} & \mathbf{0} & \mathbf{0} & e^{-\beta_a \Delta t}\mathbf{I_3} & \mathbf{0} & \mathbf{0} \\ \mathbf{0} & \mathbf{0} & \mathbf{0} & \mathbf{0} & e^{-\beta_\omega \Delta t}\mathbf{I_3} & \mathbf{0} \\ \mathbf{0} & \mathbf{0} & \mathbf{0} & \mathbf{0} & \mathbf{0} & e^{-\beta_q \Delta t}\mathbf{I_3} \end{bmatrix} \tag{4.14}$$

where $\mathbf{I}_3$ is a three by three identity matrix and $\mathbf{0}$ a three by three matrix of zeros. In this system, it is assumed that the noise for each state variable is uncorrelated with the noise for each other state. Hence, all non-diagonal terms of the noise matrix $\mathbf{Q}_t$ matrix are zero and the diagonal terms are the variances of the random variables.

4.2.4 Measurement model

The measurement presented to the Kalman filter is the distance measured by the optical system $\mathbf{q}_t$ minus the inertial distance estimate $\mathbf{p}_t$ (see Figure 4.2). Therefore, the discrete measurement model is formed from the inertial position error $\mathbf{p}_{\varepsilon,t}$ and optical error $\mathbf{q}_{\varepsilon,t}$:

$$\mathbf{C}_t = \begin{bmatrix} \mathbf{I}_3 & \mathbf{0} & \mathbf{0} & \mathbf{0} & \mathbf{0} & \mathbf{I}_3 \end{bmatrix} \tag{4.15}$$

The $\mathbf{R}_t$ parameter is the variance associated with the white measurement noise $\boldsymbol{v}_t$ term in Equation 4.3. The noise of the sensors in one direction is assumed to be uncorrelated with the sensor noise in another direction. Therefore, the non-diagonal elements of the measurement covariance matrix $\mathbf{R}_t$ matrix are zero.

4.2.5 Smoothing

In an off-line analysis, which is often used in clinical applications, the whole measurement sequence from $\mathbf{z}_1$ to $\mathbf{z}_N$ is available for processing. This offers valuable information about the error state propagation and enables the use of a fixed-interval Kalman smoothing algorithm. The principle of the fixed-interval smoothing algorithm during an optical gap is illustrated in Figure 4.4 [46]. The figure shows that two separate inertial solutions computed in the forward and backward directions quickly increase over time. When the Kalman smoothing algorithm is applied to the data, the error is significantly reduced across the data gap interval.

The Rauch-Tung-Striebel (RTS) algorithm provides an efficient method for implementing the Kalman filter smoothing [35]. The first (forward) sweep uses the Kalman filter as described previously but saves the computed *a priori* estimates $\hat{\mathbf{x}}_t^-$ and *a posteriori* estimates $\hat{\mathbf{x}}_t$ and their associated matrices $\mathbf{P}_t^-$ and $\mathbf{P}_t$ at each step time t. The second pass runs backward in time in a sequence from the time t_N of the last measurement, computing the smoothed state estimate $\hat{\mathbf{x}}_{[s]t}$ from the intermediate results stored on the forward pass. The recursive equations for the backward sweep are:

$$\hat{\mathbf{x}}_{[s]t} = \hat{\mathbf{x}}_t + \mathbf{S}_t \left(\hat{\mathbf{x}}_{[s]t+1} - \hat{\mathbf{x}}_{t+1}^- \right) \tag{4.16}$$

where the smoothing gain $\mathbf{S}_t$ is given by:

$$\mathbf{S}_t = \mathbf{P}_t \mathbf{A}_t^{\mathrm{T}} \mathbf{P}_{t+1}^{-}{}^{-1} \tag{4.17}$$
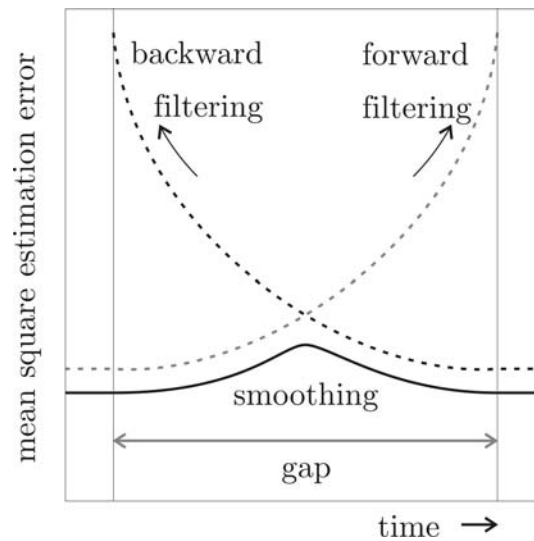
Figure 4.4 — Kalman filter smoothing during gap. The inertial errors increase rapidly over time when no reference data is available. By smoothing the forward and backward filtering, the mean square errors are significantly reduced.

4.3 Experimental methods

To test the algorithm, a Vicon 470 system (Oxford Metrix) consisting of 6 cameras and a MT9-B (Xsens Motion Technologies) inertial and magnetic sensor module were used. Calibration values of the 3D gyroscopes, accelerometers and magnetometers were provided by the manufacturer of the sensor modules. A temperature model in which the offsets of the sensors were related to the temperature of the sensor module was incorporated in the calibrated values. The signals of the sensors were sampled at 100 Hz with 16-bit resolution. The sample rate of the Vicon system was 120 Hz. The optical data was resampled in an off-line procedure to 100 Hz to match the sample rate of the inertial sensors. One optical marker with a diameter of 25 mm was attached to the sensor module to measure the sensor's position $\mathbf{q}$. Before testing, the alignment between the orientation of the sensors and the laboratory was determined in order to express the signals from both systems in the same frame.

4.3.1 Experiments

Two sets of experiments were performed. In the first set, the sensor with optical marker was placed on the mid foot of a subject. The subject walked across the lab several times at a comfortable pace. Ten trials were recorded varying from 30 seconds to 1 minute. In the second set of 10 trials, the sensor module was moved

freely through the lab by hand in a working volume of approximately 3 * 2.5 * 2 m. The movements consisted of combined translations and rotations at different speeds.

4.4   Results

The vertical positions of the optical marker and the Kalman estimates of a typical trial from the first set of experiments are given in Figure 4.5. The signals show a characteristic pattern of the vertical displacement of the marker on the foot while walking. The lower graph contains an enlargement of the upper graph. It can be seen that the position of the Kalman filter (dotted line) follows the Vicon position measurement. The filter removes some noise from the optical system but retains its dynamic characteristics.

Figure 4.6 shows the measured and estimated accelerations in the Z-direction of the same trial as in Figure 4.5. In the upper graph, the second order derivatives of Vicon position measurements are plotted without filtering any of the data. The noise, although small, in the position measurements is amplified by differentiating the data. When the position estimates are low pass filtered (middle graph, -3dB at 25 Hz, zero-phase 2nd order Butterworth), the accelerations look quite similar to the direct acceleration measurements from the accelerometers (lower graph). However, the accelerations measured by the accelerometers show less noise at a higher bandwidth. See, for example, the heel strike moments of the foot at t=14.8 and 16.1 seconds.

Figure 4.7 shows an example of a simulated gap in the optical data in a trial from the second set of experiments. The 3D measurements from the Vicon system were assigned as unavailable for two seconds (7 - 9 s) and the Kalman filter estimated the position changes based on the inertial sensor data. The dashed line in the upper graph is the connection between the last and first available optical frames by a 6th order spline function. Increasing the order of the function did not improve the curve fitting. The maximum error plotted is 12.1 cm in the Z-direction compared to the available original Vicon data. The maximum error when filling the gap using inertial data in the forward filter is 1.16 cm as illustrated in the lower graph. It can be seen that the error increases with the duration of the gap due to integration drift. By using the smoothing algorithm, the maximum error reduced to 0.38 cm, and the end position shows no drift error. The X and Y coordinates showed similar results.

The performances of gap filling when using inertial sensors and a spline function in the gait trials are illustrated in Figure 4.8. The optical data was assigned as unavailable for 5, 10, 25 and 50 frames (sample frequency = 100 Hz). The start of each gap was shifted through the gait cycle in steps of 10 %, where heel strike is
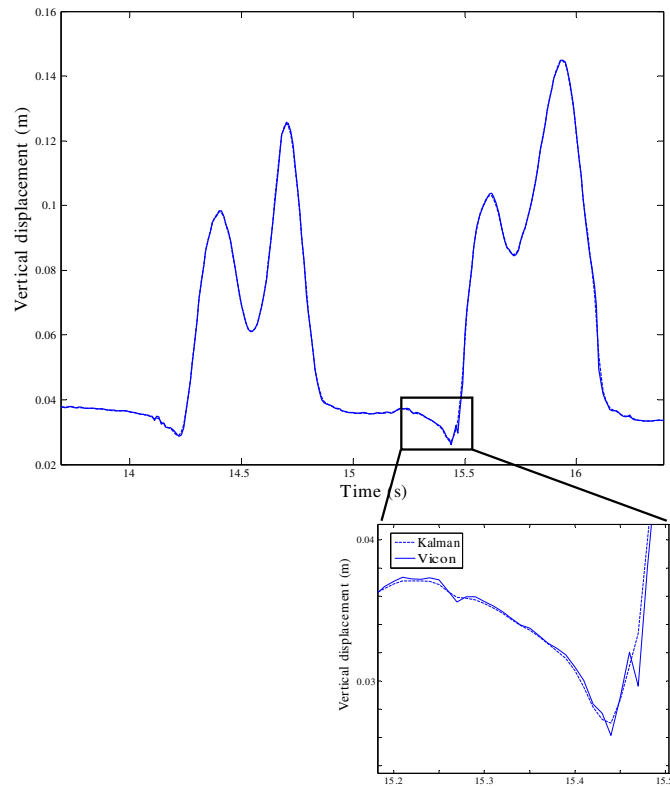
Figure 4.5 — Upper: vertical displacement of the Vicon marker on the mid foot of a typical gait trial consisting of two steps. Lower: zoom of Z-coordinate of Kalman filter (dotted) and Vicon position (solid).
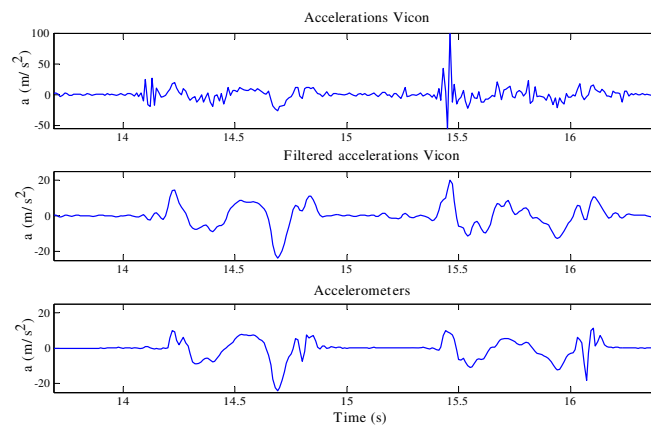

Figure 4.6 — Upper: Z-component of accelerations by double differentiation of optical position data. Middle: Twice differentiated filtered optical data. Lower: Measured acceleration with accelerometers after removing gravitational acceleration.
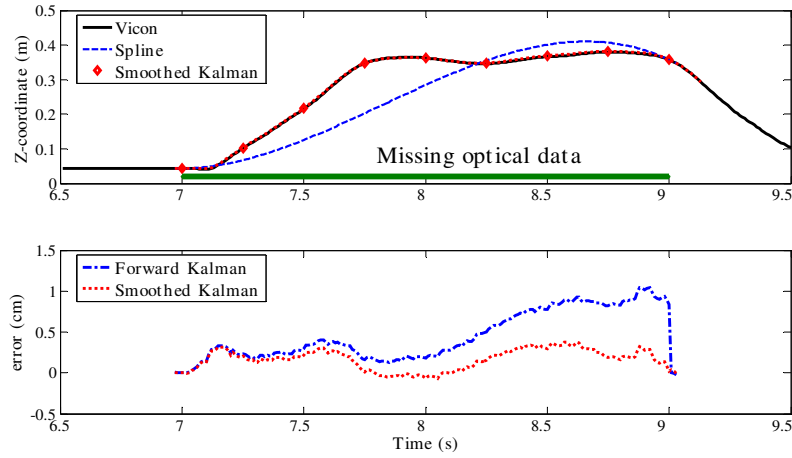
Figure 4.7 — Upper: 2 seconds of gap filling with a spline function and Kalman filtering in the global Z-coordinate. Lower: error of gap using the forward filter and smoothed implementation compared to the original Vicon data.

defined as 0 % and 100 %. In total, 10 steps were evaluated and compared with the original available optical data. The averages of the maximum errors during the gap are plotted for each time step. At short gaps (5 or 10 missing frames), the errors of inertial and spline fills are comparable (a few mm). With longer gaps, both methods show low errors during the stance phase. However, when a gap occurs during a part of the swing phase, the errors of the spline function increase significantly. Note that for larger gap sizes errors in the second part of the stance phase include errors related to the swing phase.

To test the performances of the filter at lower sample rates of the optical system, the frequency of available optical measurements presented to the Kalman was reduced. The update ratio is defined as the number of inertial measurements per number of updates of the optical system, with the inertial sample rate being 100 Hz. Accordingly, an update ratio of 2 means a simulated optical sample frequency of 50 Hz. In Figure 4.9, the errors of the Kalman filter are plotted as a function of the update ratio of the optical system for both the forward as well as the smoothed filter implementation. The averages and standard deviations are taken from all rms values of the second experiments. When the update ratio is 1, the difference between the position estimates of Vicon and the Kalman filter is below 0.1 mm. With an update once per second (ratio=100), the rms error of the forward filter is around 1.5 cm, though some higher maximum errors were observed, as can be concluded from the plotted standard deviations. When subsequently applying the backward filtering, the rms error is considerably reduced; the rms error is approximately 0.25 cm at an update ratio of 100.
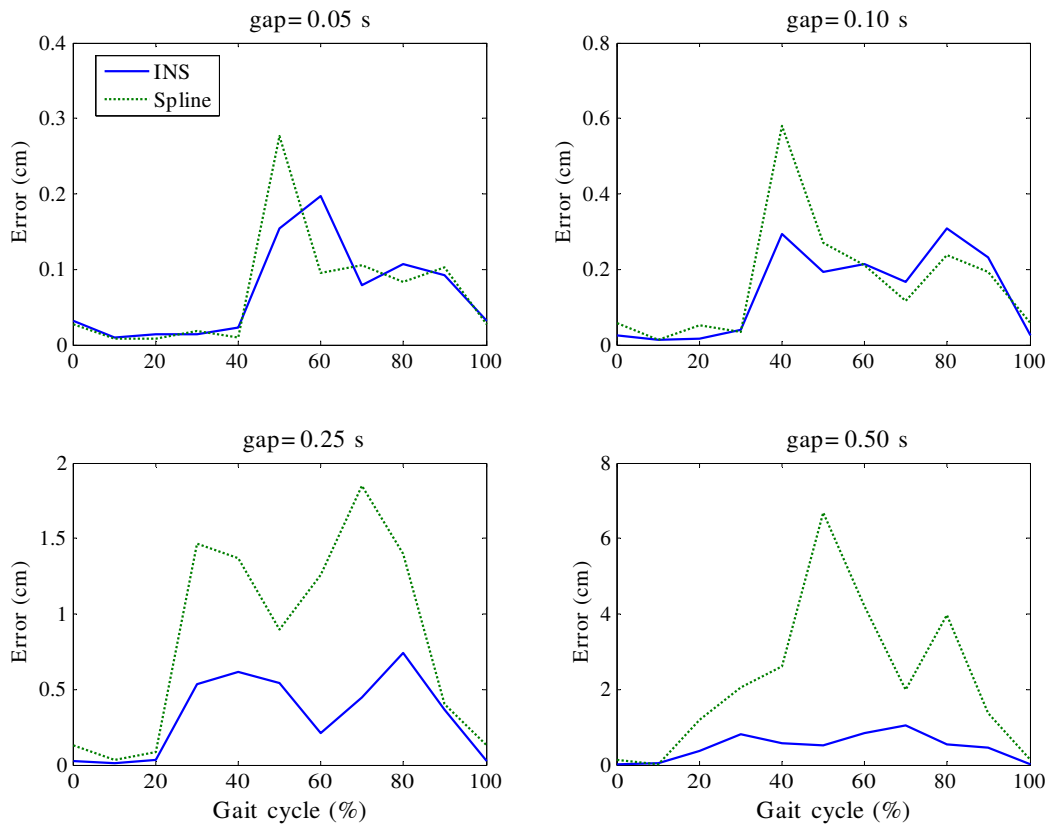
Figure 4.8 — Average maximum errors of gap filling with inertial sensors (solid) and spline function (dotted) related to the start of the gap in the gait cycle. The sensor was placed on the foot during walking. Ten steps were evaluated using the backward filtering and compared with the original available optical data. The gait cycle starts and ends at heel strike. Upper left: gap size is 0.05 seconds (5 frames), upper right: gap size is 0.10 s, lower left: gap size is 0.25 s, and lower right: gap size is 0.50 s.

The relation between the update ratio and rms error presented in Figure 4.9 is quite similar to the relation between the duration of a gap and the errors that occur when these gaps are filled with inertial estimates. An update ratio of 50 would correspond to a gap of 0.5 seconds. However, most optical systems have much higher sample rates, therefore more measurements are available before and after the gap which will improve the state estimates and reduce the errors.

4.5   Discussion

This chapter proposes a method for combining a camera-marker based motion analysis system with inertial sensors. The results show that the complementary
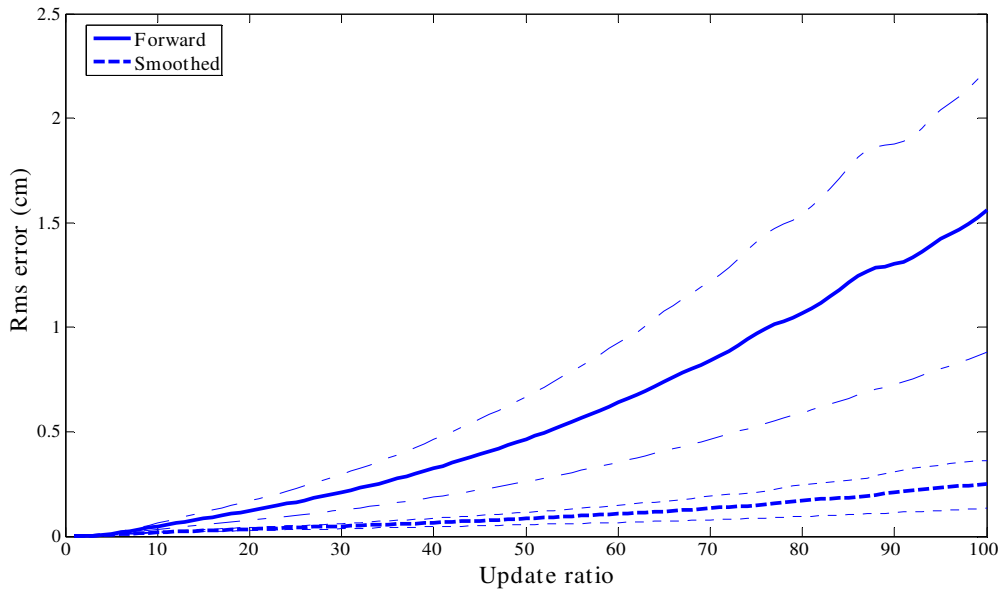
Figure 4.9 — Averages with standard deviations of all rms errors (n=10) of Kalman filter position estimates with update of Vicon system every x-th sample. The solid line represents the forward filter plus and minus the standard deviation (dash-dotted line). The dashed line is the smoothed error with standard deviation (dotted line).

Kalman filter can be used to fill gaps of optical data and increase the data rate of the optical system. The method also offers possibilities for identification and elimination of ghost markers. The 3D position and orientation estimates can be converted into axis of functional motion for biomechanical analyses. If the data is analyzed in an off-line procedure, the filter can also be executed reverse in time using a smoothing algorithm. Combining the forward and reverse position estimates significantly increases the performances. The smoothing algorithm described in this paper is obtained using the RTS fixed-interval smoothing. The algorithm can also be implemented as a fixed-lag smoother [35] for near real-time applications. When short gaps are present in the optical data, a spline function connecting the samples around a gap can be preferred since it is easier to implement. However, at longer gaps and during movement, the inertial fillings show significantly better results.

The sample rate of the used optical system was high compared to the sample rate of the inertial sensors. This offered the possibility to investigate the fusion algorithm at lower update rates by resampling the optical data and compare it with the original higher optical rate. With an update frequency of Vicon up to ten times lower than the sample frequency of the accelerometers, the maximum errors did not exceed 1 mm. This is well within the accuracy of the Vicon system running at full sample rate, as reported by Ehara [26].

The system as described in this study is not fully observable when applying only a single marker on the sensor. When the sensor is not moved, the rotation error around the global vertical (Z) axis cannot be measured. One optical marker does not give orientation information, therefore the orientation estimates can drift around this vertical axis. However, the position estimates are fully observable and when the sensor is moved, the measurements provide sufficient information to estimate the correct orientation using the system equations. Adding magnetometers or two more orthogonally placed optical markers can provide full observability. Magnetometers have the disadvantage of being sensitive to ferromagnetic materials. Adding more markers will increase the time necessary for the labeling procedure and may not be possible at some body segments without losing freedom of movement.

In order to estimate the orientation to remove the gravitational acceleration component, it is also possible to use an algorithm by fusing gyroscope, accelerometer and magnetometer signals as described in the previous chapters and [30, 8]. However, when testing this option with three optical markers as a reference, errors were significantly higher. The position error is highly correlated with the orientation error from the orientation sensor fusion algorithm. An error in inclination estimate of 1 degree results in an acceleration error of 0.17 ms^{-2} at 1 **g** as can be derived from Equation 4.1. This is explained in more detail in Appendix 4.A of this chapter.

The Kalman filter depends on a set of measurements and a proper dynamics model to provide optimal estimation of the states. Besides the quality of the measurements, the final quality of the states relies on the quality of the dynamic model [21]. If the measurements do not fit the model properly, it will result in non-optimal estimates. It is difficult to set accurate stochastic models for the used miniature gyroscopes and accelerometers that work efficiently in all cases and reflects the long-term behavior of these sensors' errors [45]. In Appendix 4.B, the innovations of the Kalman filter are presented. The analysis of the innovations shows that the used models are appropriate for this system.

It is unlikely that the optical data is unavailable for a long period in an experiment with well placed cameras. Moreover, the new generations of micro machined (MEMS) inertial sensors will be more accurate, have lower noise levels and suffer less from offset fluctuations [103], therefore the results can improve significantly.

In this study, the optical markers were attached directly to the sensor module. It is likely that the sensor modules will move with respect to the bones due to skin movements. The sensor module should be strapped tightly onto the body segment. The effect of vibrations and the calibration of a sensor module with an optical marker to the body segment should be investigated into more detail. The coordinates of a marker were assumed to be equal to those of the inertial sensors within the sensor module. Although they are very close in practice, it may explain

some errors in the comparison of both systems, especially during rotations.

In gait analysis, the highest marker speed is about 5 ms^{-1} [116]. This means the maximal position change of a particular marker between two successive frames taken by the same camera operating at 50 Hz equals 5/50=10 cm. By a sudden change in this movement, for example during stumbling, large errors in the frame capturing this moment can be expected. Also in sports analysis, high marker velocities with relatively large bandwidths are likely to be measured. The methods presented in this paper can potentially reduce costs of optical motion capture systems by reducing frame rate requirements but at the same time retaining high dynamic update rates and even improve dynamic performances.

Appendix 4.A: Different approach for orientation and position estimation

In order to use accelerometers for position estimates, the orientation of the sensor is required at each moment in time to express the acceleration in the global frame and remove the component of gravitational acceleration. In Chapter 2, we have developed a method to estimate orientation by fusing the signals from gyroscopes, accelerometers and magnetometers. Although Chapter 3 showed that this method is accurate, it appeared not to be the optical choice in combination with the position estimation filter described in the current chapter. The orientation measurements are related to accelerations of the sensor. A Kalman filter assumes uncorrelated measurements and since this is not the case when using the method described in Chapter 2, valuable measurement information cannot be recovered by the position models used in this chapter. To illustrate this relation, one trial was processed with the orientation estimates of Chapter 2 and these were used in Equation 4.1. The orientation propagation error (Equation 4.8 and the related covariance matrix $\mathbf{Q}$) was modeled as white noise with zero mean.

To measure the orientation of the sensor during movement, three additional optical markers were attached in an orthogonal arrangement (see Figure 3.1). The update ratio of the Vicon system was set at 50, which indicate a gap of 0.5 seconds shifting through the data. The sensor module was moved by hand through the lab in a cyclic movement with an amplitude of 0.5 m and a frequency of approximately 0.3 Hz. The upper graphs of Figure 4.10 show the norm of the accelerations obtained after estimating the orientation using only the gyroscope signals as presented in this chapter (left), and after using the fusion filter of Chapter 2 (right). Although they look very similar, there are some differences, for example around t=14 s. These small differences will cause errors when integrating the accelerations to velocity and position. The differences in accelerations can be related to the errors in orientation estimates which are shown in the middle graphs. Both methods were compared to the orientation obtained with the three optical markers. In the first few seconds of the recording, the sensor is not moved and the gyroscope orientation error in the heading direction shows some drift (left graph). This can be explained by the fact that when using a single marker for position updates, rotations about the global Z-axis cannot be observed, as already described in Section 4.5. When moving, this rotation error has a stochastic character and can be identified and corrected. The orientation errors of the fusion filter (right graph) show a cyclic pattern caused by the accelerations of the movement. This cyclic pattern contains information which was not retrieved by the Kalman filter. The lower graphs show the corresponding errors in position estimates. The position errors using the fusion filter orientation are about two times larger than the
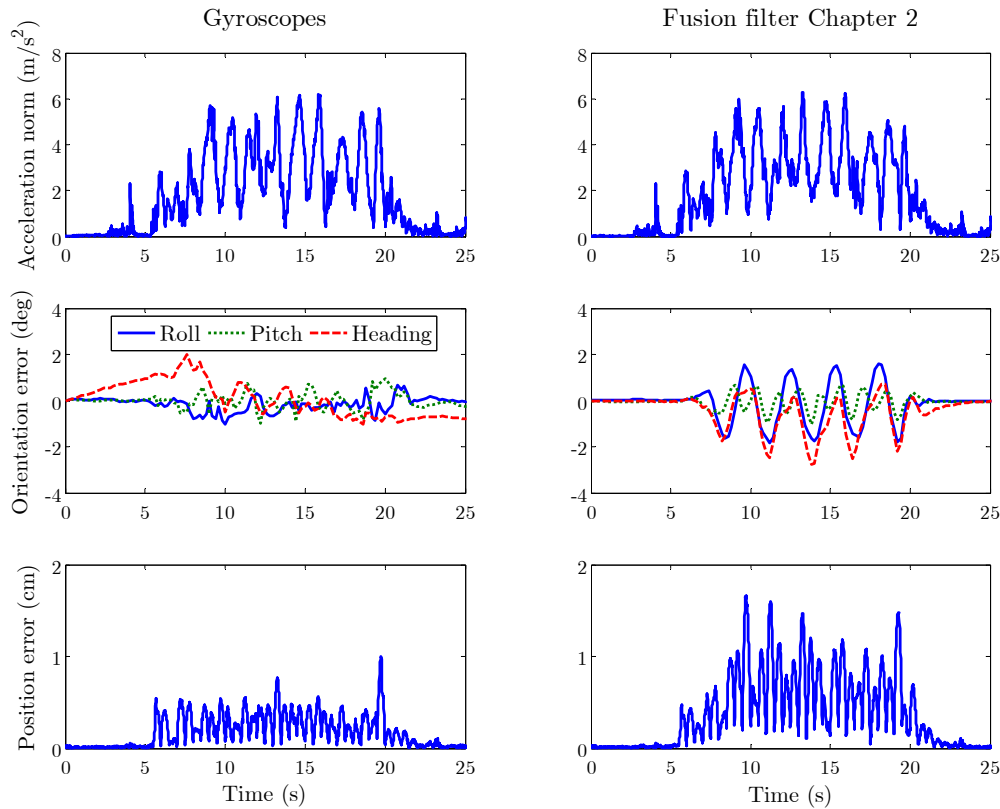
Figure 4.10 — Norm of acceleration, orientation errors and position errors when using only gyroscopes for orientation estimation (left) and the method of Chapter 2 (right). The sensor was moved by hand trough the lab in a cyclic movement with an amplitude of 0.5 m and a frequency of approximately 0.3 Hz.

position errors after estimating the orientation with only the gyroscopes.

Appendix 4.B: Innovations Kalman filter

In a properly tuned Kalman filter, one expects the innovation sequence to be white (uncorrelated, with zero mean). The innovation sequence is the time series of differences between the observations and the model predictions before updating:

$$\mathbf{y}_t = \mathbf{z}_t - \mathbf{C}_t \hat{\mathbf{x}}_t^- \tag{4.18}$$

A white innovation sequence can be taken as an indication that no further information can be extracted from the sequence of observations and the models and Kalman filter are appropriate for this system. Figure 4.11 shows a histogram of the innovations of a gait trial presented in Section 4.4 with a normal probability

density function. As can be seen in this figure, the innovations have zero mean and a normal distribution.

Figure 4.12 shows the spectrum of the same innovations which appears to be close to that of a white noise signal. From Figures 4.11 and 4.12, we can conclude that the used models in this chapter are appropriate for combining inertial sensors with the optical position system.
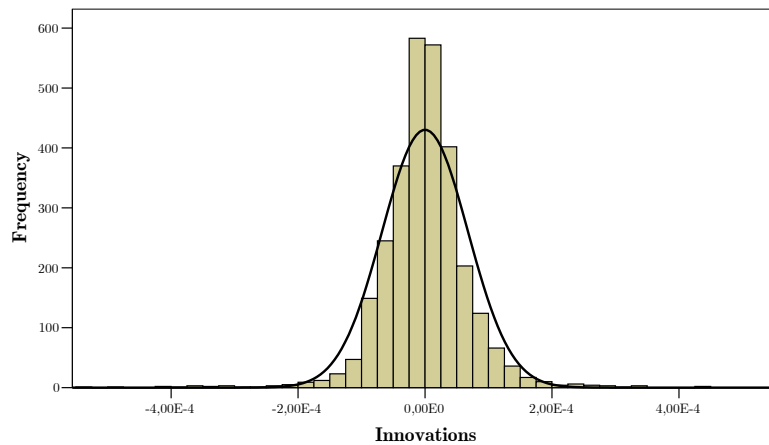
Figure 4.11 — Histogram of innovations of the Kalman filter, taken from 2983 samples. The line represents a normal (white) distribution.
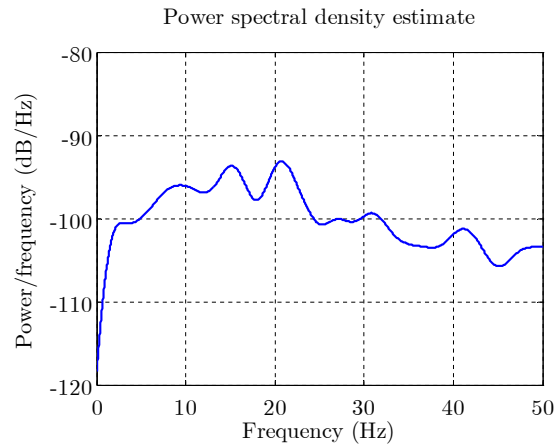
Figure 4.12 — The power is calculated shifting a Hanning window through the Fast Fourier Transformation (FFT) of the innovations.

Chapter 5

A portable magnetic position and orientation tracker

D. Roetenberg, P. Slycke, A. Ventevogel and P.H. Veltink

5.1   Introduction

IN MANY biomechanical and virtual reality applications, position measure-ments on the body are important. For motion analysis laboratories, many systems are available based on different physical principles; for example optical (e.g. Vicon; Oxford Metrics, Optotrak; Northern Digital), magnetic (e.g. Flock of Birds; Ascension, Star Track; Polhemus) or ultrasonic (e.g. IS300, InterSense). Under ambulatory conditions, possibilities for position measurements are limited. Miniature inertial sensors have been proposed for measurements outside the laboratory [72]. Positions and relative distances on the body can be estimated by using anatomic knowledge of segment lengths and joint characteristics in combination with inertial sensor based segment orientation estimates [8, 120, 67]. However, this approach is not satisfactory in cases with complex joints and non-rigid body segments like the back and shoulder. Distances between body segments can principally not be assessed by numerical integration of the measured accelerations due to the unknown starting position. Only short-term estimates of position changes within seconds can be estimated because of the inherent drift associated with double integration of accelerations [36].

To estimate on-body positions accurately, inertial measurements need to be combined with an aiding method. In traditional navigation applications, the fusion of inertial sensors with aiding sources such as GPS or Doppler radar is well established. In the previous chapter, a method for fusion of inertial sensors with an optical system is presented. Foxlin [31] fused acoustic time of flight measurements with miniature accelerometers and gyroscopes for 6 degrees of freedom (DOF) motion tracking. Emura and Tachi [27] combined a magnetic position and orientation tracking system with rate gyroscopes to improve the data rate and latency of a magnetic system. In all three studies, a fixed lab system was combined with inertial measurements. In this chapter, we will develop a portable magnetic tracking system, to be used as an aiding system. The magnetic-transducing technique overcomes occlusion problems associated with optical and acoustic tracking technologies [57].

Magnetic trackers use an electromagnetic field generated at some point in space and detected at a remote segment [58, 59]. Three essential components comprise these systems [88]:

- a 3D source, which generates a magnetic field;
- a compatible 3D sensor, which is fixed at a remote body segment and detects the fields generated by the source;
- a processor whose function is to relate the signals from source and sensor.

Given the signals from the source and sensor, the position and orientation of the sensor in 6 DOF with respect to the position of the transmitter can be estimated.

Commercially available magnetic trackers such as Fastrak (Polhemus) and

Flock of Birds (Ascension Technology) are provided with so-called long or extended range sources offering a tracking range of several meters [23]. However, the source, consisting of large (30-45 cm diameter) 3D coils, is fixed in one place and therefore limiting the measurement volume. For biomechanical analysis in ambulatory settings, we are interested in relative distances between body segments. These relative distances are generally smaller than the distances from a fixed source to a moving sensor in a lab environment. Consequently, the required magnetic fields to bridge distances on the body are smaller. Therefore, the source and power supply can be scaled down to be attached to the body, making the system portable.

   This paper focuses on the design of a portable magnetic system. Major requirements for such a system are small weight and size, and no impediment of functional mobility. It will be used as an aiding system for fusion with inertial measurements, therefore, the update rate requirements can be relatively low. The calculations to resolve the 6 DOF are based on a magnetic dipole approximation of the source [59, 88]. In the design of the coils, we try to imitate the ideal, infinitely-small dipole. Such imitation, however, is never perfect and causes inevitable errors, which dramatically increase at distances comparable with the coil dimensions [86]. In this paper, coil parameters, such as the radius are optimized for tracking the distance between the lower back and the shoulder of a person. With these results, the accuracy of the implemented magnetic distance and orientation estimates are evaluated by an optical reference system.
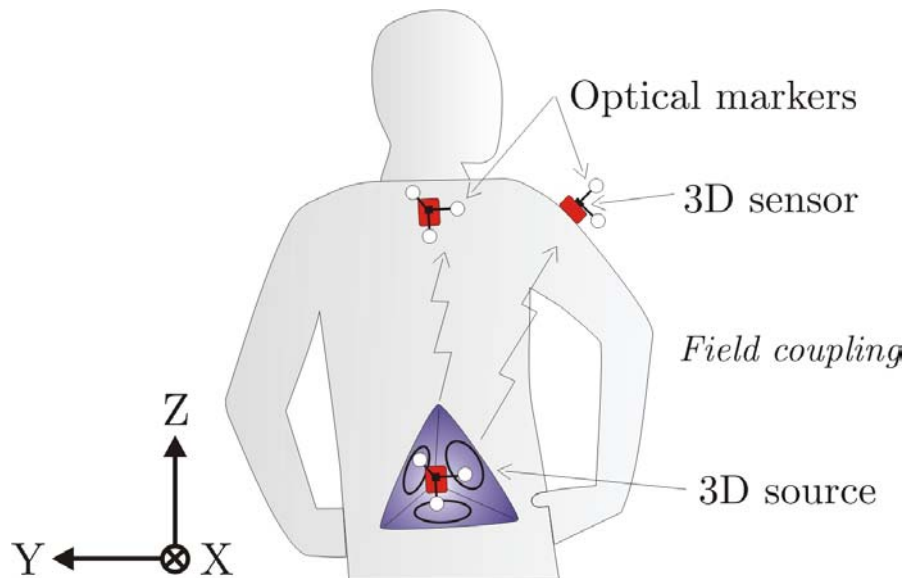

Figure 5.1 — Body-mounted magnetic system for measurement of relative distances and orientations on the body, consisting of a three-axis magnetic dipole-source worn by the subject and three-axis magnetic and inertial sensors on remote body segments.

5.2 Design of the system

Figure 5.1 shows a scheme of the implemented ambulatory magnetic system. The 3D source is constructed as a three orthogonally-sided pyramid (base diameter = 21 cm, height = 11 cm, weight 450 g). It is mounted on the back of the body and sensors are placed at remote body segments. The transmitter driver provides controlled pulsed DC current to three coils having orthogonal axes. The three-axis magnetic sensor measures the strengths of the magnetic pulses that are functions of the distance to the transmitter. The equations presented by Kuipers [60] are used to calculate the 6 DOF and are summarized in Appendix 5.A of this chapter. The three position parameters are expressed in spherical coordinates, where R is the distance between source and sensor and α and β are the tracking angles between the source and sensor frames. The orientation between source and sensor is expressed by rotation matrix $\mathbf{\Psi}$. Figure 5.2 shows the timing relationship of two identical cycles between the three orthogonal sources and sensors. During the period B_1 to B_2 the X-source is activated, from B_2 to B_3 the Y-source and from B_3 to B_1 the Z-source. Between the magnetic pulses, only the earth magnetic field is measured which can be subtracted from the measured pulses yielding the field $\mathbf{B}$ as emitted by the dipole source. At the end of the cycle, 9 values represent the relation between source and sensor; three sensor values for each time one of the coils is actuated. The entire cycle of pulsing the sources X, Y and Z repeats as long as measurements are required.

Because the source and sensors are placed on the body, the absolute position and orientation of the magnetic system are not known. To determine the orientation $\mathbf{\Phi}$ of the source with respect to the global reference system, an inertial and magnetic sensor was attached to the source. Accelerometers provide a means to estimate inclination [64]. The magnetometers give information about the heading direction, when not measuring the magnetic pulses. Changes in angles can be determined by integration of angular velocity, provided by gyroscopes. In between the magnetic actuation, the orientation of the sensor module was calculated using the Kalman filter fusion algorithm as presented in Chapter 2.

Assuming the maximum distance to be covered on the body, the noise levels of a typical magnetic sensor, and a sufficient signal-to-noise ratio (SNR), the minimal strength of the magnetic field can be calculated. The calculations and design of a coil to generate this field are presented in the next session.

5.2.1 Magnetic dipole

Figure 5.3 shows a circular loop of wire with radius b that carries current I. The magnetic potential $\mathbf{A}$ at a distance R_1 can be found by applying the Biot-Savart
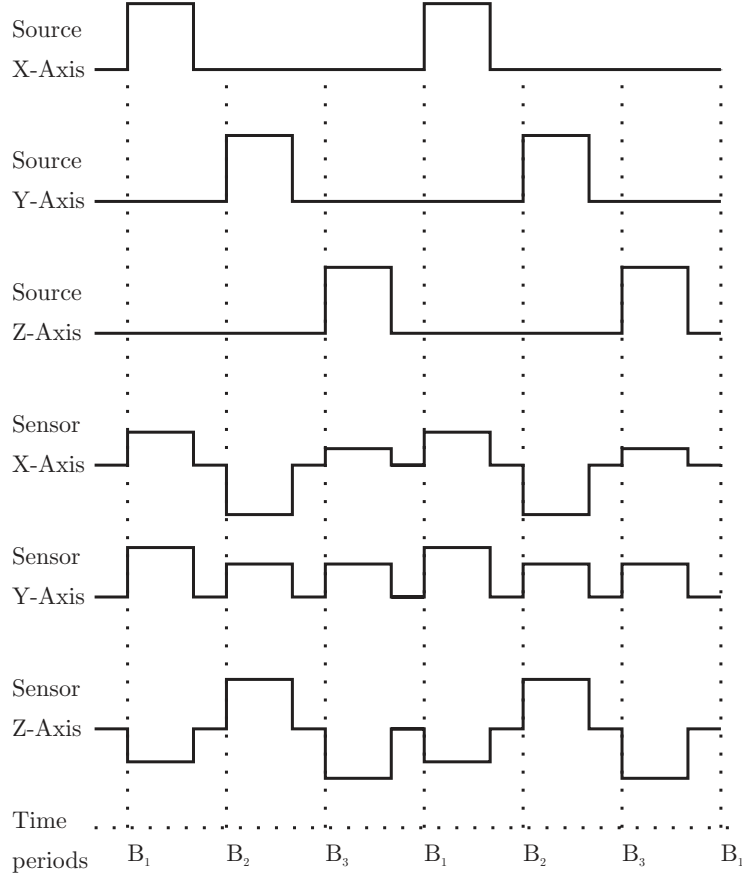
Figure 5.2 — Timing diagram showing the relationship between the transmitted and received signals.

law [20]:

$$\mathbf{A} = \mathbf{a}_\phi \frac{\mu_0 I b}{2\pi} \int\limits_{-\pi/2}^{\pi/2} \frac{b \sin \phi'}{R_1} d\phi' \tag{5.1}$$

with μ_0 being the magnetic permeability of vacuum ($4\pi \cdot 10^{-7}$ T $\cdot$ m^2/A). The magnetic flux density is $\mathbf{B} = \nabla \times \mathbf{A}$. To calculate the magnetic field when $R \gg b$, a coil can be considered as a magnetic dipole, with the magnetic induction $\mathbf{B}$ being expressed in spherical coordinates:

$$\mathbf{B}_{dipole} = \frac{\mu_0 M}{4\pi R^3} \left(\mathbf{a}_R 2 \cos \varphi + \mathbf{a}_\varphi \sin \varphi \right) \tag{5.2}$$

where M is the magnetic dipole:

$$M = N \cdot I \cdot \pi b^2 \tag{5.3}$$
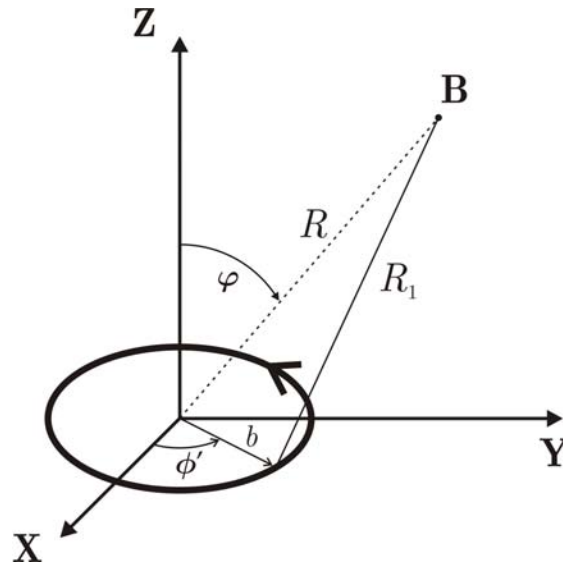
Figure 5.3 — A circular loop of wire, with radius b, carrying current I.

The axis of the coil is aligned with the line $\varphi = 0$, $\mathbf{a}_R$ and $\mathbf{a}_\varphi$ are radial and tangential unit vectors. N is the number of turns of wire in the coil. Figure 5.4 shows the relative error between the magnetic field as emitted by a coil and equivalent dipole, as a function of the relative distance R with respect to radius b. The error ε_{approx} is given by:

$$\varepsilon_{approx} = \frac{|\mathbf{B}_{coil} - \mathbf{B}_{dipole}|}{\mathbf{B}_{coil}} \times 100\% \qquad (5.4)$$
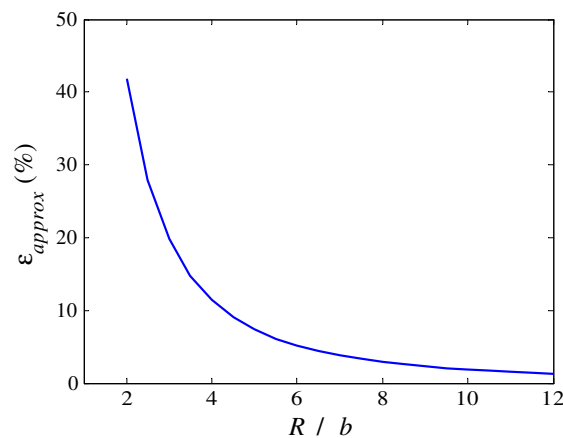
Figure 5.4 — Relative error ε_{approx} of a coil compared to a dipole as a function of distance from the coil along the Z-axis.

In the dipole approximation, three parameters need to be optimized: the coil radius b, the number of windings N and the current through the coil I. Although a coil with a large area has a higher magnetic moment M according to equation 5.3, the accuracy in dipole approximation will decrease. Increasing the number of windings also increases M, however, it will result in a higher self-inductance and resistance, which is undesirable, especially in case of battery power supply. A higher resistance requires a higher voltage to drive the same amount of current through the coil. An increased self-inductance results in a longer rise time of the applied pulse. Finally, the current through the coil is partly limited by the internal resistance of the battery and partly by its capacity, the additional weight, and maximum measurement time. From Figure 5.4, we find that the systematic dipole approximation error decreases as the distance from the coil increases, however at larger distances, stochastic errors will determine the accuracy of the 6 DOF measurement.

The required magnetic dipole strength M assuming a SNR n can be obtained using:

$$M = \frac{4\pi R_{max}^3 n \mathbf{B}_n}{\mu_0} \qquad (5.5)$$

The maximum distance R_{max} to be covered by the magnetic field was based on the distance between the source as placed on the lower back and the shoulder and was assumed not to exceed 70 cm. The noise level $\mathbf{B}_n$ of the used magnetoresistive sensor, with the necessary electronic flipping circuit [106] is about $0.5 \cdot 10^{-7}$ T [118]. With a SNR n of 4, the magnetic dipole becomes 0.69 A/m. The necessary accuracy in the dipole approximation was set at 5 % at a distance half of the specified distance between the lower back and shoulder (=35 cm). In Figure 5.4, we can find the corresponding coil radius b, which is 5.5 cm. The number of windings N and current I followed from the necessary field strength and were 50 and 1.5 A respectively.

5.3   Experimental methods

An electrical circuit was designed to drive the coils by means of four AA (LR6 - 2400 mAh) batteries. The pulse duration, duty cycle and driving current could be controlled by means of a Bluetooth interface. The magnetometers in a MTx (Xsens Motion Technologies) sensor module were used to measure the strength of the pulses and the earth magnetic field in 3D. The sample frequency of the sensors was 120 Hz with 16 bits resolution. A Vicon 470 system (Oxford Metrix) consisting of 6 cameras operating at 120 Hz was used as a reference. Three optical markers with a diameter of 25 mm were attached to the sensor module in an orthogonal arrangement to validate the sensor's position and orientation with respect to the

position of the coils as can be seen in Figure 5.1. One MTx sensor module was attached to the assembly of the three coils to measure its orientation with respect to the global reference system. Before testing, the alignment between the orientation of the sensors and the laboratory was determined in order to express the signals from both systems in the same frame.

In the first experiments, the bench-test, the set of coils was placed on a table. One sensor was moved by hand near the coils. Distances were varied slowly from approximately 10 cm to 80 cm and the sensor was rotated along all axes. In the following experiments, the three perpendicular coils were attached to the body as illustrated in Figure 5.1. One sensor was placed on the back of a subject, at the level of the first thoracic vertebra and one sensor was placed on the proximal part of the upper arm. The subject performed flexion - extension and abduction - adduction of the arm followed by standard anatomical movements of the back: flexion (and extension), lateral flexion and rotation. In the final tests, the sensor was placed on the upper leg, just above the knee. The subject walked across the laboratory at a comfortable pace for a number of steps. All experiments were repeated 10 times.

5.4   Experimental results

Figure 5.5 shows the magnetic pulses as measured by the magnetometers from a typical trial. The sequence of the three X, Y and Z pulses, as illustrated in 5.2, can be identified as well as their changes in magnitude as a result of the performed movement. The pulsewidth was 60 ms, the cycle time (B_1 to B_1) was 600 ms and the current 1.5 A.

The time instants of the pulses are exactly known and the rise time of a pulse is much faster than changes in the earth magnetic field vector caused by movement. Therefore, by evaluating the values of the earth magnetic field just before and after the pulse, the magnitudes of the pulses can be obtained. However, due to movement within one cycle of three pulses, errors can occur. An example can be seen in Figure 5.6; in the first burst of three pulses, the DC earth field component varies.

In Figure 5.6, an example of the distance estimates R from the center of the coils to the magnetic sensor is presented where the sensor is moved by hand. The root mean square (rms) accuracy of this trial is 7.9 mm compared to the optical distance measurement. When the sensor was moved beyond a distance of approximately 80 cm, the SNR of the magnetic signal was too low to be used for relevant measurements.

Figure 5.7 shows the X, Y and Z-coordinates of a trial in which the subject performed latero-flexion of the back twice. The spherical parameters (distance R,
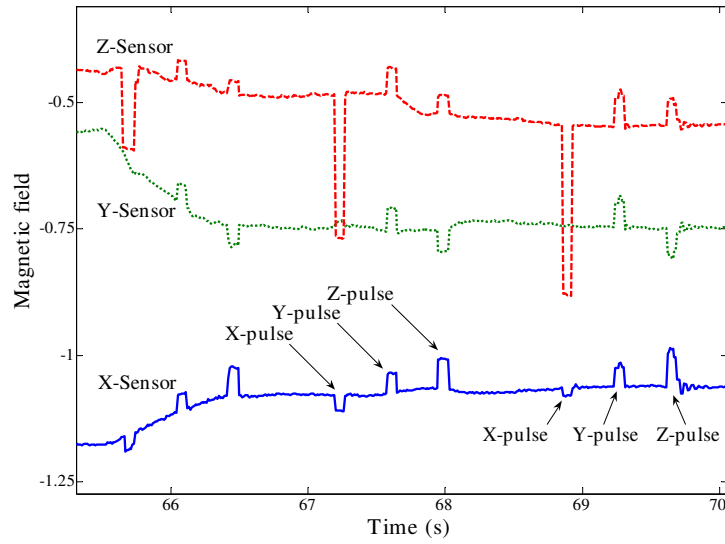
Figure 5.5 — Three cycles of magnetic pulses measured by the magnetometers. The pulsewidth was 60 ms and the cycle time 600 ms.
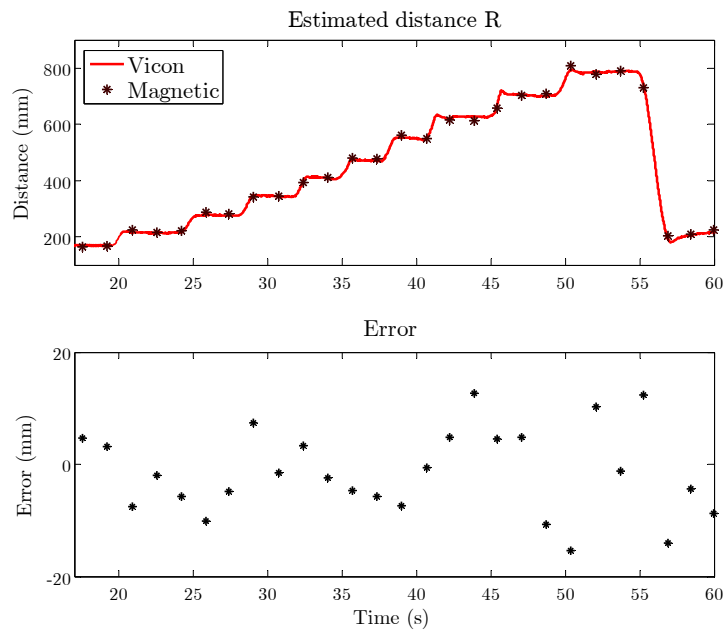
Figure 5.6 — Upper, magnetic and Vicon distance measurements of a typical bench-test recording. The sensor is moved by hand around the fixed source from approximately 15 cm to 80 cm. The magnetic estimates are indicated by *. Lower: error in magnetic distance estimation compared to the reference Vicon.
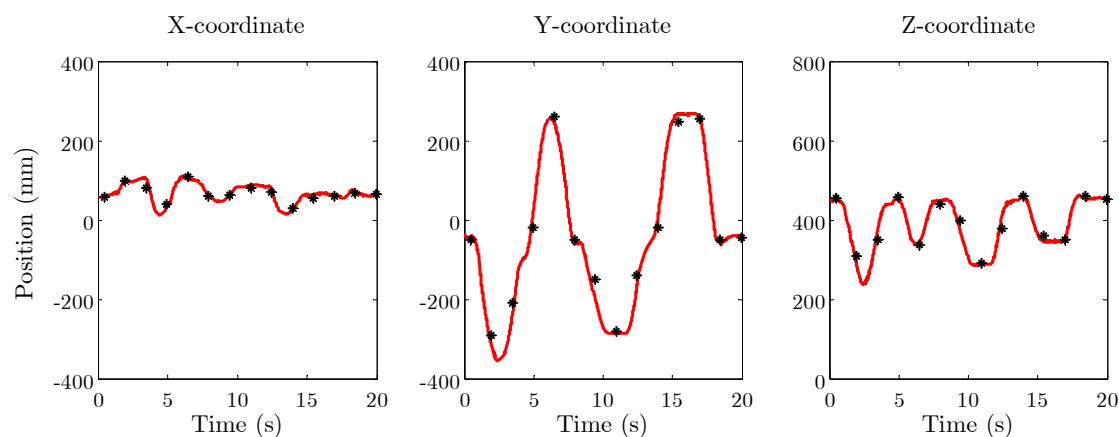
Figure 5.7 — X, Y and Z coordinates of the sensor placed on the back with respect to the center of the source. The subject performed latero-flexion of the back twice. The magnetic position estimates are indicated by *, the Vicon reference is the solid line.

and tracking angles α and β) were transformed in Cartesian coordinates. The center of the coils is the origin of the magnetic frame which is aligned with the global frame using the orientation Φ of the source. The stars (*) present the magnetic position measurements and the solid line, the reference coordinates. From the initial coordinates, we see the sensor is located on the back about 45 cm positioned above the source (Z-coordinate), 5 cm to right (Y-coordinate) and 6 cm forward (X-coordinate). First, the subject bends to the right and both the Y-coordinate and the Z-coordinate decrease. Then, the subject flexes through neutral position to the left. The Y-coordinate now increases while the Z-coordinate decreases. Since the sensor is placed on the right side of the spinal chord, the amplitude of the left flexion movement is less than the right. At the end of the two cycles, the subject is neutral position again. From the X-coordinate, we can see the sensor moved only a few cm forward and backward during the recording.

Table 5.1 shows the numerical results of all performed experiments. The orientation error is defined as the smallest angle about which the sensor frame has to be rotated to coincide with the reference frame. The position error is defined as the shortest distance between the magnetic coordinates and the reference coordinates. The differences between the position and orientation measurements of the optical and magnetic system were taken from 10 trials for each movement. The lowest errors were observed during the relatively slow movements of the arm and back. The walking trials showed higher errors because of the under sampling with respect to the performed movement. The errors of the sensor on the back were smaller than those of the sensors on the leg or arm because during walking, the relative position of the sensor on the back was stable with respect to the source.

The orientation of the sensor module was also estimated using the signals from the gyroscopes, accelerometers and magnetometers and the fusion algorithm described in Chapter 2. These estimates are independent of the distance between source and sensors, but they are correlated with accelerations and magnetic disturbances. The average orientation error using this method was 3.0° for all trials, comparable with the accuracy reported in Chapter 3.

Segment	Movement	Position error [mm]		Orientation error [deg]	
		RMS	SD	RMS	SD
Bench-test		7.6	2.4	5.9	2.6
Back	*Flexion*	5.9	1.5	4.9	2.3
	Latero-flexion	6.3	1.5	5.2	2.1
	Rotation	5.9	1.4	5.1	1.9
	Walking	8.6	1.6	6.8	2.7
Arm	*Flexion*	7.8	1.8	6.6	2.2
	Abduction	7.2	1.7	6.2	2.2
	Walking	11.7	2.9	7.4	3.1
Leg	*Walking*	15.0	4.6	8.7	3.3

Table 5.1 — RMS Position and orientation errors and their standard deviations (SD) of the magnetic tracker for each segment and movement. All movements were performed 10 times.

5.5 Discussion

In this chapter, a magnetic tracking device is presented that is ambulant and thus can fully be worn on the body without the need for an external reference. Although magnetic trackers are commercially available, they are limited to a restricted measurement volume and have large and heavy sources which do not allow for ambulatory purposes. We have designed a set of copper-winded coils, integrated in a synthetic dome, and the electronics for battery powered magnetic pulsing. The system will be used as an aiding system to update on-body position and orientation estimates from inertial sensors. The average position error was 7.6 mm with the bench tests where the sensor was moved by hand in 6 DOF. The reference system was assumed to have an accuracy of 1 mm [26]. With the sensors on the shoulder and back, the relative movement between sensor and source was limited and errors were smaller. The highest errors were observed when both source and sensor moved with relatively high velocities during walking. The performances do not yet meet requirements for many biomedical applications. A part of the errors

was related to the low pulsing and sampling frequency with respect to the performed movements. By combining the magnetic system with inertial sensors, we expect these errors to reduce. This combination will also improve the orientation estimates of the magnetic system. In the experiments, we have seen that the orientation errors of the inertial and magnetic sensor fusion algorithm from Chapter 2 are smaller than those of the magnetic system solely.

The accuracy of the magnetic system can be improved by a higher signal-to-noise ratio, which will reduce the stochastic errors. This can be achieved by increasing the strength of the magnetic dipole or reducing the noise of the sensors. The configuration of the coils was optimized for distances up to 70 cm. This means that this set-up is not suitable for full body tracking. Paperno and Plotkin [86] found a significant improvement of the magnetic dipole approximation error of a coil by optimizing the length L of a coil with respect to its diameter b to an optimum of $L/b = 0.86$. A dipole strength necessary for distances on the body require an optimal length that is not practical for body mounting. However, different coil configurations emitting stronger fields should be investigated. Also, a network of body attached coils can be used for full body tracking. Systematic errors can be reduced by using the analytical relation to calculate the field emitted by a coil instead of the dipole approximation. However, it will require more processing time.

The magnetometers in the sensor module are now 'flipped' every few samples to prevent offset drift [106]. Although regular flipping is necessary for stable magnetic measurements, it can introduce oscillations during pulsing due to large changes in the measured magnetic field. This can be seen in the last Z-pulse of Figure 5.5. These measurement artifacts will decrease by reducing the frequency of flipping and by avoiding flipping during pulsing. The latter can be implemented by synchronizing it with the timing of actuation.

Within one burst of three magnetic pulses, the relative position and orientation between source and sensor can change. In the related 6 DOF calculation, these were assumed to be constant. To reduce these errors, the time between a X, Y and Z-pulse should be decreased. Also, the pulse duration can be shortened which requires a higher sample frequency of the magnetometers. Moreover, changes in orientation and position of source and sensor during pulsing can be measured using inertial sensors.

The magnetic field magnitude decreases with the cube of distance. To measure a signal with a sufficient SNR, a strong field at the source is necessary and the sensors should be relatively close to the source. Continuous driving of all coils requires a substantial amount of energy. The tested update rate of this system was 1.7 Hz, which is low if this system is used for human motion tracking. However, this update rate is sufficient to serve as reference measurement for inertial tracking as we have seen in the previous chapter. Miniature inertial sensors are suitable for measuring fast changes in position and orientation and require less energy. Since

the magnetic dipole source is required to be active only during a small percentage of time, the average energy needed is limited. This principle requires an algorithm to fuse position and orientation estimates from the magnetic system with those of the inertial sensors. In the next chapter, this combination will be developed.

Like every magnetic tracking system, it is vulnerable for magnetic disturbances. The static magnetic field in the used measurement volume can be considered as homogeneous. The distance between source and sensors is relatively small, therefore less interference problems are expected compared to a range of several meters in a laboratory set-up. Moreover, by combining this system with inertial sensors, the effect of magnetic disturbances can be reduced. Errors related to magnetic disturbances will have different spatial and temporal properties than drift errors related to inertial sensors.

The system uses magnetic pulses because time-varying (AC) fields cause an induced electromotive force (emf) in accordance with Faraday's law when magnetic flux flows in nearby conducting and ferrous materials. The induced emf will produce local currents in the materials normal to the magnetic flux. These so-called eddy currents generate secondary magnetic field that will influence the magnetic distance measurement. When using pulses, eddy currents die out at an exponential rate after the pulse reaches its steady state value. Sampling the transmitted signals farther from the leading edge will result in a sensed signal containing less eddy current components. The relative sensitivity to ferromagnetic materials depends on the size and type of the metal [81, 61].

With the described settings and used batteries we were able to perform measurements for over 30 minutes. New generations of rechargeable batteries (or fuel cells) will have higher capacities which can extend the measurement time. Alternatively, the driving current I through the coils can be increased. In addition, shorter pulses and a longer cycle time when combined with inertial sensors will extent the operating time with a set of batteries.

Appendix 5.A: Theory 6 DOF magnetic tracking

All six DOF, i.e. the three translation parameters (R, α, β) and the three rotation parameters (ψ, ϕ, θ) are illustrated in Figure 5.8. They define how two independent bodies are situated relative to each other. The spherical coordinates (R, α, β) are related to the Cartesian coordinates X, Y and Z by:

$$R = \sqrt{X^2 + Y^2 + Z^2} \tag{5.6}$$

$$\alpha = \tan^{-1}\left(\frac{Y}{X}\right) \tag{5.7}$$

$$\beta = \cos^{-1}\left(\frac{Z}{R}\right) \tag{5.8}$$

where $R \in [0, \infty)$, $\alpha \in [0, 2\pi)$, and $\beta \in [0, \pi]$, and the inverse tangent must be suitably defined to take the correct quadrant of (X,Y) into account.

A three-axis electromagnetic dipole source represents the reference frame. This source generates a time-multiplexed sequence of electromagnetic fields which are detected by a three-axis magnetic sensor which represents the remote body frame. The algorithms to calculate the 6 DOF are presented by Kuipers [60] and are summarized in the following sections.

The sequence of unit source excitations is represented by the column vector of the matrix $\mathbf{E}_i$, expressed in the source frame:

$$\mathbf{E}_i = \begin{bmatrix} 1 & 0 & 0 \\ 0 & 1 & 0 \\ 0 & 0 & 1 \end{bmatrix} \tag{5.9}$$

The corresponding sensed signals is expressed in the sensor frame by the columns of the matrix $\mathbf{E}_o$ as can be seen in Figure 5.2.

Source-to-sensor coupling

Consider the Z-unit excitation applied to a source - a single dipole element, as illustrated in Figure 5.3. The field generated by the unit excitation vector $\mathbf{B}$ is detected by a remote sensor whose location (R, α, β), is yet unknown. The tracking transformation matrix $\mathbf{\Upsilon}$ defines the direction to the sensor with respect to the
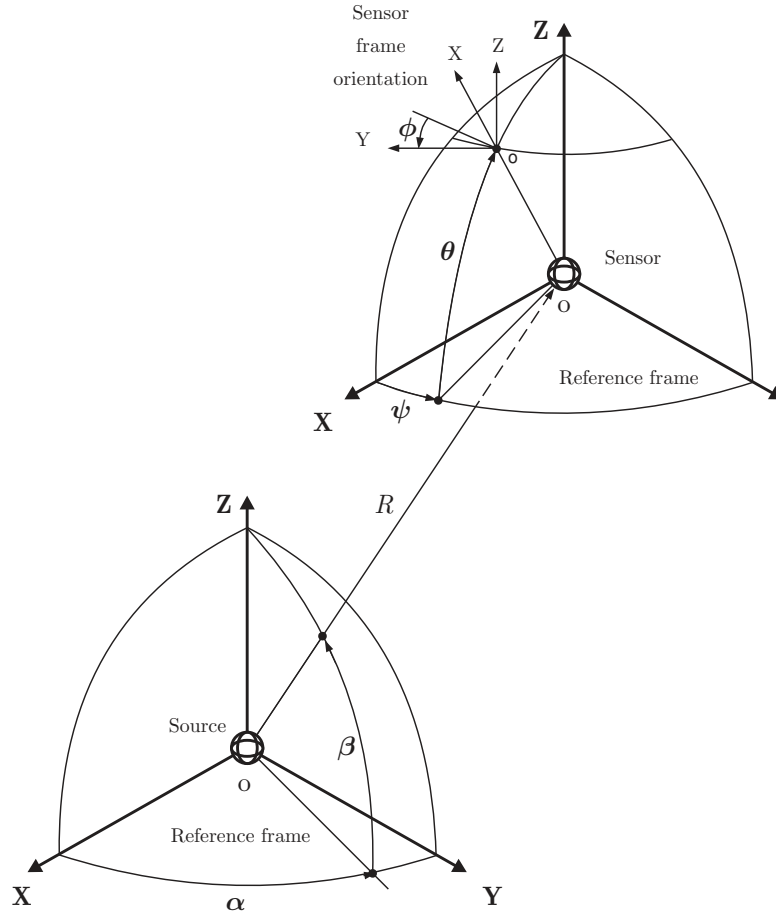
Figure 5.8 — Six degrees of freedom between reference source frame and sensor frame. The sensor position (remote body) is given by R, α, and β and the orientation by ψ, ϕ, and θ.

source frame and is defined by:

$$
\mathbf{\Upsilon} = \begin{bmatrix} \cos\beta & 0 & -\sin\beta \\ 0 & 1 & 0 \\ \sin\beta & 0 & \cos\beta \end{bmatrix} \begin{bmatrix} \cos\alpha & \sin\alpha & 0 \\ -\sin\alpha & \cos\alpha & 0 \\ 0 & 0 & 1 \end{bmatrix}
$$

$$
= \begin{bmatrix} \cos\alpha\cos\beta & \sin\alpha\cos\beta & -\sin\beta \\ -\sin\alpha & \cos\alpha & 0 \\ \cos\alpha\sin\beta & \sin\alpha\sin\beta & \cos\beta \end{bmatrix} \tag{5.10}
$$

$\boldsymbol{\Psi}$ is the orientation matrix which relates the sensor frame with respect to the source frame:

$$
\begin{aligned}
\boldsymbol{\Psi} &= \begin{bmatrix} 1 & 0 & 0 \\ 0 & \cos\phi & \sin\phi \\ 0 & -\sin\phi & \cos\phi \end{bmatrix} \begin{bmatrix} \cos\theta & 0 & -\sin\theta \\ 0 & 1 & 0 \\ \sin\theta & 0 & \cos\theta \end{bmatrix} \begin{bmatrix} \cos\psi & \sin\psi & 0 \\ -\sin\psi & \cos\psi & 0 \\ 0 & 0 & 1 \end{bmatrix} \\
&= \begin{bmatrix} \cos\psi\cos\theta & \sin\psi\cos\theta & -\sin\theta \\ \cos\psi\sin\theta\sin\phi - \sin\psi\cos\phi & \sin\psi\sin\theta\sin\phi + \cos\psi\cos\phi & \cos\theta\sin\phi \\ \cos\psi\sin\theta\cos\phi + \sin\psi\sin\phi & \sin\psi\sin\theta\cos\phi - \cos\psi\sin\phi & \cos\theta\cos\phi \end{bmatrix}
\end{aligned}
\tag{5.11}
$$

The two rotation matrices $\boldsymbol{\Upsilon}$ and $\boldsymbol{\Psi}$, provide the means for relating the source frame to the sensor frame. To express the measured signals from the sensor frame into the source frame, first they are rotated back to the source frame, using the inverse of the matrix $\boldsymbol{\Upsilon}$, namely $\boldsymbol{\Upsilon}^{\mathrm{T}}$. Then, it can be rotated into the sensor frame using the orientation matrix $\mathbf{A}$. The excitation of the source (given by $\mathbf{E}_i$) can be related to the corresponding signals $\mathbf{E}_o$, measured by the magnetic sensors:

$$
\mathbf{E}_o = \mathbf{S}\mathbf{E}_i
\tag{5.12}
$$

where the sensed signal matrix $\mathbf{S}$ is given by:

$$
\mathbf{S} = k\boldsymbol{\Psi}\boldsymbol{\Upsilon}^{\mathrm{T}}\mathbf{C}_m\boldsymbol{\Upsilon}
\tag{5.13}
$$

with k being the electromagnetic field coupling or attenuation factor and $\mathbf{C}_m$ the coupling matrix. From equation 5.2, it can be found that the magnitude of the signal detected by the sensor when sensor and coil are coaxial ($\varphi = 0$) is twice the magnitude when sensor and coil are coplanar ($\varphi = \pi/2$). Moreover, if the co-axial coupling is positive, then the co-planar coupling is negative. Angle φ corresponds with tracking angles α and β depending on the activated coil. From this, the coupling matrix $\mathbf{C}_m$ can be defined:

$$
\mathbf{C}_m = \begin{bmatrix} 2 & 0 & 0 \\ 0 & -1 & 0 \\ 0 & 0 & -1 \end{bmatrix}
\tag{5.14}
$$

Source-to-Sensor distance

The far magnetic field of a coil decreases with the third order of distance, which means the attenuation factor k is proportional to $1/R^3$. To determine k, first $\mathbf{U}$ is defined:

$$
\mathbf{U} = \mathbf{S}^{\mathrm{T}}\mathbf{S} = k^2\boldsymbol{\Upsilon}^{\mathrm{T}}\mathbf{C}_m^2\boldsymbol{\Upsilon}
\tag{5.15}
$$

The trace of matrix $\mathbf{U}$ is the sum of the components on the main diagonal of the matrix $\mathbf{U}$.

$$
\begin{aligned}
\text{tr}\,(\mathbf{U}) &= \text{tr}\,\left(\mathbf{S}^{\text{T}}\mathbf{S}\right)\\
&= \text{tr}\,\left(k^2\mathbf{\Upsilon}^{\text{T}}\mathbf{C}^2\mathbf{\Upsilon}\right)\\
&= \text{tr}\,\left(k^2\mathbf{C}_m^2\right)\\
&= 6k^2
\end{aligned}
\tag{5.16}
$$

Since $\mathbf{U}$ is computed using the measured signal matrix $\mathbf{S}$, k can be derived:

$$
k = \sqrt{\text{tr}\left(\frac{\mathbf{U}}{6}\right)}
\tag{5.17}
$$

The expression for the distance R between source and sensor now becomes:

$$
R = R_0 \sqrt[3]{\frac{k_0}{k}}
\tag{5.18}
$$

with R_0 and k_0 being the initial calibration parameters of the system.

Angular Degrees of Freedom

The five remaining DOF will be determined by uncoupling the position and orientation matrices $\mathbf{\Upsilon}$ and $\mathbf{\Psi}$ which reside in the measured signal matrix $\mathbf{S}$. First, the signal matrix $\mathbf{S}$ will be divided by the value of k, resulting in matrix $\mathbf{M}$ which in independent of the distance R:

$$
\mathbf{M} = \mathbf{\Psi}\mathbf{\Upsilon}^{\text{T}}\mathbf{C}\mathbf{\Upsilon}
\tag{5.19}
$$

The coupling matrix $\mathbf{C}_m$ can be rewritten to:

$$
\mathbf{C}_m = 3\mathbf{E}_1 - \mathbf{I}
\tag{5.20}
$$

$$
\text{with } \mathbf{E}_1 = \begin{bmatrix} 1 & 0 & 0 \\ 0 & 0 & 0 \\ 0 & 0 & 0 \end{bmatrix}
\tag{5.21}
$$

and $\mathbf{I}$ a 3 by 3 identity matrix. Using this representation for $\mathbf{C}_m$, the following relations can be derived:

$$
\mathbf{M}^{\text{T}}\mathbf{M} = 3\mathbf{X} + \mathbf{I}
\tag{5.22}
$$

$$
\text{and} \quad \mathbf{\Psi}^{\text{T}}\mathbf{M} = 3\mathbf{X} - \mathbf{I}
\tag{5.23}
$$

$$
\text{where} \quad \mathbf{X} = \mathbf{\Upsilon}^{\text{T}}\mathbf{E}_1\mathbf{\Upsilon}
\tag{5.24}
$$

Note that equation 5.24 involves only the tracking matrix $\boldsymbol{\Upsilon}$, that is, $\mathbf{X}$ is independent of orientation matrix $\boldsymbol{\Psi}$. This equation can be solved for $\mathbf{X}$:

$$\mathbf{X} = \boldsymbol{\Upsilon}^{\mathrm{T}} \mathbf{E}_1 \boldsymbol{\Upsilon} = \tfrac{1}{3} \left(\mathbf{M}^{\mathrm{T}} \mathbf{M} - \mathbf{I} \right) \tag{5.25}$$

Each element of the matrix $\mathbf{X}$ must be a function of the tracking angles α and β.

$$\mathbf{X} = \begin{bmatrix} \cos^2\alpha\cos^2\beta & \cos\alpha\sin\alpha\cos^2\beta & -\cos\alpha\sin\beta\cos\beta \\ \cos\alpha\sin\alpha\cos^2\beta & \sin^2\alpha\cos^2\beta & -\sin\alpha\sin\beta\cos\beta \\ -\cos\alpha\sin\beta\cos\beta & -\sin\alpha\sin\beta\cos\beta & \sin^2\beta \end{bmatrix} \tag{5.26}$$

It is now easy to see that:

$$\tan\alpha = \frac{\sin\alpha}{\cos\alpha} = \frac{x_{22}}{x_{12}} \tag{5.27}$$

$$\sin\beta = \pm\sqrt{x_{33}} \tag{5.28}$$

Since the numerical values for x_{12}, x_{22} and x_{33} are derived from the normalized measurement matrix $\mathbf{M}$ using equation 5.24, these equations determine the tracking angles α and β.

To compute the relative orientation of the remote sensor, the inverse of the normalized signal matrix $\mathbf{M}$ is calculated from equation 5.19 [1]:

$$\mathbf{M}^{-1} = \boldsymbol{\Upsilon}^{\mathrm{T}} \mathbf{C}_m^{-1} \boldsymbol{\Upsilon} \boldsymbol{\Psi}^{\mathrm{T}}$$
$$= \tfrac{1}{2} \left(3\boldsymbol{\Upsilon}^{\mathrm{T}} \mathbf{E}_1 \boldsymbol{\Upsilon} - 2\mathbf{I} \right) \boldsymbol{\Psi}^{\mathrm{T}} \tag{5.29}$$

By using equations 5.24 and 5.22 the inverse of matrix M becomes:

$$\mathbf{M}^{-1} = \tfrac{1}{2} \left(3\mathbf{X} - 2\mathbf{I} \right) \boldsymbol{\Psi}^{\mathrm{T}}$$
$$= \tfrac{1}{2} \left(\mathbf{M}^{\mathrm{T}} \mathbf{M} - 3\mathbf{I} \right) \boldsymbol{\Psi}^{\mathrm{T}} \tag{5.30}$$

By multiplying this last equation on both sides by the signal matrix $\mathbf{M}$ followed by the multiplication by the orientation matrix $\boldsymbol{\Psi}$, the following result is obtained:

$$\boldsymbol{\Psi} = \tfrac{1}{2}\mathbf{M} \left(\mathbf{M}^{\mathrm{T}} \mathbf{M} - 3\mathbf{I} \right) \tag{5.31}$$

Using the definitions for $\boldsymbol{\Psi}$, and knowing the numerical values of the elements of matrix $\mathbf{M}$, the orientation angles can be calculated:

$$\tan\psi = \frac{\sin\psi}{\cos\psi} = \frac{\Psi_{12}}{\Psi_{11}} \tag{5.32}$$

$$\sin\theta = -\Psi_{33} \tag{5.33}$$

$$\tan\phi = \frac{\sin\phi}{\cos\phi} = \frac{\Psi_{23}}{\Psi_{33}} \tag{5.34}$$

---

[1] $\mathbf{C}_m^{-1} = \tfrac{1}{2} \left(3\mathbf{E}_1 - 2\mathbf{I} \right)$

It should be emphasized that solving for $\boldsymbol{\Upsilon}$ and $\boldsymbol{\Psi}$ using these matrix methods, can results in some hemispheric ambiguity. These ambiguities, however, are usually eliminated by the application boundaries.

The tracking angles α and β, and orientation of the magnetic sensor ψ, ϕ, and θ are calculated using single elements from Equations 5.26 and 5.31. A least square error method can be used to provide a more robust solution for these parameters.

Chapter 6

Ambulatory position and orientation tracking fusing magnetic and inertial sensing

D. Roetenberg, P. Slycke, and P.H. Veltink
Submitted
Xsens Technologies and University of Twente
patent pending [100]

6.1   Introduction

RECENT developments in miniature sensor technology have opened many possibilities for motion analysis outside the laboratory [13]. However, these ambulatory measurements do not yet provide full 6 degrees of freedom (DOF) information. Orientations of body segments can be estimated accurately by fusion of the signals from gyroscopes, accelerometers and magnetometers [30, 93]. By using the orientations of individual body segments, the knowledge about the segment lengths and joint characteristics, relative positions on the body and angles between segments can be estimated [8, 120, 67]. In this kinematic chain, model and orientation errors of joints and segments can accumulate in position errors in the connecting body parts. Moreover, to track complex joints and non-rigid body parts like the back and shoulder accurately, more than three degrees of freedom, as given by an orientation measurement, are required. Position measurements on the body are important in many applications. For example, the distance between the center of mass and the position of the feet is necessary to evaluate balance in daily life. In virtual reality applications, the position of the arm with respect to the head mounted display (HMD) should be known. Ergonomic studies would benefit from position measurements of the back to estimate its curvature to assess workload [11]. To get a better agreement between simulation results of a kinematic model and the measured data of a specific person, the model should be scaled to the geometry of that specific person [53].

Distances between body segments can principally not be assessed by numerical integration of the measured accelerations because of the unknown starting position. Only short-term estimates of position changes within seconds can be estimated due to the inherent integration drift. Giansanti et al. [37] used inertial sensors for accurate reconstruction of the movement of a body segment. However, these measurements were restricted to time-limited applications up to 4 seconds.

In the previous chapter, a portable magnetic system was presented to measure relative positions and orientations on the body. Magnetic trackers overcome line of sight restrictions related to optical and acoustic systems. The source was scaled and the system was designed to run on battery supply, making it suitable for body mounting and ambulatory measurements. The transmitter driver provides short current pulses in a sequence involving three coils having orthogonal axes. The three-axis magnetic sensor measures the strengths of each of the magnetic pulses that are related to the distance of the transmitter [58, 59]. Driving three orthogonal coils continuously requires a substantial amount of energy restricting the maximum measurement time and update rate with a set of batteries. Moreover, magnetic systems can be disturbed by ferromagnetic or other magnetic materials which will decrease their accuracy.

In this study, the previously described magnetic tracker is combined with minia-

ture inertial sensors. Accelerometers and gyroscopes measure fast changes in position and orientation, require less energy and are not sensitive for magnetic disturbances. The magnetic system is used as an aiding system and provides updates at a relatively low rate to obtain long-term stable assessment of relative positions. Since the magnetic dipole source is only required to be active during a short period of time, the average energy over time needed is limited. Measurements from both sources and *a priori* knowledge about their behavior are combined using a complementary Kalman filter structure. The output of the filter is used to correct drift errors from the inertial sensors and reduce errors related to magnetic disturbances.

The objective of this chapter is to design and evaluate a new system for ambulatory measurements of position and orientation on the body. The major requirements for such a system are small weight and size, and no impediment of functional mobility. The fusion scheme of the portable magnetic tracker with inertial sensors is presented and the accuracy of the implemented combination of position and orientation estimates is evaluated by several experiments and compared with an optical reference system.
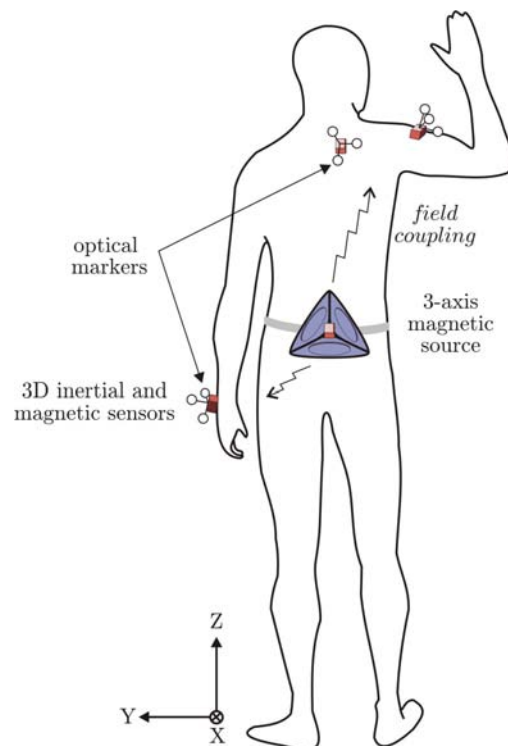

Figure 6.1 — Body-mounted magnetic system for measurement of relative distances and orientations on the body, consisting of a three-axis magnetic dipole-source worn by the subject and three-axis magnetic and inertial sensors on remote body segments.

6.2 System design

6.2.1 Magnetic tracking

The magnetic tracker is comprised of three essential components [88]: (1) an actuator, consisting of three orthogonal coils, which are fixed to the body and generate magnetic fields; (2) 3D magnetic sensors, fixed to several remote body segments, which measure the fields generated by the source; and (3) a processor whose function is to calculate relative distances and orientations on the body using the actuator and sensor signals and to control the distributed magnetic actuation and sensing system. Figure 6.2 shows the timing relationship of two cycles between a 3D orthogonal source and sensor. At time B_1, the X-source is activated, at B_2, the Y-source, and at B_3, the Z-source. At the end of a magnetic burst cycle, 9 values represent the relation in 6 DOF between source and sensor; three sensor values for each of the three transmitting coils. The equations presented by Kuipers [60] are used to calculate the 6 DOF (see Appendix 5.A). The three position coordinates are expressed in the magnetic frame (M) by $^M\mathbf{q}'$. The relative orientation between source and sensor is expressed by rotation matrix $^M\mathbf{\Psi}'$.

6.2.2 Inertial tracking

Rate gyroscopes measure angular velocity $\boldsymbol{\omega}$, and if integrated over time, provide the change in angle (or orientation) with respect to an initially known angle [14]:

$$^{GS}\dot{\boldsymbol{\Theta}}_t = {}^{GS}\boldsymbol{\Theta}_t \left[\boldsymbol{\omega}_t \times\right] \tag{6.1}$$

where $^{GS}\boldsymbol{\Theta}_t$ is the rotation matrix describing the transformation from sensor to global frame at time t. Linear accelerometers measure the vector of acceleration $\mathbf{a}$ and gravitational acceleration $\mathbf{g}$ in sensor coordinates (S). The sensor signals can be expressed in the global reference system (G) if the orientation of the sensor $^{GS}\boldsymbol{\Theta}_t$ is known:

$$^G\mathbf{a}_t - {}^G\mathbf{g} = {}^{GS}\boldsymbol{\Theta}_t \left(^S\mathbf{a}_t - {}^S\mathbf{g}\right) \tag{6.2}$$

After removing the gravity component, the acceleration $\mathbf{a}_t$ can be integrated once to velocity $\mathbf{v}_t$ and twice to position $\mathbf{p}_t$, all in the global frame:

$$\mathbf{v}_t = \mathbf{v}_0 + \int_{t_0}^{t} \mathbf{a}(\tau)d\tau \tag{6.3}$$

$$\mathbf{p}_t = \mathbf{p}_0 + \int_{t_0}^{t} \mathbf{v}(\tau)d\tau \tag{6.4}$$

where the initial velocity $\mathbf{v}_0$ and position $\mathbf{p}_0$ should be known.
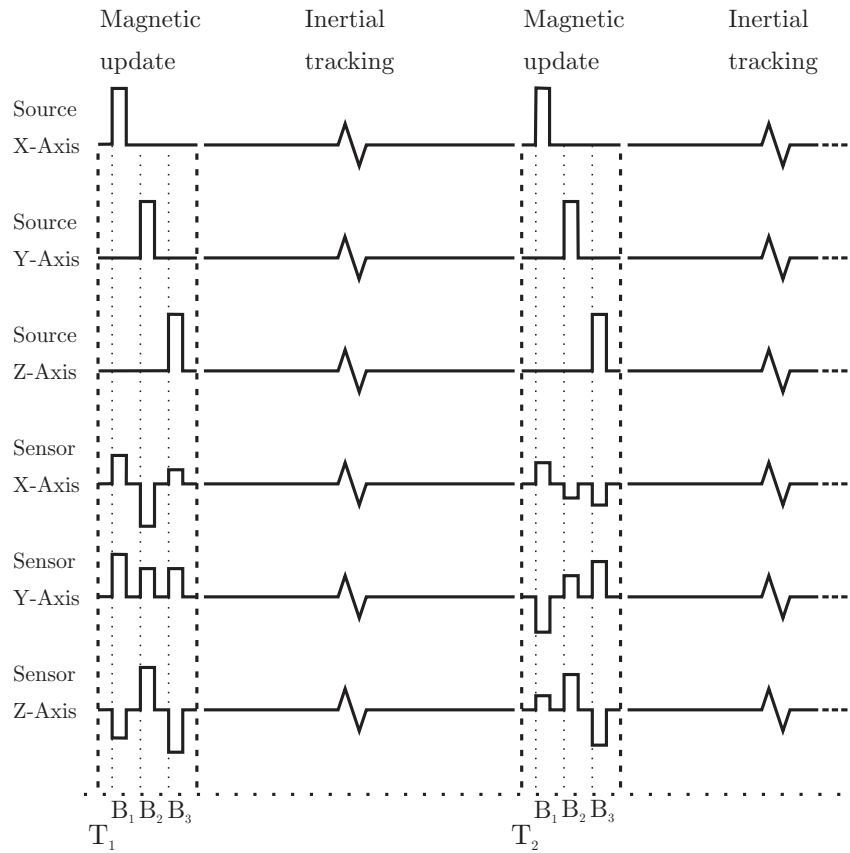
Figure 6.2 — Timing diagram of magnetic and inertial sensor fusion. During B_1 to B_3, three magnetic pulses are generated from which 6 DOF can be calculated. In between magnetic measurements, inertial sensors are used to track changes in position and orientation.

6.2.3 Sensor fusion

Fusing inertial measurements with other systems is well established in traditional navigation applications [16]. To blend the available data from the inertial sensors and magnetic system efficiently, a complementary Kalman filter has been designed (see Figure 6.3), which operates on the system errors. The inertial sensors provide output at a much higher rate than the magnetic tracking system. In between bursts of magnetic pulses, inertial measurements are used to track the changes in position and orientation using Equations 6.1 to 6.4 (see Figure 6.2). In traditional navigation, this is often referred to as dead reckoning. The input for the Kalman filter is the difference between the inertial and magnetic estimates of position and orientation at the end of an inertial tracking period. The Kalman filter processes the measurements to deduce a minimum error estimate of the states which are used to correct the inertial system.
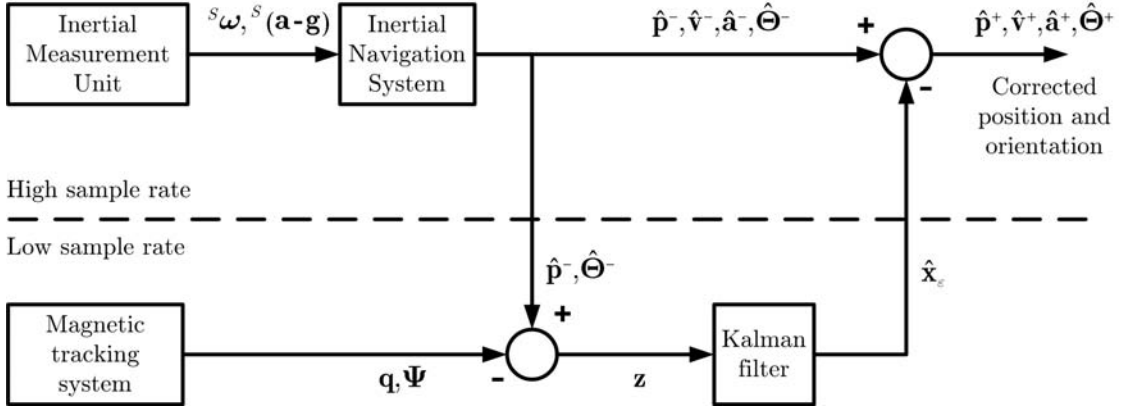
Figure 6.3 — Complementary Kalman filter structure for combining inertial and magnetic measurements. Position $\hat{\mathbf{p}}^-$ and orientation $\hat{\mathbf{\Theta}}^-$ are estimated at a high sampling rate, using the inertial navigation equations (6.1 to 6.4). At a lower rate, the magnetic system provides updates $\mathbf{q}$ and $\mathbf{\Psi}$. The differences between the two systems $\mathbf{z}$ is delivered to the Kalman filter which estimates the errors in the quantities of interest $\hat{\mathbf{x}}_\varepsilon$. These are used to correct position, velocity, acceleration and orientation estimates resulting in $\hat{\mathbf{p}}^+$,$\hat{\mathbf{v}}^+$,$\hat{\mathbf{a}}^+$ and $\hat{\mathbf{\Theta}}^+$.

Consider a discrete time error signal model, operating at a high sample rate as:

$$\mathbf{x}_{\varepsilon,t+1} = \mathbf{A}\mathbf{x}_{\varepsilon,t} + \boldsymbol{w}_t \tag{6.5}$$

where $\mathbf{A}$ is the state transition matrix from t to $t+1$. When a magnetic measurement comes available, the linear measurement equation for the data fusion Kalman filter can be represented by:

$$\mathbf{z}_{\varepsilon,t} = \mathbf{C}\mathbf{x}_{\varepsilon,t} + \boldsymbol{v}_t \tag{6.6}$$

where $\boldsymbol{w}_t$ and $\boldsymbol{v}_t$ represent process and measurement noise with covariance matrices $E\left[\boldsymbol{w}_t\boldsymbol{w}_t^{\mathrm{T}}\right] = \mathbf{Q}_t$ and $E\left[\boldsymbol{v}_t\boldsymbol{v}_t^{\mathrm{T}}\right] = \mathbf{R}_t$, respectively. The Kalman filter equations can be found in Figure 4.3 of Chapter 4. The outputs of the filter are used to correct the position, velocity, acceleration and orientation estimates resulting in $\hat{\mathbf{p}}^+$,$\hat{\mathbf{v}}^+$,$\hat{\mathbf{a}}^+$ and $\hat{\mathbf{\Theta}}^+$.

The magnetic system outputs 6 DOF of the sensor with respect to the position and orientation of the source. Since the source can move, no absolute position and orientation is given by this system. To estimate the orientation of the source $^{GM}\mathbf{\Phi}$, an inertial and magnetic sensor was attached to the source. The accelerometers provide a measure for inclination, the magnetometers are used as a compass to provide a reference in the horizontal plane and the gyroscopes measure fast changes in orientation by integrating angular velocities [93]. The position coordinates of the magnetic frame are aligned with the axes of the global frame, with the origin being the center of the source by using:

$$^{G}\mathbf{q}_t = {}^{GM}\mathbf{\Phi}_t{}^{M}\mathbf{q}'_t \tag{6.7}$$

Similar, to express the orientation of the sensor $^M\boldsymbol{\Psi}'$, measured by the magnetic system, in the global frame, it should be multiplied by $^{GM}\boldsymbol{\Phi}$ resulting in the orientation $^G\boldsymbol{\Psi}$.

Figure 6.4 shows an example of the coupling between a moving sensor module and a moving source source. At T_1 the magnetic system emits its sequence of three pulses, and the distance $\mathbf{q}_1$ between source and sensor can be determined. Then, the source on the back is moved by $\Delta\mathbf{p}_1$, and simultaneously, the sensor on the arm is moved over a distance $\Delta\mathbf{p}_2$. At T_2, the magnetic system provides an update of the position $\mathbf{q}_2$, which can be compared in the Kalman filter with the position estimate $\mathbf{p}$, by integrating of $\mathbf{a}_{net,t}$. The resulting net position change between source and sensor depends on the measured accelerations of the sensor and source in the global frame:

$$\mathbf{a}_{net,t} = \mathbf{a}_{sensor,t} - \mathbf{a}_{source,t} \tag{6.8}$$

When the magnetic update comes available at T_2, the inertial position and orientation estimates during T_1 to T_2 can be improved by running the Kalman filter backward in time. This can efficiently be implemented with the Rauch-Tung-Striebel (RTS) smoothing algorithm [35], described in Section 4.2.5. This approach is not possible for real-time applications. The improved estimates can be calculated with a delay of the time between updates (fix-lag smoothing) or the RTS algorithm can be executed in an off-line procedure (fixed-interval smoothing).

6.2.4 Error models

The fusion filter states consists of 21 error states for the position $\mathbf{p}_\varepsilon$, velocity $\mathbf{v}_\varepsilon$, orientation $\boldsymbol{\Theta}_\varepsilon$, accelerometer bias $\mathbf{a}_\varepsilon$, gyroscope bias $\boldsymbol{\omega}_\varepsilon$, magnetic position error $\mathbf{q}_\varepsilon$, and magnetic orientation error $\boldsymbol{\Psi}_\varepsilon$, all in the three directions:

$$\mathbf{x}_{\varepsilon,t} = [\mathbf{p}_{\varepsilon,t}, \mathbf{v}_{\varepsilon,t}, \boldsymbol{\Theta}_{\varepsilon,t}, \mathbf{a}_{\varepsilon,t}, \boldsymbol{\omega}_{\varepsilon,t}, \mathbf{q}_{\varepsilon,t}, \boldsymbol{\Psi}_{\varepsilon,t}]^{\mathrm{T}} \tag{6.9}$$

The discrete inertial error model with timestep Δt, follows directly from Equations 6.1 to 6.4. The position error is calculated by the integration of the velocity error:

$$\mathbf{p}_{\varepsilon,t+1} = \mathbf{p}_{\varepsilon,t} + \Delta t \mathbf{v}_{\varepsilon,t} \tag{6.10}$$

The velocity error is the integration of the acceleration error and the orientation error multiplied by the measured acceleration signal:

$$\mathbf{v}_{\varepsilon,t+1} = \mathbf{v}_{\varepsilon,t} + \Delta t \left({}^G\left(\mathbf{a}_t - \mathbf{g}\right) \times \boldsymbol{\Theta}_{\varepsilon,t} + \mathbf{a}_{\varepsilon,t} \right) \tag{6.11}$$

The orientation error can be found by taking the first order approximation of the strapdown integration step:

$$\boldsymbol{\Theta}_{\varepsilon,t+1} = \boldsymbol{\Theta}_{\varepsilon,t} + \Delta t \left[\boldsymbol{\omega}_{\varepsilon,t} \times\right] \tag{6.12}$$
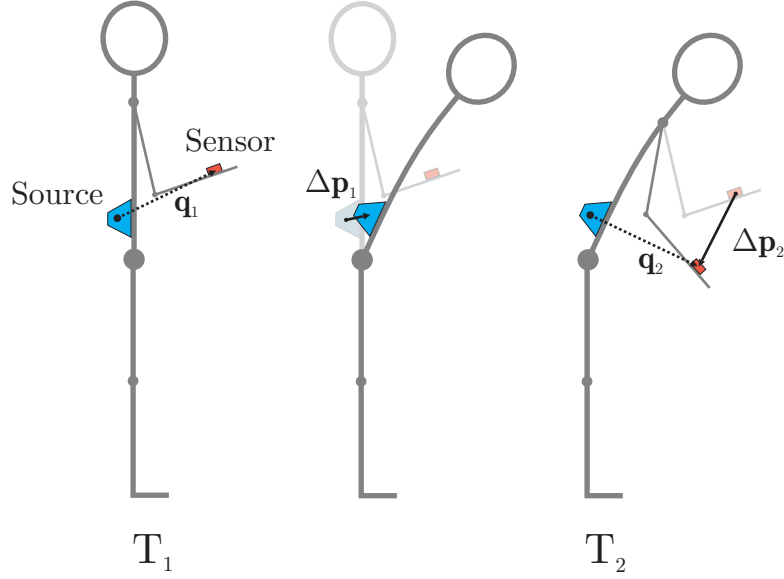
Figure 6.4 — Relative coupling between source and sensor. The source is placed on the back of the subject, the sensor on the wrist. At T_1 $\mathbf{q}_1$ is determined by the magnetic system. Then, the source on the back is moved by $\Delta\mathbf{p}_1$, and simultaneously, the sensor on the arm is moved over a distance $\Delta\mathbf{p}_2$. At T_2, the magnetic system provides an update of the position $\mathbf{q}_2$.

The acceleration and angular velocity errors $\mathbf{a}_{\varepsilon,t}$ and $\boldsymbol{\omega}_{\varepsilon,t}$ are modeled as first order Markov processes:

$$\mathbf{a}_{\varepsilon,t+1} = \mathbf{a}_{\varepsilon,t}e^{-\beta_a\Delta t} \tag{6.13}$$

$$\boldsymbol{\omega}_{\varepsilon,t+1} = \boldsymbol{\omega}_{\varepsilon,t}e^{-\beta_\omega\Delta t} \tag{6.14}$$

From the results in Chapter 5, we can conclude that there is no correlation between successive samples from magnetic position and orientation measurements and the magnetic position error $\mathbf{q}_{\varepsilon,t}$ model and orientation error $\boldsymbol{\Psi}_{\varepsilon,t}$ model are zero:

$$\mathbf{q}_{\varepsilon,t+1} = \mathbf{0} \tag{6.15}$$

$$\boldsymbol{\Psi}_{\varepsilon,t+1} = \mathbf{0} \tag{6.16}$$

The state transition matrix $\mathbf{A}_t$ is defined from equations 6.10 to 6.16:

$$\mathbf{A}_t = \begin{bmatrix} \mathbf{I}_3 & \Delta t\mathbf{I}_3 & \mathbf{0} & \mathbf{0} & \mathbf{0} & \mathbf{0} & \mathbf{0} \\ \mathbf{0} & \mathbf{I}_3 & \Delta t\left[(\mathbf{a}-\mathbf{g})\times\right] & \Delta t\mathbf{I}_3 & \mathbf{0} & \mathbf{0} & \mathbf{0} \\ \mathbf{0} & \mathbf{0} & \mathbf{I}_3 & \mathbf{0} & [\Delta t\times] & \mathbf{0} & \mathbf{0} \\ \mathbf{0} & \mathbf{0} & \mathbf{0} & e^{-\beta_a\Delta t}\mathbf{I}_3 & \mathbf{0} & \mathbf{0} & \mathbf{0} \\ \mathbf{0} & \mathbf{0} & \mathbf{0} & \mathbf{0} & e^{-\beta_\omega\Delta t}\mathbf{I}_3 & \mathbf{0} & \mathbf{0} \\ \mathbf{0} & \mathbf{0} & \mathbf{0} & \mathbf{0} & \mathbf{0} & \mathbf{0} & \mathbf{0} \\ \mathbf{0} & \mathbf{0} & \mathbf{0} & \mathbf{0} & \mathbf{0} & \mathbf{0} & \mathbf{0} \end{bmatrix} \tag{6.17}$$

where $\mathbf{I}_3$ is a 3×3 identity matrix and $\mathbf{0}$ a 3×3 matrix of zeros. It is assumed that the noise for each state variable is uncorrelated with the noise for each other state. Hence, all non-diagonal terms of the noise matrix $\mathbf{Q}_t$ matrix are zero and the diagonal terms are simply the variances of the random variables.

6.2.5 Measurement model

The first measurement presented to the Kalman filter is the position measured by the magnetic system $\mathbf{q}_t$ minus the inertial position estimate $\mathbf{p}_t$. For the orientation correction, there are several alternatives to combine the inertial and magnetic measurements:

1. Compare orientation $\mathbf{\Theta}_t$ with magnetic orientation estimates expressed in the global frame $\mathbf{\Psi}_t$. The discrete measurement model is formed from the inertial position error $\mathbf{p}_{\varepsilon,t}$ and magnetic position error $\mathbf{q}_{\varepsilon,t}$, and the elements of the inertial orientation error $\mathbf{\Theta}_{\varepsilon,t}$ and magnetic orientation error $\mathbf{\Psi}_{\varepsilon,t}$:

$$\mathbf{C}_t = \left[\begin{array}{ccccccc} \mathbf{I}_3 & \mathbf{0} & \mathbf{0} & \mathbf{0} & \mathbf{0} & \mathbf{I}_3 & \mathbf{0} \\ \mathbf{0} & \mathbf{0} & \mathbf{I}_3 & \mathbf{0} & \mathbf{0} & \mathbf{0} & \mathbf{I}_3 \end{array} \right] \tag{6.18}$$

2. Compare orientation $\mathbf{\Theta}_t$ with the orientation $\mathbf{\Xi}_t$ obtained by fusing the accelerometer, gyroscope and magnetic signals from the sensor module as described in Chapter 2. The error state $\mathbf{x}_{\varepsilon,t}$ is expanded with an additional state:

$$\mathbf{x}_{\varepsilon,t} = [\mathbf{p}_{\varepsilon,t}, \mathbf{v}_{\varepsilon,t}, \mathbf{\Theta}_{\varepsilon,t}, \mathbf{a}_{\varepsilon,t}, \boldsymbol{\omega}_{\varepsilon,t}, \mathbf{q}_{\varepsilon,t}, \mathbf{\Psi}_{\varepsilon,t}, \mathbf{\Xi}_{\varepsilon,t}]^{\mathrm{T}} \tag{6.19}$$

The measurement model becomes:

$$\mathbf{C}_t = \left[\begin{array}{cccccccc} \mathbf{I}_3 & \mathbf{0} & \mathbf{0} & \mathbf{0} & \mathbf{0} & \mathbf{I}_3 & \mathbf{0} & \mathbf{0} \\ \mathbf{0} & \mathbf{0} & \mathbf{I}_3 & \mathbf{0} & \mathbf{0} & \mathbf{0} & \mathbf{0} & \mathbf{I}_3 \end{array} \right] \tag{6.20}$$

The first measurement model would be most obvious, considering both systems have 6 DOF as outputs. The orientation used in the second model is not an independent measurement. It is correlated with the signals of the inertial navigation system (see Appendix 4.A). In Section 5.4 we have seen that the orientation errors of the magnetic system are high, namely 5.9°. An error in inclination estimate of 1 degree will result in an acceleration error of 0.17 ms^{-2}. This makes it difficult to correct drift errors of the gyroscope. The fusion orientation estimate $\mathbf{\Xi}_t$ appeared to be more accurate than the magnetic orientation estimate $\mathbf{\Psi}_t$ (see Section 5.4). Therefore, we used both measurements in the implemented system:

3. In between magnetic updates, only gyroscopes are used to track orientation changes. At a magnetic update, the orientation measurement will consist of

the gyroscope integration, and the weighted sum of the magnetic and fusion orientation:

$$\mathbf{C}_t = \left[\begin{array}{cccccccc} \mathbf{I}_3 & \mathbf{0} & \mathbf{0} & \mathbf{0} & \mathbf{0} & \mathbf{I}_3 & \mathbf{0} & \mathbf{0} \\ \mathbf{0} & \mathbf{0} & \mathbf{I}_3 & \mathbf{0} & \mathbf{0} & \mathbf{0} & \mathbf{I}_3 & \mathbf{I}_3 \end{array} \right] \tag{6.21}$$

The fusion weights of the measurements are assigned by the values of the covariance matrix $\mathbf{R}_t$. The $\mathbf{R}_t$ parameter is the variance associated with the white measurement noise $\boldsymbol{v}_t$. The noise in one direction is assumed to be uncorrelated with the noise in another direction. Therefore, the non-diagonal elements of the measurement covariance matrix $\mathbf{R}_t$ matrix are zero.

6.3 Experimental methods

Three coils were mounted in an orthogonal arrangement as illustrated in Figure 6.1. Coil dimensions were optimized to minimize approximation errors of a coil compared to a magnetic dipole (see Section 5.2.1). The number of windings was 50, the diameter 5.5 cm and the maximum current through the coil 1.5 A. The duration of the magnetic pulses was set at 60 ms, the cycle time (T_1 to T_2) was 600 ms. The driving electronics were designed to run on 4 AA (2400 mAh) batteries, making the whole system portable. MTx (Xsens Motion Technologies) sensor modules were used to measure angular velocities, accelerations, and strengths of magnetic pulses and the earth field in 3D. The sample frequency of the sensors was 120 Hz with 16 bits resolution. A Vicon 470 system (Oxford Metrix) consisting of 6 cameras operating at 120 Hz was used as a reference. Three optical markers with a diameter of 25 mm were attached to each sensor module in an orthogonal arrangement to validate the sensor's position and orientation with respect to the position of the coils. One sensor module with markers was attached to the source.

We used the same set of data as described in Section 5.3. In the first experiments, the set of coils was placed on a table. One sensor was moved by hand near the coils. In this bench-test, distances were varied slowly from approximately 10 cm to 80 cm and the sensor was rotated along all axes. In the following experiments, the three perpendicular coils were attached to the lower back. One sensor was placed on the back of a subject, at the level of the first thoracic vertebra and one sensor was placed on the proximal part of the upper arm. The subject performed flexion - extension and abduction - adduction of the arm followed by standard anatomical movements of the back: flexion, lateral flexion and rotation. In the final tests, the sensor was placed on the upper leg, just above the knee. The subject walked across the laboratory at a comfortable pace for a number of steps. All experiments were repeated 10 times.

6.4 Results

Figure 6.5 shows the results of an experiment where the subject performed flexion and extension of the back three times. In figure (a), we can see that the orientation of the source $\boldsymbol{\Phi}$ is changed during the movement. The magnetic source frame can be rotated and aligned with the global frame because this orientation is measured. In figure (b), distance measurements between the source and sensor on the back are plotted for the magnetic and reference system. During flexion, the distance increases a few cm. Figure (c) shows the X, Y and Z coordinates of the sensor with respect to the center of the source using the described Kalman filter. From the initial coordinates, we find the sensor about 45 cm above the source (Z-coordinate), 5 cm to right (Y-coordinate) and 6 cm forward (X-coordinate). During flexion, the X-position increases, the Z-coordinate decreases, while in the Y-direction, there is hardly movement. At negative values of the Z-coordinate, the sensor is positioned lower than the source as can be seen in figure (a). The root mean square (rms) position error of this trial is 4.7 mm compared optical reference measurements.

Figure 6.6 shows a typical example from an experiment where the subject performed ab- and adduction of the arm. In the upper graphs, the distance estimates between the source on the back and the proximal part of the upper arm are plotted which is between 38 and 50 cm. The solid line represents the reference measurement, the stars (*) are the magnetic updates, and the dotted line is the Kalman fusion of the magnetic and inertial measurements. The middle graph shows the errors of the magnetic system and Kalman filter. The rms position error of the magnetic system of this trial is 7.2 mm. The rms error of the Kalman filter is significantly lower with 4.6 mm. In the lower graph, the differences between the orientations obtained with the reference system and the inertial-magnetic measurements are given. The error is the smallest angle about which the sensor frame has to be rotated to coincide with the reference frame and is 2.1° rms for this trial.

Table 6.1 shows the numerical results of all performed experiments. The position error is defined as the shortest distance between the coordinates from the Kalman filter and the reference coordinates. The orientation error is defined as the smallest angle about which the sensor frame has to be rotated to coincide with the reference frame. If we compare these results with those reported in the previous chapter (Table 5.1), we can observe a significant improvement in the accuracy. Because the orientation estimates of the magnetic system $\boldsymbol{\Psi}$ were combined with those of the fusion algorithm $\boldsymbol{\Xi}$, the orientation accuracy also improved and did not differ much between different movements. They are comparable to the results reported in Chapter 3.

(a) Position and orientation of the source and sensor change during flexion.

(b) Distance between source and sensor.
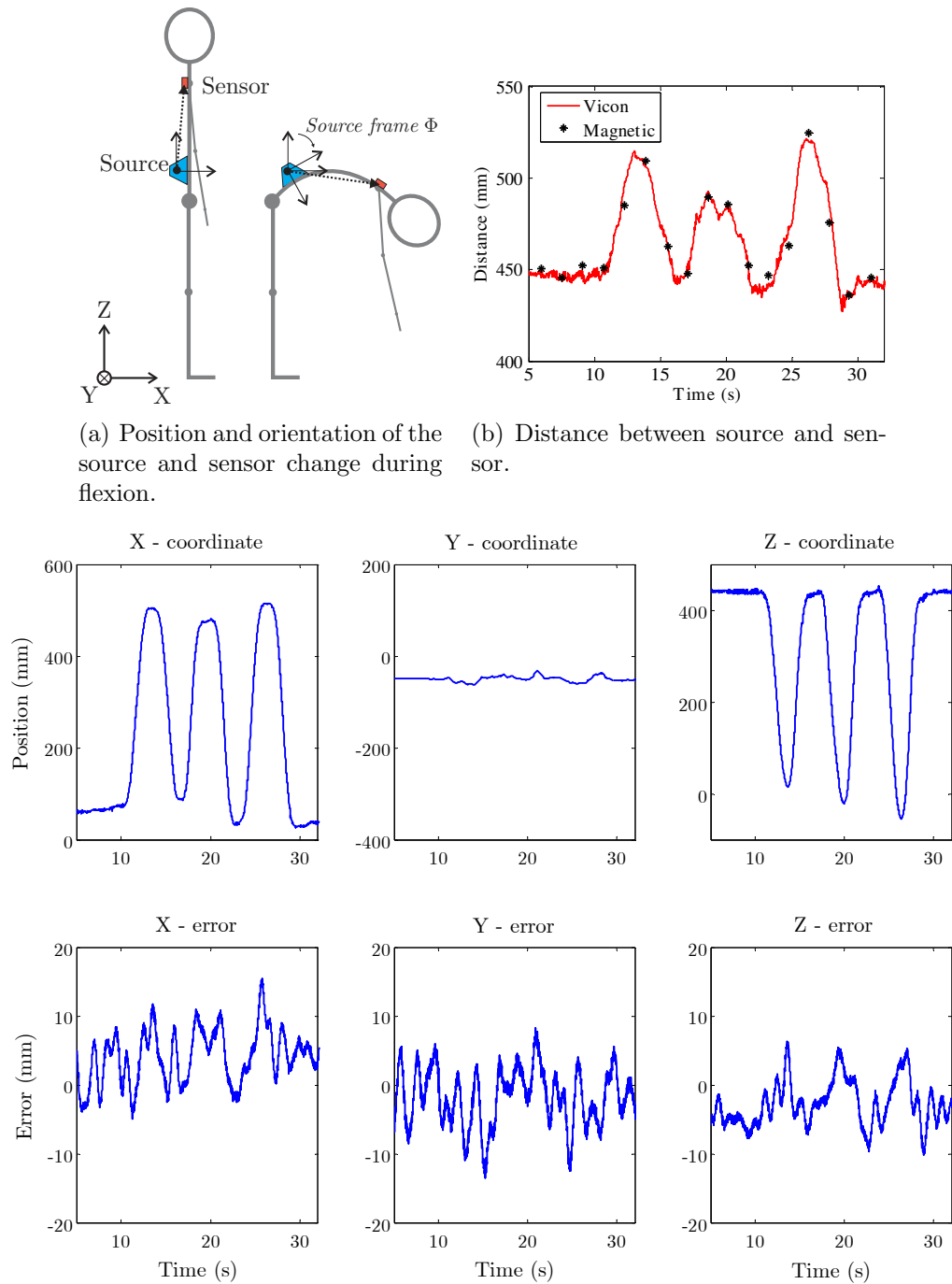
(c) Upper: X, Y and Z coordinates of the sensor with respect to the center of the source. The subject performed three times flexion of the back. Lower: Error in coordinates using inertial and magnetic sensing compared with optical references system.

Figure 6.5 — Experimental results of magnetic and inertial sensor fusion.
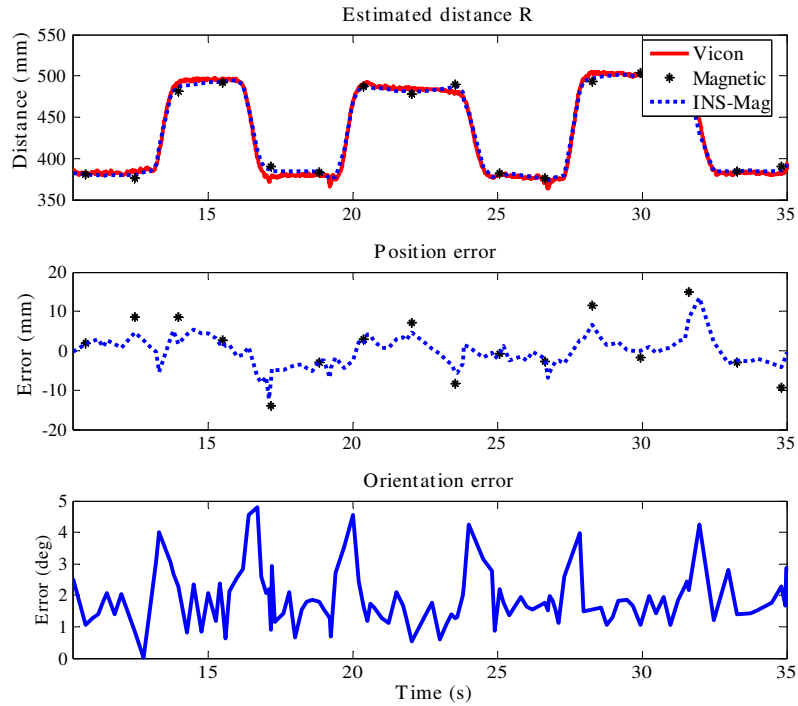
Figure 6.6 — The upper graph shows the distance between the source on the back and the sensor on the upper arm while performing ab- and adduction of the arm. The solid line represents the reference measurement by Vicon. The magnetic updates are indicated by the stars (*), and the dotted line is the Kalman fusion of the magnetic and inertial measurements. The middle graph shows the errors of the magnetic system and Kalman filter. The lower graph shows the differences between the orientation obtained with the reference system and the inertial-magnetic measurements.

Segment	Movement	Position error [mm]		Orientation error [deg]	
		RMS	SD	RMS	SD
Bench-test		5.2	1.1	3.0	0.6
Back	*Flexion*	4.8	1.1	2.4	0.5
	Latero-flexion	5.0	0.9	2.6	0.5
	Rotation	4.9	1.0	2.6	0.5
	Walking	5.6	1.8	3.0	0.6
Arm	*Flexion*	5.1	1.3	2.4	0.5
	Abduction	5.0	1.6	2.3	0.5
	Walking	7.9	2.6	3.1	0.6
Leg	*Walking*	8.6	2.8	3.2	0.6

Table 6.1 — RMS position and orientation errors and their standard deviations (SD) of the magnetic and inertial sensor fusion algorithm. All movements were performed 10 times.

6.5 Discussion

In this study, the combination of magnetic measurements and inertial sensors for fully ambulatory position and orientation tracking is examined. Given the actuator and sensor signals, the magnetic system determines their relative positions and orientations in 6 degrees of freedom. This is combined in a Kalman filter to provide actual distance measurements on the body and correct drift errors in estimates of position and orientation changes by the inertial sensors. Experiments were performed with only one subject, but the results show the feasibility of the proposed measurement system. A full evaluation on a wider range of movements needs to be performed.

Experiments with relatively slow movements of the arm and back showed significantly lower errors than the experiments where walking was evaluated. The main reason for these higher errors was the relative movement between sensor and source within one cycle of bursts B_1 to B_3 (Figure 6.2). In the algorithm for the 6 DOF calculations, the relative position and orientation between source and sensor are assumed to be fixed during one cycle. If these movements are not taken into account, errors are introduced, especially during fast movements. The time B_1 to B_3 can be shortened, but requires some adaptations of the used sensor hardware. The movements of the source and sensor during the cycle of pulsing can be estimated by $\mathbf{a}_{source}$ and $\mathbf{a}_{sensor}$, respectively. The distance between source and sensor can be assessed for each pulse and by triangulation of these distances, the relative position can be obtained. The acceleration of the source $\mathbf{a}_{source,t}$ is now related to orientation errors of the source $\mathbf{\Phi}$. This can be improved by incorporating $\mathbf{\Phi}$ in the fusion scheme.

The actuator has a working range of about 70 cm and is placed on the back of a person. This is sufficient to track, for example, shoulder or hip movements. For full ambulatory body tracking, the coil configuration should be optimized. Multiple sets of coils can be mounted on and around body parts. The fusion of the two complementary systems showed significantly better results than the magnetic tracker solely. Emura and Tachi [27] already reported improvements in angle estimation by combining a fixed lab magnetic tracking system with rate gyroscopes.

For the proposed portable system, increasing the signal-to-noise ratio of magnetic tracker can greatly improve the accuracy. In the measurement model, we have chosen to correct orientation errors with the magnetic orientation and the orientation obtained by fusing signals from gyroscopes, accelerometers and magnetometers. With a higher accuracy of the magnetic system, the fusion weight of the related orientation estimates can be increased. The error as a function of the distance or orientation between source and sensor was not taken into account. Incorporating this behavior in the models can also improve the accuracy.

In the experiments, the cycle time of the magnetic updates and current through the coils were fixed. To minimize drift errors, inertial position estimates should be updated at a relatively high rate, however, it will cost more energy. This can be optimized by weighting the accuracy requirements and maximum measurement time with a set of batteries. With the used settings, we were able to record for about 30 minutes. In off-line or near real-time analyses, the R.T.S. smoothing algorithm can be used, which will reduce errors as can be concluded from the results presented in Figure 4.9 in Chapter 4.

Several studies report effects of nearby conductive and magnetic materials on the accuracy of tracking using magnetic systems [81, 61]. The tracker was tested without metals in the vicinity. It should be investigated how these materials interfere with the emitted magnetic fields. However, since inertial sensors are not affected by magnetic fields, we expect significantly less problems than using magnetic tracking only.

This system does not provide the position of a person in, for example, a room. For indoor use, additional magnetic sources or a local positioning system based on a different physical principle can be placed in the measurement volume. An estimate in the horizontal plane with respect to a known starting point can also be made by means of a gait phase detector or advanced step counter using inertial sensors on the feet [97, 112, 96]. For outdoor applications, a system such as GPS or wireless networks can provide coordinates [40].

The proposed system opens many possibilities for ambulatory biomedical research and monitoring. By providing biomechanical models with position and orientation measurements of body segments, various parameters like angle joints and moments can be calculated. By combining it with instrumented shoes to measure ground reaction forces proposed by Veltink et al. [111], fully biomechanical analyses are feasible.

Chapter 6. Ambulatory position and orientation tracking

Chapter 7

General discussion

H UMAN MOTION tracking using inertial and magnetic sensing has been the central theme of this thesis. We have developed and evaluated algorithms and devices to measure orientation and position of body segments.

In **Chapter 2**, a so-called attitude and heading reference system was developed in which the effects of magnetic disturbances were taken into account. The evaluation of this algorithm in **Chapter 3** showed accurate and drift free orientation estimates for these sets of data. In other experiments, we observed a decrease in accuracy when a measurement was started in a heavily disturbed area. Also, the settings of the filter parameters required some tweaking. The initialization of the orientation is determined by the first samples from the accelerometers and magnetometers. In case these measurements are disturbed, the initial reference frame is not accurate. The magnetic disturbance model is such that it will converge to the initial settings. Incorporating a more complex disturbance filter can improve the orientation estimates under such circumstances. Accelerations are now modeled as a first order Markov process. Better results are expected when the bandwidth of the sensed movements is taken into account.

Although an optical system, such as Vicon, is often marked as a golden standard in human motion analysis, it has its limitations. Some measurement errors were already presented in **Chapter 3**. Orientation estimates using miniature inertial and magnetic sensors are getting close the accuracy of optical orientation measurements and in some cases even perform better. In **Chapter 4**, a method has been presented in which the position and orientation estimates of inertial sensors are used to improve performances of an optical tracking system. Gaps of optical data can be filled accurately, and high dynamic measurements of accelerations and velocities are possible by combining both systems.

In **Chapter 5**, a magnetic tracker has been developed as an aiding system for inertial position estimates. The choice for a magnetic system was based on possibility to make this system portable and the transparency of the human body for magnetic fields. The prototypes developed within our group showed the feasibility of this idea. As we have seen in the experiments, the accuracy of distance measurements was approximately 8 mm. Errors were higher during fast movements due to under sampling and were depending on the distance between source and sensor. Another disadvantage of the magnetic tracker is its susceptibility for field disturbances due to (ferro)magnetic materials in the vicinity. However, by using an appropriate fusion filter with inertial sensors these problems can be reduced.

Chapter 6 presents the combination of the magnetic tracker with inertial sensors. The accuracy and update rate of this sensor fusion showed significant improvements over magnetic tracking solely. Relative positions and orientations on the body can be tracked without the need for an external reference. However, mounting of the currently used coils to the body is not practical and the working range of the magnetic system is too low for full body monitoring. To use it in

clinical practice, many issues should be investigated. The following sections give a direction for possible improvements.

7.1 Sensor fusion

In the design of sensor fusion filters, there are many ways to choose the prediction steps, model states and measurement models. For the measurements of human motion, various aspects were taken into consideration, like the type of movements to be evaluated, the quality of the sensors, the available data and update rate of the aiding system. The fusion algorithms were designed in the form of complementary or error state Kalman filters. The Kalman filter is based on linear dynamic models and works optimal under the assumption of white measurement and process noise. Inertial and magnetic navigation is a non-linear problem, but their errors can be linearized. This implementation also has the advantage that it keeps the high dynamic responses necessary for human motion analysis.

In the filter of Chapter 2, the prediction step is performed before the actual filter equations. This may lead to sub-optimal estimates but the advantage is that no large matrix calculations are necessary which saves computational time; the inversion of a N by N matrix needs at least N^3 floating point operations [6]. Large matrix inversions in the covariance update can be avoided by processing uncorrelated measurements one at a time. In Chapter 4, the optical aiding system did not provide orientation information, but the position estimates were very accurate. With these position updates, the orientation errors during movement could be identified and corrected. Using the orientation estimation filter of Chapter 2 in this model was not optimal, due to the correlation between acceleration and orientation errors (see Appendix 4.A). The magnetic system developed in Chapter 5 provided both the relative position and orientation of the sensor with respect to the magnetic source. However, these measurements were noisy and therefore less suitable to correct gyroscope integration errors. The orientation obtained fusing the signals from gyroscopes, accelerometers and magnetometers as presented in Chapter 2 appeared to be more accurate under these conditions and was therefore used to correct the orientation estimates of the magnetic system. It is recommended to use only gyroscopes for orientation estimates if position estimates are accurate and the time between updates is relatively short. In contrast, when position estimates are noisy or the time between updates is relatively long, it is recommended to estimate the orientation with additional sensors as described in Chapter 2.

In the methods of Chapter 6, the magnetic and inertial measurements were processed separately. The independence of the aiding and INS navigation functions is also known as a loosely coupled (or decentralized) integration scheme. Another type of aided navigation is the tightly coupled (or centralized) strategy.

In tightly coupled schemes all measurements, for example, the individual GPS-satellites pseudoranges and IMU data, are processed together in the same filter. The main advantage of this technique is in preserving data availability. Another benefit of this type of integration comes from the fact that poor measurements can be detected and rejected from the solution. However, tightly coupled algorithms require higher computational load in comparison to loosely coupled schemes and usually have a complex system and measurement model.

Another approach, often described in literature to solve non-linear problems, is by means of an extended Kalman filter (EKF). The EKF implements a Kalman filter for a system dynamics that results from the linearization of the original non-linear filter dynamics around the previous state estimates. Theoretically, there is no difference between the EKF and the feedback complementary Kalman filter. Furthermore, the feedforward complementary Kalman filter is identical to the linearized filter [48]. With the increase of computation power over the last years, other solutions for non-linear problems such as particle filters have become a feasible option [41].

7.2 Magnetic actuation and sensing

Changing magnetic fields nearby conducting and ferrous materials cause secondary fields that will disturb the measurements. The coils were activated using current pulses to reduce the effect of these eddy currents. The rising edge of the pulse will cause an initial burst of eddy currents. After the pulse reaches its steady state value, however, no new eddy currents will be generated. Existing eddy currents then die out at an exponential rate proportional to the metal's conductivity, size and nearness. Sampling the transmitted signal close to its rising edge will thus result in a sensed signal containing large eddy current components. Sampling the signal farther from the leading edge results in less interference [5]. The use of AC fields can offer some advantages above pulses.

- Specific band filters can be used for the frequency of the emitted field, reducing the measurement noise.
- Each coil can be activated at the same time by using different frequencies for each coil. This will increase the update rate of the magnetic system, and the problem of sensor movement within one measurement cycle of three subsequent pulses will reduce significantly.
- AC fields can be generated with less energy.

It should be investigated to which extent AC fields are more disturbed by ferromagnetic materials than pulsed fields and which frequency is optimal.

The calculations to obtain the 6 DOF are based on a dipole approximation of a coil. In Section 5.2.1 we have seen that the field emitted by a true coil introduces

large approximation errors at distances comparable to the coil dimensions. As a result, the defined coupling matrix $\mathbf{C}_m$ in Appendix 5.A of Chapter 5 will not be accurate. The exact field values can be calculated using the Biot-Savart law (Equation 5.1). For each position and orientation, the 9 magnitudes (three pulses sensed by three sensors) can be stored in a look-up table on a suitably defined grid. The effect of errors on one or more of the measured field components can be simulated, which provide confidence intervals of the estimated 6 DOF. These confidence intervals can be used in the models for the fusion with inertial sensors.

The orthogonal arrangement of the coils enabled a straightforward analytical solution to determine 6 DOF. Instead of activating three perpendicular coils, a whole network of (smaller) sources can be used. Coils can be mounted on and around body parts, such as the arms, legs and torso and integrated in clothing. The relative position and orientation between the coils can vary during movement of the subject and should be measured with inertial sensor modules. An example of body-mounted coils integrated in a belt is given in Figure 7.1. In this asymmetric configuration, the center of the source is not a single point. However, the field coupling can be calculated for each coil, as described in the previous paragraph. By triangulation of the measured distances from each coil, relative positions can be obtained. Also, a biaxial transmitter can be used as proposed by Paperno and Keisar [85]. However, it will result in some low-resolution regions. Combining the distance of each source with orientation estimates and anatomical knowledge of joints will increase the accuracy and can provide full body tracking.
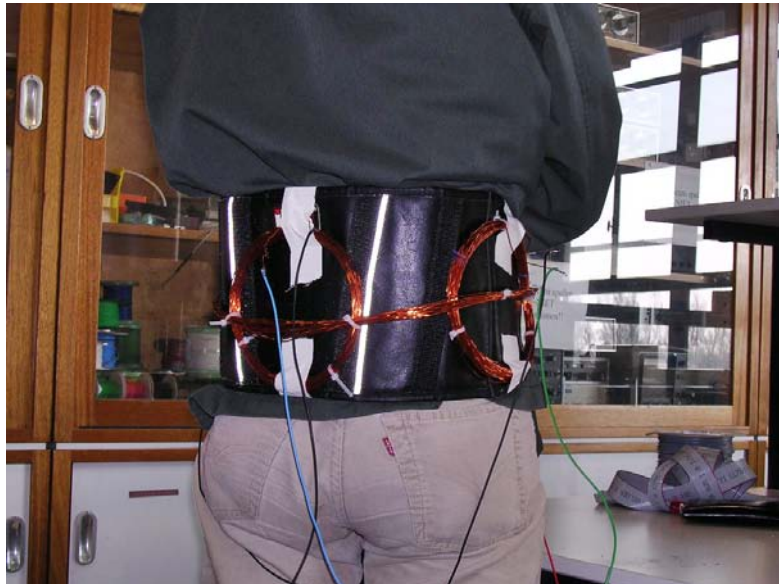

Figure 7.1 — Prototype of body-mounted magnetic tracking system with coils integrated in a belt.

In the performed experiments, the current through the coils was equal for each cycle. When the sensor is near the source and the signal-to-noise ratio is more than sufficient, the strength of the magnetic dipole can be decreased. Also, the duty cycle of magnetic updates was fixed. Drift errors of inertial sensors are larger when they are moved. Based on the values of the covariance matrices or estimated errors of the inertial system, the duty cycle of magnetic pulsing can be adapted. Both options can reduce the energy consumption and increase accuracy. The first feature will also prevent clipping of the magnetometer signals. When multiple users are wearing a magnetic system close to each other, the timing of pulsing should be controlled at a higher level to avoid cross-interference of the emitted magnetic fields.

When measuring weak magnetic fields, like the earth magnetic field, sensor offset and temperature effects can greatly reduce both the sensitivity and accuracy of magnetoresistive sensors. A technique called 'flipping' was used to cancel these effects. Flipping causes a change in the polarity of the sensor output signal. This can be used to separate the offset signal from the measured signal [106]. The unknown field in the 'normal' positive direction (plus the offset) is measured in one half of the cycle, while the unknown field in the 'inverted' negative direction (plus the offset) is measured in the second half. This results in two different outputs symmetrically positioned around the offset value. After filtering and rectifying, the output is free of offset. Although 'flipping' is necessary for stable magnetic field measurements, oscillations in the output signal may occur during pulsing, due to the large changes in field amplitude. To reduce these effects, timing of 'flipping' should occur before or after a burst of pulses and can be synchronized using the bus system to which the sensors are attached.

A concern that might arise when sending magnetic fields through the human body are safety issues. We found no signs of increased health risks with the strength of the used magnetic fields based on the studies by the *International Commission of Non-Ionizing Radiation Protection* [82, 83]. Moreover, magnetic trackers are already commercially available for years and no safety issues have been reported. Nevertheless, the effect of attaching coils closely to the body should be investigated in more detail. Although no tissue is affected by low-power and low-frequency fields, electronic equipment can be disturbed. For example, pacemaker warnings usually start at 5 Gauss, with manufacturers warning at 10 Gauss. However, the field measured a few cm from the coil was around 1 Gauss. Motion analysis is often combined with recordings of the electric activity of muscles; electromyography (EMG). From several studies which recorded EMG together with magnetic motion trackers, e.g. [25, 71], we found no evidence for the influence of magnetic fields on the EMG. Loops of wire should be avoided since they can cause induced electric fields.

7.3 Future directions and related research

Over the last years, many generations of inertial sensor modules have been introduced (e.g. InertiaCube, MT9, MTx) [50, 118]. The orientation of sensor module can be calculated real-time in an embedded processor which is convenient for extension of modules on the body. With each new type, the accuracy increased and noise levels went down. For orientation measurements, this implies the Kalman filter can rely more on the gyroscopes, and accelerometer and magnetometer weights are reduced. This will result in better inclination and magnetic disturbance estimates and therefore, less interference problems. Although gyroscopes drift rates are still quite high compared to large fiber optical gyros, in the near future, miniature gyroscopes might be accurate enough to be used for gyro compassing. A gyrocompass finds north by sensing the rotation of the earth. They have two main advantages over magnetic sensors for heading determination; firstly they find true north, i.e. the direction of earth's rotational axis, as opposed to magnetic north and secondly, they are not affected by metal. However, since the operation of a gyrocompass crucially depends on its rotation on earth, it won't function correctly if the vessel (or body part) it is mounted on is moving fast, especially in east-west direction.

Besides developments in sensor technology, advances can be expected in power supply (rechargeable batteries and fuel cells) and portable computational power (DSP's). With increasing battery capacity and power reduction of electronics and sensors, cables between sensor modules can be eliminated and data can be transferred by wireless communications. The ultra-wideband (UWB) technology seems to be very promising in high resolution ranging. UWB employs very short pulse waveforms that spread their energy over a broad part of the frequency spectrum [1]. Due to the inherently fine temporal resolution of UWB, arriving multi-path components can be sharply timed at a receiver to provide accurate time of arrival estimates. At this moment, UWB hardware is still quite bulky and expensive, because very high computer clock rates are necessary for exact timing determination, and special antennas are necessary to emit the fields. Moreover, for high frequency EM-fields, the human body is not transparent.

All calculations involving orientations were performed using rotation matrices. A different way to describe orientations is by means of quaternions. A quaternion $q = q_0 + \mathbf{i}q_1 + \mathbf{j}q_2 + \mathbf{k}q_3$ can be viewed as the sum of a real number q_0 (the real or scalar part of the quaternion) and a 3-vector $\mathbf{i}q_1 + \mathbf{j}q_2 + \mathbf{k}q_3$ in R3 (the imaginary or vector part) [38]. The advantages of quaternions are:

- non singular representation (compared with Euler angles for example)
- more compact (and faster computations) than matrices

To perform human motion analysis with this kind of sensor technology, human body segment kinematics have to be derived from the sensor kinematics. For this,

the relations between the sensor frame and the axes frame of the body segment on which the sensor is mounted has to be known. The effect of inaccuracies of the measurements of bony landmarks will result in errors in the assessment of bone rotations [73]. The sensors should be mounted as stable as possible after which the relative orientation and position between the sensor frame and functional axes of movement are determined. In a calibration procedure, sensor data is recorded while the body segment is rotated around one of its segment axes (e.g. arm flexion and extension) or aligned with one of the defined global frame axes (e.g. arm held horizontally) [10, 67]. It depends partly on the ability of the subject to consistently perform the required motions. The quality of this calibration procedure determines the quality of the clinical motion assessment. These issues are now under further investigation in the *FreeMotion* [32] project.

In this thesis, we have developed methods for on-body position estimates using inertial and magnetic and sensing and actuation. Although more research is necessary to apply this technology in clinical practice, we have demonstrated the feasibility of this concept. It opens many possibilities for ambulatory biomedical research and monitoring.

Bibliography

[1] Æther Wire & Location. `http://www.aetherwire.com`.

[2] E.J. Alexander and T.P. Andriacchi. Correcting for deformation in skin-based marker systems. *Journal of Biomechanics*, 34:355–361, 2001.

[3] S.E. Alper and T. Akin. A symmetric surface micromachined gyroscope with decoupled oscillation modes. *Sensors and Actuators A-Physical*, 97-8:347–358, 2002.

[4] K. Aminian and B. Najafi. Capturing human motion using body-fixed sensors: outdoor measurement and clinical applications. *Computer Animation and Virtual Worlds*, 15:79–94, 2004.

[5] Ascension Technology Corporation. Flock of Birds. `http://www.ascension-tech.com`.

[6] K.E. Atkinson. *An Introduction to Numerical Analysis.* John Wiley, second edition, 1989.

[7] R. Azuma and G. Bishop. Improving static and dynamic registration in an optical see-through HMD. In *Proceedings of SIGGRAPH '94*, Orlando, Florida, 1994.

[8] E.B. Bachmann. *Inertial and magnetic tracking of limb segment orientation for inserting humans into synthetic environments.* PhD Thesis, Naval Postgraduate School, 2000.

[9] C.T.M. Baten. Ambulatory spinal curvature estimation applying 3D motion analysis through inertial sensing for use in net spinal moment estimation. In *Seventh International Symposium on the 3-D Analysis of Human Movement*, Newcastle, 2002.

[10] C.T.M. Baten, H. Luinge, and H. van Moerkerk. Estimating body segment body orientation applying inertial sensing. In *The Sixth International Symposium on the 3-D Analysis of Human Movement*, Cape Town, 2000.

[11] C.T.M. Baten, H. van Moerkerk, I. Kingma, J. Van Dieën, T. Dolan, P.H. Veltink, and H.J. Hermens. Ambulatory low back load exposure estimation. In *XIVth tri-annual congress of the IEA/44th annual meeting HFES*, San Diego, 2000.

[12] E. Bernmark and C. Wiktorin. A triaxial accelerometer for measuring arm movements. *Applied Ergonomics*, 33(6):541–547, 2002.

[13] P. Bonato. Wearable sensors/systems and their impact on biomedical engineering. *IEEE Engineering in Medicine and Biology Magazine*, 22(3):18–20, 2003.

[14] J.E. Bortz. A new mathematical formulation for strapdown inertial navigation. *IEEE Transactions on Aerospace and Electronic Systems*, 7:61–66, 1971.

[15] C.V.C. Bouten, K.T.M. Koekkoek, M. Verduin, R. Kodde, and J.D. Janssen. A triaxial accelerometer and portable processing unit for the assessment of daily physical activity. *IEEE Transactions on Biomedical Engineering*, 44(3):136–147, 1997.

[16] R.G. Brown and P.Y.C. Hwang. *Introduction to random signals and applied Kalman filtering*. John Wiley, 3rd edition, 1997.

[17] H.J. Busser, W.G. de Korte, E.B.C. Glerum, and R.C. van Lummel. Method for objective assessment of physical work load at the workplace. *Ergonomics*, 41(10):1519–1526, 1998.

[18] H.J. Busser, J. Ott, R.C. van Lummel, M. Uiterwaal, and R. Blank. Ambulatory monitoring of children's activity. *Medical Engineering & Physics*, 19(5):440–5, 1997.

[19] M.J. Caruso. Application of magnetoresistive sensors in navigation systems. In *Sensors and Actuators, SAE SP-1220*, pages 15–21, 1997.

[20] D.K. Cheng. *Field and Wave Electromagnetics*. Addison-Wesley, 1989.

[21] W.K. Chiang. *INS/GPS Integration Using Neural Networks for Land Vehicular Navigation Applications*. PhD Thesis, University of Calgary, 2004.

[22] L. Chiari, U.D. Croce, A. Leardini, and A. Cappozzo. Human movement analysis using stereophotogrammetry: Part 2: Instrumental errors. *Gait & Posture*, 21(2):197–211, 2005.

[23] J.S. Day, G.A. Dumas, and D.J. Murdoch. Evaluation of a long-range transmitter for use with a magnetic tracking device in motion analysis. *Journal of Biomechanics*, 31(10):957, 1998.

[24] P. Desjardins, A. Plamondon, S. Nadeau, and A. Delisle. Handling missing marker coordinates in 3D analysis. *Medical Engineering & Physics*, 24(6):437–440, 2002.

[25] D.D. Ebaugh, P.W. McClure, and A.R. Karduna. Effects of shoulder muscle fatigue caused by repetitive overhead activities on scapulothoracic and glenohumeral kinematics. *Journal of Electromyography and Kinesiology*, In Press, 2005.

[26] Y. Ehara, H. Fujimoto, S. Miyazaki, M. Mochimaru, S. Tanaka, and S. Yamamoto. Comparison of the performance of 3D camera systems II. *Gait & Posture*, 5:251–255, 1997.

[27] S. Emura and S. Tachi. Multisensor integrated prediction for virtual reality. *Presence*, 7(4):410–422, 1998.

[28] Y. Feng, W. Grooten, P. Wretenberg, and U.P. Arborelius. Effects of arm suspension in simulated assembly line work: muscular activity and posture angles. *Applied Ergonomics*, 30:247–253, 1999.

[29] F. Ferraris, U. Grimalde, and M. Parvis. Procedure for effortless in-field calibration of three-axis rate gyros and accelerometers. *Sensors and Materials*, 7(5):311, 1995.

[30] E. Foxlin. Inertial head-tracker sensor fusion by a complementary separate-bias Kalman filter. In *Proceedings of VRAIS '96*, pages 185–194, 1996.

[31] E. Foxlin, M. Harrington, and G. Pfeifer. Constellation: A wide-range wireless motion-tracking system for augmented reality and virtual set applications. In *Proceedings of SIGGRAPH '98*, Orlando, Florida, 1998.

[32] FreeMotion. `http://freemotion.ambulab.nl`.

[33] C. Gabriel, S. Gabriel, and E. Corthout. The dielectric properties of biological tissues: I. literature surveys. *Physics in Medicine and Biology*, 41:2231–2249, 1996.

[34] J.R. Gage. Gait analysis: An essential tool in the treatment of cerebral palsy. *Clinical Orthopaedics and Related Research*, 288:126–134, 1993.

[35] A. Gelb. *Applied Optimal Estimation*. The M.I.T. press, 1974.

[36] D. Giansanti, V. Macellari, G. Maccioni, and A. Cappozzo. Is it feasible to reconstruct body segment 3-D position and orientation using accelerometric data? *IEEE Transactions on Biomedical Engineering*, 50(4):476–83, 2003.

[37] D. Giansanti, V. Macellari, G. Maccioni, and V. Macellari. The development and test of a device for the reconstruction of 3-D position and orientation by means of a kinematic sensor assembly with rate gyroscopes and accelerometers. *IEEE Transactions on Biomedical Engineering*, 52(7):1271–1277, 2005.

[38] Goldstein. *Classical Mechanics*. Addison-Wesley, 1977.

[39] M.S. Grewal, L.R. Weill, and A.P. Andrews. *Global Positioning Systems, Inertial Navigation, and Integration*. John Wiley, 2001.

[40] F. Gustafsson and F. Gunnarsson. Mobile positioning using wireless networks: possibilities and fundamental limitations based on available wireless network measurements. *IEEE Signal Processing Magazine*, 41(4):41–53, 2005.

[41] F. Gustafsson, F. Gunnarsson, N. Bergman, U. Forssell, J. Jansson, R. Karlsson, and P.-J. Nordlund. Particle filters for positioning, navigation, and tracking. *IEEE Transactions on Signal Processing*, 50(2):425–437, 2002.

[42] M. Haid and J. Breitenbach. Low cost inertial orientation tracking with Kalman filter. *Applied Mathematics and Computation*, 153(2):567–575, 2003.

[43] G.-Å. Hansson, P. Asterland, N.-G. Holmer, and S. Skerfving. Validity and reliability of triaxial accelerometers for inclinometry in posture analysis. *Medical & Biological Engineering & Computing*, 39(4):415–413, 2001.

[44] J. He and C-X. Tian. A statistical smoothness measure to eliminate outliers in motion trajectory tracking. *Human Movement Science*, 17(2):189–200, 1998.

[45] C. Hide, T. Moore, and M. Smith. Adaptive Kalman filtering for low cost INS/GPS. *The Journal of Navigation*, 56(1):143–152, 2003.

[46] C.D. Hide and T. Moore. Low cost sensors, high quality integration. In *Proceedings of NAV/AIS04*, 2004.

[47] A.L. Hof and E. Otten. Assessment of two-dimensional induced accelerations from measured kinematic and kinetic data. *Gait & Posture*, 22(3):182–188, 2005.

[48] J.D Hol. *Sensor Fusion for Camera Pose Estimation.* Master Thesis, University of Twente, 2005.

[49] S. Holzreiter. Autolabeling 3D tracks using neural networks. *Clinical Biomechanics*, 20(1):1–8, 2005.

[50] InterSense. `http://www.isense.com`.

[51] P. Jonker, S. Persa, J. Caarls, F. de Jong, and I. Lagendijk. Philosophies and technologies for ambient aware devices in wearable computing grids. *Computer Communications*, 26(11):1145–1158, 2003.

[52] R.E. Kalman. A new approach to linear filtering and prediction problems. *Journal of Basic Engineering*, 82:35–45, 1960.

[53] B.L. Kaptein and F.C.T. van der Helm. Estimating muscle attachment contours by transforming geometrical bone models. *Journal of Biomechanics*, 37(3):263–273, 2004.

[54] B. Kemp, A.J. Janssen, and B. van der Kamp. Body position can be monitored in 3D using miniature accelerometers and earth-magnetic field sensors. *Electroencephalography and Clinical Neurophysiology*, 109(6):484–488, 1998.

[55] T.M. Kepple, K.L. Siegel, and S.J. Stanhope. Relative contributions of the lower extremity joint moments to forward progression and support during gait. *Gait & Posture*, 6(1):1–8, 1997.

[56] D.V. Knudson and C.S. Morrison. *Qualitative analysis of human movement.* Human Kinetics, Champaign, III,, 2nd edition, 2002.

[57] K. Kobayashi, L. Gransberg, E. Knutsson, and P. Nolen. A new system for three-dimensional gait recording using electromagnetic tracking. *Gait & Posture*, 6(1):63, 1997.

[58] J. Kuipers. Object tracking and determining orientation of object using coordinate transformation means, system and process, Feb. 25 1975. US Patent 3,868,565.

[59] J. Kuipers. Tracking and determining orientation of object using coordinate transformation means, system and process, Sep. 26 1976. US Patent 3,983,474.

[60] J.B. Kuipers. *Quaternions and Rotation Sequences.* Princeton University Press, 1999.

[61] L. LaScalza, J. Arico, and R. Hughes. Effect of metal and sampling rate on accuracy of flock of birds electromagnetic tracking system. *Journal of Biomechanics*, 36:141–144, 2003.

[62] T.-W. Lu and J.J. O'Connor. Bone position estimation from skin marker co-ordinates using global optimisation with joint constraints. *Journal of Biomechanics*, 32:129–134, 1999.

[63] H.J. Luinge. *Inertial sensing of human movement.* PhD Thesis, University of Twente, 2002.

[64] H.J. Luinge and P.H. Veltink. Inclination measurement of human movement using a 3D accelerometer with autocalibration. *IEEE Transactions on Neural Systems & Rehabilitation Engineering*, 12(1):112–121, 2004.

[65] H.J. Luinge and P.H. Veltink. Measuring orientation of human body segments using miniature gyroscopes and accelerometers. *Medical & Biological Engineering & Computing*, 43:273–282, 2005.

[66] H.J. Luinge, P.H. Veltink, and C.T.M. Baten. Estimating orientation with gyroscopes and accelerometers. *Technology and Health Care*, 7(6):455–9, 1999.

[67] H.J. Luinge, P.H. Veltink, and C.T.M. Baten. Ambulatory measurement of arm orientation. *Journal of Biomechanics*, In Press, 2006.

[68] J.L. Marins, X. Yun, E.R. Bachmann, R.B. McGhee, and M.J. Zyda. An extended Kalman filter for quaternion-based orientation estimation using marg sensors. In *IEEE/RSJ International Conference on Intelligent Robots and Systems*, pages 2003–2011, 2001.

[69] R.B. Martins. A genealogy of biomechanics. In *23rd Annual Conference of the American Society of Biomechanics*, 1999.

[70] M.J. Mathie, A.C.F. Coster, N.H. Lovell, and B.G. Celler. Detection of daily physical activities using a triaxial accelerometer. *Medical & Biological Engineering & Computing*, 41(03):296–301, 2003.

[71] R. Matias and A.G. Pascoal. The unstable shoulder in arm elevation: A three-dimensional and electromyographic study in subjects with glenohumeral instability. *Clinical Biomechanics*, In Press, 2005.

[72] R.E. Mayagoitia, A.V. Nene, and P.H. Veltink. Accelerometer and rate gyroscope measurement of kinematics: an inexpensive alternative to optical motion analysis systems. *Journal of Biomechanics*, 35(4):537–542, 2002.

[73] C.G.M. Meskers, H. Fraterman, F.C.T. van der Helm, H.M. Vermeulen, and P.M. Rozing. Calibration of the 'Flock of Birds' electromagnetic tracking device and its application in shoulder motion studies. *Journal of Biomechanics*, 32(7):629–633, 1999.

[74] D.G. Meskin and I.Y. Bar-Itzhack. Unified approach to inertial navigation system error modeling. *Journal of Guidance, Control and Dynamics*, 15(3):648–653, 1992.

[75] T.B. Moeslund and E. Granum. A survey of computer vision-based human motion capture. *Computer Vision and Image Understanding*, 81(3):231–268, 2001.

[76] T. Molet, R. Boulic, and D. Thalmann. Human motion capture driven by orientation measurements. *Presence*, 8(2):187–203, 1999.

[77] J.R.W. Morris. Accelerometry - A technique for the measurement of human body movements. *Journal of Biomechanics*, 6:729–736, 1973.

[78] A.M.M. Muijtjens, J.M.A. Roos, T. Arts, A. Hasman, and R.S. Reneman. Tracking markers with missing data by lower rank approximation. *Journal of Biomechanics*, 30(1):95–98, 1997.

[79] M. Munneke, Z. de Jong, A.H. Zwinderman, G.J. Tijhuis, J.M. Hazes, and T.P. Vliet Vlieland. The value of a continuous ambulatory activity monitor to quantify the amount and intensity of daily activity in patients with rheumatoid arthritis. *Journal of Rheumatology*, 28(4):745–50, 2001.

[80] National Geomagnetism Program. `http://geomag.usgs.gov`.

[81] M.A. Nixon, B.C. McCallum, W.R. Fright, and N.B. Price. The effect of metals and interfering fields on electromagnetic trackers. *Presence*, 7(2):204–218, 1998.

[82] International Commission on Non-Ionizing Radiation Protection. Guidelines on limits of exposure to static magnetic fields. *Health Physics*, 66:100–106, 1994.

[83] International Commission on Non-Ionizing Radiation Protection. Guidelines on limiting exposure to time-varying electric, magnetic and electromagnetic fields (up to 300 ghz). *Health Physics*, 74:494–522, 1998.

[84] Optotrak. `http://www.ndigital.com`.

[85] E. Paperno and P. Keisar. Three-dimensional magnetic tracking of biaxial sensors. *IEEE Transactions on Magnetics*, 4(3):1530–1536, 2004.

[86] E. Paperno and A. Plotkin. Cylindrical induction coil to accurately imitate the ideal magnetic dipole. *Sensors and Actuators A: Physical*, 112(2-3):248–252, 2004.

[87] Polhemus. `http://www.polhemus.com`.

[88] F.H. Raab, E.B. Blood, T.O. Steiner, and H.R. Jones. Magnetic position and orientation tracking system. *IEEE Transactions on Aerospace and Electronic Systems*, 15(5):709–718, 1979.

[89] C. Reinschmidt, A.J. van den Bogert, B.M. Nigg, A. Lundberg, and N. Murphy. Effect of skin movement on the analysis of skeletal knee joint motion during running. *Journal of Biomechanics*, 30:729–732, 1997.

[90] J.G. Richards. The measurement of human motion: A comparison of commercially available systems. *Human Movement Science*, 18(5):589–602, 1999.

[91] D. Roetenberg, C.T.M. Baten, and P.H. Veltink. Design and evaluation of a Kalman filter for estimation body segment orientation using inertial and magnetic sensing near ferromagnetic materials. In *Eighth International Symposium on the 3-D Analysis of Human Movement*, Tampa, Florida, USA, 2004.

[92] D. Roetenberg, C.T.M. Baten, and P.H. Veltink. Estimating body segment orientation by applying inertial and magnetic sensing near ferromagnetic materials. *IEEE Transactions on Neural Systems and Rehabilitation Engineering*, In Press, 2006.

[93] D. Roetenberg, H.J. Luinge, C.T.M. Baten, and P.H. Veltink. Compensation of magnetic disturbances improves inertial and magnetic sensing of human body segment orientation. *IEEE Transactions on Neural Systems and Rehabilitation Engineering*, 13:395–405, 2005.

[94] D. Roetenberg, H.J. Luinge, and P.H. Veltink. Inertial and magnetic sensing of human movement near ferromagnetic materials. In *IEEE/ACM International Symposium on Mixed and Augmented Reality (ISMAR)*, pages 268–269, Tokyo, Japan, 2003.

[95] D. Roetenberg and P.H. Veltink. Camera-marker and inertial sensor fusion for improved motion tracking. In *European Society of Movement Analysis for Adults and Children (ESMAC), Gait & Posture 22S*, pages 51–52, Barcelona, Spain, 2005.

[96] A.M. Sabatini, C. Martelloni, S. Scapellato, and F. Cavallo. Assessment of walking features from foot inertial sensing. *IEEE Transactions of Biomedical Engineering*, 52:486–494, 2005.

[97] K. Sagawa, H. Inooka, and Y. Satoh. Non-restricted measurement of walking distance. In *IEEE International Conference on Systems, Man, and Cybernetics*, pages 1847–1852, 2000.

[98] M. Sati, J.A. de Guise, S. Larouche, and G. Drouin. Quantitative assessment of skin-bone movement at the knee. *The Knee*, 3:121–138, 1996.

[99] D.J. Schneck. Biomechanics. In J.D. Bronzino, editor, *The Biomedical Engineering Handbook*, volume I. CRC Press & IEEE Press, second edition, 2000.

[100] P. Slycke, P.H. Veltink, and D. Roetenberg. Bewegingsvolgsysteem, 2006. Octrooi nr. 1030440.

[101] C. Smeesters, W.C. Hayes, and T.A. McMahon. The threshold trip duration for which recovery is no longer possible is associated with strength and reaction time. *Journal of Biomechanics*, 34(5):589, 2001.

[102] J. Soderkvist. Micromachined gyroscopes. *Sensors and Actuators A-Physical*, 43(1-3):65–71, 1994.

[103] C. Song and M. Shinn. Commercial vision of silicon-based inertial sensors. *Sensors and Actuators A: Physical*, 66(1-3):231–236, 1998.

[104] J. Stebbins, M. Harrington, N. Thompson, A. Zavatsky, and T. Theologis. Repeatability of a model for measuring multi-segment foot kinematics in children. *Gait & Posture*, In Press, 2005.

[105] V.P. Stokes. A method for the recovery of noisy missing data in movement analysis. *Computer Methods and Programs in Biomedicine*, 34(1):61–67, 1991.

[106] T. Stork. Electronic compass design using KMZ51 and KMZ52. *Philips Semiconductors Application Note*, AN00022, 2000.

[107] D.H. Sutherland. The evolution of clinical gait analysis. Part II: kinematics. *Gait & Posture*, 16(2):159–79, 2002.

[108] G.P.Y. Szeto, L.M. Straker, and P.B. O'Sullivan. A comparison of symptomatic and asymptomatic office workers performing monotonous keyboard work–2: Neck and shoulder kinematics. *Manual Therapy*, 10(4):281–291, 2005.

[109] M. Uiterwaal, E.B. Glerum, H.J. Busser, and R.C. van Lummel. Ambulatory monitoring of physical activity in working situations, a validation study. *Journal of Medical Engineering & Technology*, 22(4):168–72, 1998.

[110] P.H. Veltink. Sensory feedback in artificial control of human mobility. *Technology and Health Care*, 7(6):383–391, 1999.

[111] P.H. Veltink, C. Liedtke, A. Droog, and H. van der Kooij. Ambulatory measurement of ground reaction forces. *IEEE Transactions on Neural Systems and Rehabilitation Engineering*, 13:423–427, 2005.

[112] P.H. Veltink, P. Slycke, J. Hemssems, R. Buschman, G. Bultstra, and H. Hermens. Three dimensional inertial sensing of foot movements for automatic tuning of a two-channel implantable drop-foot stimulator. *Medical Engineering & Physics*, 25(1):21–8, 2003.

[113] Vicon. `http://www.vicon.com`.

[114] G. Welch and G. Bishop. An introduction to the Kalman filter. *TR 95-041, UNC-Chapel Hill*, 2004.

[115] L. Williamson and B.J. Andrews. Detecting absolute human knee angle and angular velocity using accelerometers and rate gyroscopes. *Medical & Biological Engineering & Computing*, 39(03):294–302, 2003.

[116] D.A. Winter. *Biomechanics and Motor Control of Human Movement*. John Wiley, 1990.

[117] H.K. Xie and G.K. Fedder. Integrated microelectromechanical gyroscopes. *Journal of Aerospace Engineering*, 16(2):65–75, 2003.

[118] Xsens Motion Technologies. MTx data sheet. `http://www.xsens.com`.

[119] V.M. Zatsiorsky. *Kinematics of Human Motion*. Human Kinetics, Champaign III, 1998.

[120] R. Zhu and Z. Zhou. A real-time articulated human motion tracking using tri-axis inertial/magnetic sensors package. *IEEE Transactions on Neural Systems and Rehabilitation Engineering*, 12(2):295–302, 2004.

Abstract

M OVEMENT and posture tracking of the human body is of great interest in
many different disciplines such as monitoring of activities of daily living,
assessment of working load in ergonomics studies, measurement of neurological
disorders, computer animation, and virtual reality applications. This thesis deals
with ambulatory position and orientation measurements of human body segments.
Using inertial and magnetic sensing and actuation on the body, motion analysis
can be performed anywhere, without the need for an expensive lab.

Chapter 2 describes a complementary Kalman filter design to estimate ori-
entation of human body segments by fusing gyroscope, accelerometer and mag-
netometer signals from miniature sensors. Changes in angles are determined by
integration of angular velocities measured by the gyroscopes. Noise and offset
fluctuations will cause big errors using only gyroscope integration. Accelerometers
provide a means to estimate inclination by measuring the gravitational acceleration
component. The magnetometers give information about the heading direction, like
a compass. By combining all signals in a complementary Kalman filter, the drift er-
rors can be estimated and corrected. However, ferromagnetic materials (e.g. iron)
or other magnetic fields near the sensor module disturb the local earth magnetic
field and can therefore distort the orientation estimation, if not accounted for. In
the filter, magnetic disturbances, gyroscope bias errors and orientation errors were
estimated and used to correct the orientation of the sensor module. The algorithm
was tested under quasi-static and limited dynamic conditions with ferromagnetic
materials close to the sensor module. The results showed drift-free and accurate
orientation estimates with the capability to compensate for magnetic disturbances.
The average static error was 1.4 degrees in the magnetically disturbed experiments.
The dynamic error was between 1.3 and 2.4 degrees depending on the distance to
the iron and movement speed.

Chapter 3 compares the orientation output of the sensor fusion using three-
dimensional inertial and magnetic sensors against a laboratory bound camera sys-
tem (Vicon) in a simulated work environment. With the tested methods, the
difference between the optical reference system and the output of the algorithm
was 2.7 degrees when no metal was near the sensor module. Near a large metal

121

Abstract

object instant errors up to 50 degrees were measured when no compensation was applied. Using the magnetic disturbance model, the error reduced significantly to 3.9 degrees.

Optically based systems offer accurate position tracking of body segments. However, the line of sight between marker and camera can be blocked, resulting in incomplete data. **Chapter 4** proposes a method in which the position estimates from miniature inertial sensors are used to fill the gaps of the optical position measurements. A complementary Kalman filter provides accurate position estimates by fusing the data from the optical and inertial systems. When performing an off-line analysis, a smoothing algorithm in which the data is also processed reverse in time significantly improves the performances. Besides the ability to bridge gaps, the data of the inertial sensors can be used to increase the data rate beyond the limitations of the optical system. Low-cost inertial sensors sampled at a high frequency, fused with a camera-marker based system running at a low frequency, can provide an alternative for expensive high-speed cameras.

Chapter 5 focuses on the design of a portable magnetic tracking system. Three essential components comprise this system (1) 3D source, consisting of three orthogonal coils, which generates a magnetic field and is fixed on the body; (2) a compatible 3D sensor, which is fixed at a remote body segment and detects the fields generated by the source; and (3) a processor whose function is to relate the signals from source and sensor. Given these signals, the position and orientation of the sensor in 6 DOF with respect to the position of the transmitter can be estimated. The source is scaled and the electronics are designed to run on battery supply, making it suitable for body mounting and ambulatory measurements. The accuracy of the distance measurements was approximately 8 mm. Errors were higher during fast movements due to the low pulsing frequency.

In **Chapter 6**, the portable magnetic system is combined with inertial sensors. Magnetic pulsing requires a substantial amount of energy which limits the update rate with a set of batteries. Moreover, the magnetic field can easily be disturbed by ferromagnetic materials or other sources. Inertial sensors can be sampled at high rates, require only little energy and do not suffer from magnetic interferences. However, accelerometers and gyroscopes can only measure changes in position and orientation and suffer from integration drift. By combing measurements from both systems in a Kalman filter structure, an optimal solution for position and orientation estimates is obtained. The implemented system is tested against a lab-bound camera tracking system for several functional movements. The accuracy was about 5 mm for position and 3 degrees for orientation measurements. Although the implemented system cannot be used yet in clinical practice, it opens many possibilities for fully ambulatory measurements.

Samenvatting

DE ANALYSE van bewegingen en houdingen van het menselijk lichaam wordt veel toegepast in zowel de medische wereld als in computer animaties en virtual reality. In dit proefschrift worden verschillende methodes en technieken onderzocht om ambulant posities en oriëntaties van lichaamssegmenten te meten. Door inertiële sensoren en magnetische actuatoren op het lichaam te plaatsen kan bewegingsanalyse overal worden uitgevoerd waardoor geen duur laboratorium nodig is.

Hoofdstuk 2 beschrijft het ontwerp van een methode waarmee oriëntaties van lichaamssegmenten geschat kunnen worden door een combinatie van miniatuur 3D gyroscopen, versnellingsopnemers en magnetische sensoren. Hoeken in drie richtingen kunnen worden bepaald door het integreren van hoeksnelheden, gemeten met de gyroscopen. Door ruis en kleine offset fluctuaties leidt deze integratie snel tot accumulatie van fouten. De versnellingsopnemers worden gebruikt om inclinatie te schatten door het meten van de gravitatieversnelling. De magnetometers worden gebruikt als een kompas en geven informatie over de richting in het horizontale vlak. Door alle signalen te combineren in een complementair Kalman filter kunnen deze drift fouten gecorrigeerd worden. Echter, ferromagnetische materialen (bv. ijzer) of andere magnetische bronnen in de buurt van de sensor module verstoren plaatselijk het aardmagnetisch veld en daarmee de kompasrichting. Als daar geen rekening mee wordt gehouden zal de oriëntatie schatting verstoord worden. In het geïmplementeerde filter worden deze magnetische verstoringen geschat evenals de oriëntatie fout en de gyroscoop offset. Het filter is getest en laat nauwkeurige resultaten zien onder quasi-statische en een beperkte set dynamische condities, waarbij ferromagnetische materialen dichtbij de sensor waren geplaatst. De gemiddelde statische fout was 1,4 graden in magnetisch verstoorde experimenten. De dynamische fout lag tussen de 1,3 en 2,4 graden, afhankelijk van de afstand tot een ijzeren voorwerp en de snelheid van bewegen.

In **Hoofdstuk 3** wordt de output van het oriëntatie sensor fusie algoritme vergeleken met een lab gebonden camera systeem (Vicon) voor een aantal functionele bewegingen. Wanneer geen er metaal in de buurt van de sensor module was geplaatst, kwam het verschil tussen het algoritme en het optische referentiesysteem

op gemiddeld 2,7 graden. Dichtbij een ijzeren kast werden tijdelijke afwijkingen tot wel 50 graden gemeten als er geen compensatie voor die verstoring werd toegepast. Met de toepassing van het magnetische verstoringsmodel werden de afwijkingen significant gereduceerd tot gemiddeld 3,9 graden.

Optisch gebaseerde systemen worden vaak gebruikt voor bewegingsanalyses en geven over het algemeen nauwkeurige resultaten. Echter, het zicht van de camera naar de marker kan beperkt zijn, wat resulteert in incomplete data. In **Hoofdstuk 4** wordt een methode gepresenteerd waarin positie schattingen gemaakt met inertiële sensoren worden gebruikt om de discontinuïteiten in de optische metingen te overbruggen. Door de optische en inertiële data te combineren in een complementair Kalmal filter worden nauwkeurige resultaten behaald. In een off-line analyse kunnen de resultaten nog verbeteren omdat met een smoothing algoritme de data ook terug in de tijd geanalyseerd kan worden. Naast de mogelijkheid om gaten in de data op te vullen kan deze methode worden gebruikt om de dynamische eigenschappen van het camera systeem te verbeteren.

In **Hoofdstuk 5** wordt het ontwerp van een draagbaar magnetisch meetsysteem beschreven. Het systeem bestaat uit drie onderdelen (1) een 3D bron, bestaande uit drie orthogonale spoelen die een magnetisch veld genereren en op het lichaam zijn geplaatst; (2) een 3D sensor, geplaatst op een lichaamsegment, die de magnetische velden van de spoelen kan meten, en (3), een processor die met de gemeten signalen de positie en oriëntatie van de sensor in zes vrijheidsgraden ten opzichte van de bron kan berekenen. De bron en elektronica zijn zo ontworpen dat deze op batterijen werken waardoor het hele systeem op het lichaam gedragen kan worden. De nauwkeurigheid van de positie metingen was ongeveer 8 mm. De fout werd groter bij snelle bewegingen als gevolg van een te lage pulsfrequentie.

In **Hoofdstuk 6** wordt het draagbare systeem gecombineerd met inertiële sensoren. Het actueren van de spoelen kost een aanzienlijke hoeveelheid energie waardoor de samplefrequentie en meettijd beperkt is. Bovendien kan het uitgezonden magnetische veld worden verstoord door ferromagnetische materialen en andere bronnen. Inertiële sensoren kunnen met hoge snelheden worden gesampled, gebruiken weinig energie en hebben geen last van magnetische verstoringen. Echter, versnellingsopnemers en gyroscopen kunnen alleen veranderingen in posities en oriëntaties meten en hebben last van integratie drift. De combinatie van beide systemen in een Kalman filter structuur levert een optimale schatting van posities en oriëntaties op het lichaam. Het ontwikkelde systeem is getest en de resultaten zijn vergeleken met een camera systeem voor verschillende functionele bewegingen. De nauwkeurigheid was ongeveer 5 mm voor positie en 3 graden voor oriëntatiemetingen. Het ontwikkelde systeem is nog niet in alle opzichten geschikt om in de klinische praktijk te gebruiken, maar opent vele mogelijkheden voor ambulante metingen.

Dankwoord

V IER JAAR geleden begon ik met de uitdaging, bewegingen van het menselijk lichaam zo goed mogelijk vast te leggen. Het project bevatte vele interessante aspecten. Ik heb gemeten aan en met mensen, mij verdiept in sensor technologie, biomechanica, Kalman filters en heb zelfs een soldeerbout in de handen gehad. Nu, zo'n vier jaar later is dit proefschrift het resultaat. Dit was natuurlijk niet mogelijk zonder de hulp van velen.

Allereerst wil ik mijn dagelijkse begeleider en promotor Peter Veltink bedanken. Het werken met jou als begeleider was van begin tot eind prettig. Ik heb veel geleerd van jouw creatieve en kritische blik en structurele manier van werken. Je liet me vrij in het ontwerpen van de systemen en de discussies hierover leverden altijd weer interessante nieuwe ideeën op

Henk Luinge, dankzij jou heb ik mij snel kunnen inwerken in de moeilijke materie van inertiële sensoren en Kalman filters. In het ontwerpen en testen van de verschillende filters waren jouw inzicht en algoritmes onmisbaar.

Per Slycke, je bent altijd zeer betrokken geweest bij mijn werk. De overdracht van mijn werk naar Xsens was voor mij een waardevolle erkenning. Ik ben erg trots op ons gezamenlijke octrooi en hoop dat we in de toekomst nog mooie dingen kunnen ontwikkelen.

Chris Baten, jouw enthousiasme en vertrouwen in deze technologie is ongekend. Het schrijven van het projectvoorstel voor FreeMotion was een leerzame ervaring. Naast de inhoudelijke besprekingen heb ik genoten van onze discussies over fotografie en muziek.

Bedankt: het team van Xsens, voor het leveren van uitstekende sensormodules, de 'bewegingstechneuten' van RRD, Leendert, Wiebe en Jan Hindrik voor het met raad en daad bijstaan in de experimenten, TNO Industrie, in het bijzonder Ron Niesten en Andre Ventevogel, voor het bouwen van de 'magnetic dome', waarmee ik mijn laatste testen heb kunnen uitvoeren, Christian en Martin voor de hulp tijdens de experimenten, en de proefpersonen die zich gewillig met sensoren lieten

volhangen. En natuurlijk alle collega's van de leerstoel Biomedische Systemen en Signalen, voor zowel allerlei werkgerelateerde zaken als alle informele activiteiten. Ik kwam altijd met veel plezier op vloer 6.

Ljubomir en Remy, de sfeer in onze kamer was altijd zeer relaxed. Ik ben blij dat jullie mij bijstaan als paranimfen tijdens de verdediging.

Om te kunnen promoveren wordt er heel wat inspanning van iemand vereist, maar gelukkig waren er altijd velen die zorgden voor de nodige ontspanning. Zo kon ik me altijd heerlijk uitleven met vrienden tijdens het sporten, aan de ringen, op de ijsbaan of op het honkbalveld. Vooral de vakantie naar Las Vegas was een fantastische ontspanning in de laatste maanden voor de afronding van mijn studie. Stroat Ensemble, bedankt voor de vele uren muziek en feestplezier.

Pa en ma, het is altijd heerlijk om even 'thuis' te komen.

Yvette ♡, je stond altijd voor me klaar en zorgde voor rust, kus!

Iedereen, bedankt, gracias, thanks ☺